

AF-TR-01-

**NONLINEAR REDUCED-ORDER
MODELING OF LIMIT CYCLE
OSCILLATIONS OF AIRCRAFT
WINGS AND WING/STORE**



Contract No.: F49620-01-C-0029
PR/MIPR No: FQ867100100889

Contractor:
ZONA Technology, Inc.
7430 E. Stetson Drive, Ste. 205
Scottsdale, AZ 85251

Sponsor:
USAF, AFRL
AF Office of Scientific Research
801 N. Randolph Street, Room 732
Arlington, VA 22203-1977
TPOC: Dr. Daniel Segalman, Tel (703) 696-7259

December 2003

PHASE II FINAL REPORT FOR THE PERIOD MAY 2001 – OCT 2003

Approved for public release; distribution unlimited

AIR FORCE OFFICE OF SCIENTIFIC RESEARCH
801 N. RANDOLPH STREET, ROOM 732
ARLINGTON, VA 22203-1977

20040112 184

REPORT DOCUMENTATION PAGE
**Form Approved
OMB No. 0704-0188**

The public reporting burden for this collection of information is estimated to average 1 hour per response, including the time for reviewing instructions, searching existing data sources, gathering and maintaining the data needed, and completing and reviewing the collection of information. Send comments regarding this burden estimate or any other aspect of this collection of information, including suggestions for reducing the burden, to Department of Defense, Washington Headquarters Services, Directorate for Information Operations and Reports (0704-0188), 1215 Jefferson Davis Highway, Suite 1204, Arlington, VA 22202-4302. Respondents should be aware that notwithstanding any other provision of law, no person shall be subject to any penalty for failing to comply with a collection of information if it does not display a currently valid OMB control number.

PLEASE DO NOT RETURN YOUR FORM TO THE ABOVE ADDRESS.

1. REPORT DATE (DD-MM-YYYY) 09-12-2003	2. REPORT TYPE FINAL	3. DATES COVERED (From - To) May 10, 2001 - Oct. 31, 2003		
4. TITLE AND SUBTITLE Nonlinear Reduced-Order Modeling of Limit Cycle Oscillation of Aircraft Wing and Wing Store		5a. CONTRACT NUMBER F49620-01-C-0029		
		5b. GRANT NUMBER		
		5c. PROGRAM ELEMENT NUMBER		
6. AUTHOR(S) Mr. P.C. Chen, Dr. Danny D. Liu, Dr. Xiaowei Gao ZONA Technology, Inc. Dr. Kenneth C. Hall, Dr. Earl H. Dowell, Dr. Jeffrey P. Thomas Duke University		5d. PROJECT NUMBER FQ867100100889		
		5e. TASK NUMBER		
		5f. WORK UNIT NUMBER		
7. PERFORMING ORGANIZATION NAME(S) AND ADDRESS(ES) ZONA Technology, Inc. 7430 E. Stetson Drive, Ste. 205 Scottsdale, AZ 85251-3540 Tel 480-945-9988 / Fax 480-945-6588 / URL: www.zonatech.com		8. PERFORMING ORGANIZATION REPORT NUMBER ZONA 03-45		
9. SPONSORING/MONITORING AGENCY NAME(S) AND ADDRESS(ES) USAF, AFRL AF Office of Scientific Research 801 N. Randolph St., Room 732 Arlington, VA 22203-1977 Attn. Dr. Daniel Segelman (TPOC) 703-696-7259		10. SPONSOR/MONITOR'S ACRONYM(S) AFOSR		
		11. SPONSOR/MONITOR'S REPORT NUMBER(S)		
12. DISTRIBUTION/AVAILABILITY STATEMENT Approved for public release; distribution unlimited				
13. SUPPLEMENTARY NOTES				
14. ABSTRACT Significant progress has been made by the ZONA-Duke team in Phase II of our work. A novel and computationally efficient method for calculating transonic limit cycle oscillations (LCO), flutter and other nonlinear aeroelastic phenomena has been developed. To solve the general 3D Euler and Reynolds Averaging Navier-Stokes (Euler/RANS) equations, a Harmonic Balance (HB) method formulated in the frequency domain in combination with a proper orthogonal decomposition (POD) technique and reduced order modeling (ROM) has been developed and demonstrated on several challenging examples relevant to the Air Force. Various 2D and 3D cases for Euler/RANS have been studied including the conventional NACA 64A10 airfoil, the supercritical NAL7301 airfoil, the AGARD 445.6 wing and the F-16 wing/store system with the actual structural modes provided by an industry/Air Force team. These comprehensive studies have demonstrated the computational efficiency and solution accuracy of the HB and POD/ROM methods in the nonlinear and linear domains for aeroelastic applications to LCO and flutter prediction. Validation of the computational efficiency of the HB frequency domain and POD/ROM methods has been provided by comparison with results obtained in a time- domain, time marching study using the NASA developed CFL3D computer code. The results obtained using CFL3D show that the HB method is superior in terms of computation efficiency and also in the ease of LCO/Flutter identification. These achievements in phase II provide a firm foundation upon which a phase III effort can be launched to develop a commercially viable set of computer codes for transonic flutter and LCO prediction that will be useful to industry and the Air Force in the design process.				
15. SUBJECT TERMS Transonic limit cycle oscillations; transonic flutter; reduced order modeling; Harmonic Balance, frequency domain solution method; 2D/3D Euler-Navier-Stokes (RANS) solver; AGARD445.6 wing; F-16 wing/store configuration.				
16. SECURITY CLASSIFICATION OF: a. REPORT U		17. LIMITATION OF ABSTRACT SAM	18. NUMBER OF PAGES 144	19a. NAME OF RESPONSIBLE PERSON Mr. P.C. Chen
b. ABSTRACT U		19b. TELEPHONE NUMBER (Include area code) 480-945-9988		

Contents

1	Introduction	2
1.1	Review of Phase I Achievements	2
1.2	Phase II Goals and Technical Objectives	2
1.3	Proposed Method for Phases I/II: A Brief Review	3
1.3.1	Limit Cycle Oscillations	3
1.3.2	LCO Prediction Methods	4
1.3.3	Frequency-Domain POD/ROM EigenMode Approach	5
1.3.4	Merits of the Frequency-Domain Approach	6
1.4	The ZONA/Duke Team	6
2	Transonic Flutter and LCO in Nonlinear Inviscid Two Dimensional Flow: Frequency Domain	8
2.1	Introduction	8
2.2	Governing Equations	9
2.3	Frequency Domain Equations	11
2.4	Computational Model	13
2.5	Convergence Study Results	16
2.6	Aerodynamic Lift and Moment	19
2.6.1	Mass Ratio Effect	24
2.6.2	Ratio of Uncoupled Natural Frequencies Effect	24
2.6.3	Mach Number Effect	29
3	Transonic Flutter and LCO in Nonlinear Viscous Two Dimensional Flow: Frequency Domain	35
3.1	Introduction	36
3.2	Theoretical Development	36
3.2.1	Fluid Dynamic Model	36
3.2.2	Two-Dimensional Airfoil Aeroelastic Model	37
3.2.3	Static Aeroelastic Equation	38
3.2.4	LCO Solution Procedure	38
3.3	Steady and Unsteady Aerodynamic Modeling of the NLR 7301 Airfoil	40
3.3.1	Computational Mesh	41
3.3.2	Steady Flow Simulations	41
3.3.3	Unsteady Flow Simulations	47

3.3.4	Mesh and Harmonic Convergence Issues	47
3.4	Limit Cycle Oscillation Modeling for the NLR 7301 Configuration	48
3.4.1	Structural Parameters	48
3.4.2	Flutter Point Prediction	49
3.4.3	Zero Spring Stiffness Angle-of-Attack	51
3.4.4	Computed LCO Behavior	51
3.5	Conclusions	54
4	ZONA 2-DOF Airfoil LCO: CFL3D.AE	56
4.1	Introduction	57
4.2	Numerical Methodology	59
4.3	Results and Discussion	62
4.4	Time-Averaged Surface Pressure Distribution	62
4.5	Performance and Time Step Convergence	64
4.6	Effect of Viscosity and Turbulence Modeling	66
4.7	Effect of Perturbation Size	69
4.8	Conclusions	69
5	Theoretical Background of the Harmonic Balance Method in Three-Dimensions	72
5.1	Three-Dimensional Navier-Stokes and Euler Equations	72
5.2	Harmonic Balance	73
5.3	Time-Linearized Flow Three-Dimensional Flow Solver	75
5.4	Reduced Order Modeling of Time-Linearized Aerodynamic Models	76
5.5	Reduced-Order Aeroelastic Model for Multi-Degree-Of-Freedom Structures .	78
5.5.1	The Modal Approach	78
5.5.2	The Structural/Modal Damping	79
5.6	Structural Compatible Reduced-Order Aeroelastic Model	79
5.7	Modeling LCO of High Degree-of-Freedom Nonlinear Systems	80
6	Development of the Structural/FEM Models and CSD/CFD Grid Interfacing for Candidate Wings for LCO Investigation	81
6.1	Deforming CFD Meshes of the MAVRIC-I Business Jet Wing	84
6.2	Deforming CFD Mesh of the ARW-2 Wing	86
7	Duke 3D Wings LCO: AGARD 445.6	92
7.1	Introduction	93
7.2	Aeroelastic Model Governing Equations	94
7.3	Harmonic Balance Method	96
7.3.1	Governing Equations	96
7.3.2	Fourier Series Expansion	96
7.3.3	Fourier Coefficients	97
7.3.4	Time Domain Variables	97
7.3.5	Pseudo Time Marching	99
7.4	Limit Cycle Oscillation Solution Procedure	99
7.4.1	The AGARD 445.6 Transonic Wing Configuration	101

7.4.2	Unsteady Grid Motion Treatment	101
7.5	Nonlinear Unsteady Aerodynamics	104
7.5.1	Mesh Convergence	104
7.5.2	Finite Amplitude Motion Limits	106
7.5.3	Harmonic Convergence	106
7.6	Nonlinear Unsteady Aeroelasticity	110
7.6.1	Flutter Onset Trend for the AGARD 445.6 Wing Configuration . . .	110
7.6.2	LCO Behavior Trends for the AGARD 445.6 Wing Configuration . .	110
7.7	Conclusions	115
8	3D Wing With Store: F-16 Wing/Store	117
8.1	Introduction	118
8.2	Theoretical Details	118
8.3	New Theoretical Details	119
8.4	LCO Solution Procedure	119
8.5	Computational Details	120
8.5.1	F-16 Wing Structural Model	121
8.5.2	Limit Cycle Oscillations	122
8.6	Conclusions	122
9	Commercialization Strategy: Phase II	125
9.1	Next Generation Aeroelastic Software	125
9.2	Commercialization of the Software with ZAERO	126
10	Conclusion	127

List of Figures

2.1	Sketch of Aeroelastic Typical Section.	10
2.2	Depiction of the 97×97 , CFD Grid with Outer Boundary Radius of Ten Chord Lengths around a NACA 64A010A Airfoil.	13
2.3	Flutter Speed Index (a) and Reduced Frequency (b) vs the Squared Value of the "Averaged" Grid Step for the Meshes $N \times N$ of $N = 129, 97, 65, 49, 33$, and 25.	14
2.4	Flutter Speed Index (a) and Reduced Frequency (b) vs the Domain Radius. .	15
2.5	Real and Imaginary Parts of the Unsteady Aerodynamic Moment due to Plunge Motion vs Reduced Frequency $\bar{h} = 0.001$	17
2.6	Lift Curve Slope Results.	18
2.7	Lift and Leading-Edge Moment Coefficients (both per Radian) as Functions of Reduced Frequency $k \equiv \frac{\omega_b}{U_\infty}$ due to Pitching $\pm 1^\circ$ at the quarter-chord for $M = 0.8$	21
2.8	Flutter Behavior as a Function of the Mass Ratio for $\frac{\omega_b}{\omega_\alpha} = 0.5$	22
2.9	Flutter Behavior as a Function of the Mass Ratio for $\frac{\omega_b}{\omega_\alpha} = 0.8$	23
2.10	Flutter Behavior as a Function of the Ratio of Uncoupled Frequencies for $\mu = 25$	25
2.11	Flutter Reduced Frequency, $\bar{\omega}_f$, versus a) $\frac{\omega_b^2}{\omega_\alpha^2}$ and b) the coefficient a_2 of $a_2 (\frac{\omega_b^2}{\omega_\alpha^2})^2 + a_1 \frac{\omega_b^2}{\omega_\alpha^2} + a_0 = 0$ for $\mu = 25$	26
2.12	Flutter Behavior as a Function of the Ratio of Uncoupled Frequencies for $\mu = 100$	27
2.13	Flutter Behavior as a Function of Mach Number for $\frac{\omega_b}{\omega_\alpha} = 0.5$ and $\mu = 25, 100$. .	30
2.14	Flutter Behavior as a Function of Mach number for $\frac{\omega_b}{\omega_\alpha} = 0.8$ and $\mu = 25, 100$. .	31
2.15	Steady Flow Pressure Contours.	32
3.1	Example LCO Behavior Trends.	42
3.2	Geometry for "Typical" (Pitch/Plunge) Two-Degree-of-Freedom Airfoil Section Aeroelastic Model.	43
3.3	Computational Grids Used for the NLR 7301 Airfoil Configuration.	44
3.4	Computed Steady Flow Surface Pressure Distributions: NLR 7301 Airfoil Section, $M_\infty = 0.75$, $Re_\infty = 1.727 \times 10^6$	45
3.5	Computed Steady Flow Mach Number Contours: NLR 7301 Airfoil Section, $M_\infty = 0.75$, $Re_\infty = 1.727 \times 10^6$	46

3.6	Computed HB Method Unsteady Mach Number Contours: NLR 7301 Airfoil Section, $M_\infty = 0.75$, $Re_\infty = 1.727 \times 10^6$, $\bar{\alpha}_0 = 0.2$ (deg), $\bar{\alpha}_1 = 5.$ (deg), $\bar{\omega} = 0.3$, $a = -0.5$, $N_H = 3$ ($\Delta T = T/(2N_H + 1) = T/7$).	52
3.7	LCO Behavior Trends for the NLR 7301 Configuration	53
4.1	Transonic LCO Solutions and DLR Test Data for the NLR7301 Supercritical Airfoil at $M=0.75$	57
4.2	Multiblock C-type grid around NLR 7301 airfoil (eight 69x47 blocks).	60
4.3	Two-Degree-of-Freedom Dynamic Model.	62
4.4	Time-Averaged Surface Pressure Distribution (spring-off).	63
4.5	Time-Averaged Surface Pressure Distribution (spring-on).	63
4.6	Entropy Contours (spring-on): (a) by B-L-D-S model; (b) by S-A model.	63
4.7	Comparison of Single/Multiblock Grid Computations (N-S, $M_\infty = 0.753$, $\alpha = 0.6^\circ$) $t_0=4.5s$ (8 blocks): (a) Plunge Motion; (b) Pitch Motion.	66
4.8	LCO Predicted by Euler/N-S Methods: (a) Plunge Motion; (b) Pitch Motion.	67
4.9	Predicted Density Contours: (a) by B-L-D-S Model; (b) by S-A Model.	68
4.10	Effect of Initial Perturbation Sizes: (a) Plunge Motion; (b) Pitch Motion.	70
4.11	Density Contours Showing Effect of Initial Perturbation Sizes: (a) 1st Cycle; (b) 2nd Cycle; (c) 3rd Cycle; (d) Final LCO Cycle.	71
6.1	Instrumentation Layout for Refurbished MAVRIC-I Business Jet Wing Model	82
6.2	MSC NASTRAN FEM of the ARW-2 Wind-Tunnel Model	82
6.3	AGARD Standard 445.6 wing, Showing Dimensions: $AR = 4.0$, $\lambda=45$ deg, $\Lambda=0.6$, NACA 65A004 airfoil section (taken from AGARD Report 765 by Dr. Carson Yates.)	83
6.4	Wing Aerodynamic and Structural Model	83
6.5	Structural Finite Element Model of the MAVRIC-I Business Jet Wing.	85
6.6	CFD Surface Mesh of the MAVRIC-I Business Jet Wing.	85
6.7	Deforming FEM Models and CFD Meshes of the 8 MAVRIC-I Wing Structural Modes.	89
6.8	Deforming FEM Models and CFD Meshes of the 8 MAVRIC-I Wing Structural Modes.	90
6.9	CFD Surface Mesh of the ARW-2 Wing	91
7.1	Mach Number Flutter Speed Dip Trend for the AGARD 445.6 Wing Configuration	94
7.2	Computed AGARD 445.6 Wing Configuration LCO Behavior Trends	95
7.3	Computational Grid Layout for AGARD 445.6 Wing Configuration. 49(i) x 33(j) x 33(k) Grid Shown.	102
7.4	AGARD 445.6 Wing "Weakened" Structural Configuration Mode Shapes.	103
7.5	Mesh Convergence Characteristics for the AGARD 445.6 Wing Surface Pressure at 70% of Wing Semi-span: $\alpha_0 = 0.0$ (deg), $M_\infty = 0.960$, $\bar{\omega} = 0.1$, and $\xi_1 = 0.0001$	105
7.6	Real part of Unsteady Generalized Force as a Function of Mode Shape Amplitude: $\alpha_0 = 0.0$ (deg), $M_\infty = 0.960$, and $\bar{\omega} = 0.1$	107

7.7	Imaginary part of Unsteady Generalized Force as a Function of Mode Shape Amplitude: $\alpha_0 = 0.0$ (deg), $M_\infty = 0.960$, and $\bar{\omega} = 0.1$	108
7.8	Mean and Unsteady Flow Surface Pressure Distribution Dependence on Mode Shape Amplitude: $\alpha_0 = 0.0$ (deg), $M_\infty = 0.960$, $\bar{\omega} = 0.1$, and $N_H = 3$	109
7.9	Mean and Unsteady Flow Surface Pressure Distribution Dependence on Number of Harmonic Used in HB Solver: $\alpha_0 = 0.0$ (deg), $M_\infty = 0.960$, $\bar{\omega} = 0.1$, and $\xi_1 = 0.0120$	112
7.10	Mach Number Flutter Speed Dip Trend for the AGARD 445.6 Wing Configuration	113
7.11	Computed AGARD 445.6 Wing Configuration LCO Behavior Trends.	113
7.12	Computed AGARD 445.6 Wing Configuration LCO Behavior Trends When Using Different Numbers of Structural Modes in HB/LCO Solutions Procedure.	114
8.1	F-16 Inviscid Flow Case Computational Grid.	120
8.2	F-16 Inviscid Flow Case Computed Mach Contours, $M_\infty = 0.9$, $\alpha_0 = 1.5$ deg..	121
8.3	F-16 Structural Model Computational Nodes	122
8.4	Computed F-16 LCO Trends for Three Difference Altitudes Based on Viscous Flow Model. $\alpha_0 = 1.541$ (deg)	123

List of Tables

3.1	Mesh Resolution and Number of Harmonic Used in Harmonic Balance Solver Trends for Computed First Harmonic Unsteady Moment Coefficient $\bar{c}_{m_1}/\bar{\alpha}_1$: $M_\infty = 0.75$, $Re_\infty = 1.727 \times 10^6$, $\bar{\alpha}_0 = 0.2$ (deg), $\bar{\alpha}_1 = 5$. (deg), $\bar{\omega} = 0.3$, and $a = -0.5$	47
3.2	Structural Parameter Values for the NLR 7301 Aeroelastic Configuration.	48
3.3	Computed Flutter Point Conditions and NLR 7301 Aeroelastic Configuration Experimental Test Case MP77 LCO Conditions.	50
4.1	Cost/Performance	65
4.2	Time Step Convergence, 1 Block Grid	65
6.1	Natural Frequencies, Generalized Masses, and Generalized Stiffness of the MAVRIC-I Business Jet Wing.	84
6.2	Natural Frequencies, Generalized Masses, and Generalized Stiffness of the ARW-2 Wing.	86
7.1	AGARD 445.6 Wing Configuration Maximum Modal Coordinate Amplitudes - 49(i) x 33(j) x 33(k) Grid.	106
7.2	AGARD 445.6 Wing Configuration Mach Number Flutter Onset Conditions.	111

Chapter 1

Introduction

1.1 Review of Phase I Achievements

Significant milestones have been reached through the work of Phase I. These are in four related categories. Firstly, the modeling and prediction of flutter and LCO of an airfoil and control surface with structural freeplay in 2D transonic flow has been accomplished. Secondly, the modeling and prediction of flutter and LCO of an airfoil undergoing single degree of freedom pitch motions due to nonlinear aerodynamic effects associated with large (inviscid) shock motions in 2D flow has been achieved. Thirdly, the modeling and prediction of flutter of a 3D flow about an elastic wing has been accomplished. Note that in the latter category, we are modeling the nonlinear static or steady flow effects in the transonic regime even though the aerodynamic model is dynamically linear, i.e., the shock motions are assumed to be proportional to the airfoil motion in this model. And finally, a 2D numerical simulation of the NLR 7301 supercritical airfoil limit cycle oscillations was performed using the time-marching procedure of the CFL3D code. This fourth category of work is to establish benchmarks for the viscous POD/ROM methodology developed in Phase I and to be developed in Phase II.

1.2 Phase II Goals and Technical Objectives

The overarching goal for the Phase II work is to build on the very substantial progress made in Phase I and to develop a capability for a highly computationally efficient and physically accurate mathematical modeling of limit cycle oscillations (LCO) and other nonlinear aeroelastic phenomena. The approach uses the concepts of aerodynamic modes as well as structural modes. Such models provide substantially improved physical understanding and also more accurate prediction of LCO in particular and nonlinear aeroelastic responses in general. This capability may also lead to a rational prediction of buffet onset due to aerodynamically nonlinear oscillations.

Phase II technical objectives included:

- Develop the 2-D N-S version of the above proposed approach
- Investigate further the initial condition impact on LCO via a 2-D time-domain method (CFL3D/N-S code)

- Extend the geometry capability to 3-D including wing/store configurations
- Generalize the 2-D/3-D methods to include Harmonic Balance technique for nonlinear LCO analysis
- Include multiple structural mode analysis capability
- Perform LCO case studies including wing-alone and F-16 wing/store systems.

1.3 Proposed Method for Phases I/II: A Brief Review

1.3.1 Limit Cycle Oscillations

Limit Cycle Oscillations (LCO) are known to occur on various operational vehicles. In particular, LCO has been a prevalent aeroelastic problem on several current fighter aircraft. It usually occurs for aircraft with external stores throughout the transonic flight regime (Refs [1, 2, 3, 4]). Complicated by the aircraft-store system, its mechanism still remains to be fully understood. Meanwhile, a business jet wing LCO was also reported recently (Refs [5, 6]). This has been a serious concern since there are few analytical techniques available for LCO prediction and an insufficient understanding of its physics.

LCO can be characterized as sustained periodic oscillations which neither increase or decrease in amplitude over time for a given flight condition. Using an s-domain unsteady aerodynamic model of the aircraft and stores, Chen, Sarhaddi and Liu (Ref [7]) have shown that wing/store LCO can be a post-flutter phenomenon whenever the flutter mode contains low unstable damping. This type of flutter mode is called a "hump mode". Since the aircraft structure usually contains structural nonlinearity, such as friction damping, this amplitude-dependent friction damping can suppress the growth of amplitude, thus resulting in a steady state oscillation. This is known as the nonlinear structural damping (NSD) model of the wing/store LCO. Although not thoroughly proven through tests or numerical simulations, results of the NSD show excellent correlation with flight test LCO data of F-16 throughout subsonic and transonic Mach numbers.

On the other hand, other researchers, notably Cunningham and Meijer (Ref [8]) believe that the wing/store LCO is due largely to transonic shock oscillation and shock induced flow separation. This is called the Transonic Shock/Separation (TSS) model. Edwards has suggested the TSS model and viscous effects are two major factors that cause transonic LCO for wings. He also has studied the shock buffet phenomenon in addition to transonic LCO (Ref [9]). It should be noted, however, that there is no conflict between the NSD model and the TSS model in that both physical effects may contribute to LCO.

Note that the method in Ref [7] used a damping correlation technique for LCO-onset prediction, whereas that of Ref [8] is a semi-empirical method that requires steady and unsteady data input from wind tunnel measurement.

1.3.2 LCO Prediction Methods

Recent renewed interest in LCO is motivated by the need to better predict and understand fighter LCO and also by the rapid advent of CFD methodology in aeroelasticity. Currently, there are two potential computational approaches for LCO prediction/investigation: the time-marching approach using a high-level CFD code such as CFL3D (Ref [10]) developed and supported by NASA/Langley, and the Frequency-Domain POD/ROM EigenMode approach (Ref [11]) originated by Dowell and Hall of Duke University. The former is a conventional time-domain CFD method whereas the latter is a frequency-domain CFD method using aerodynamic eigenmodes.

For nearly twenty years, the aerospace industry has been lacking of a viable, efficient CFD method for transonic flutter applications. The time-marching CFD unfortunately remain inefficient as a practical tool. Under an AFOSR/STTR Phase I contract, ZONA has recently conducted a feasibility study on the simulation of transonic LCO for a supercritical NLR7301 airfoil using the CFL3D/Navier-Stokes code. It was found that the time-marching LCO solution is turbulence-model dependent and time-step sensitive. One LCO solution case typically would take 96 hours on a 1GHz CPU computer.

Earlier work of Bendiksen (Ref [12]) and recent work of Sheta et al (Ref [13]) also used time-marching CFD approach for Euler transonic and N-S incompressible LCO simulations, respectively. Based on the cases studied by ZONA, the time-marching Euler simulation of a transonic LCO requires one half of the computing time required of a Navier-Stokes simulation, due to the reduction in grid points. The computing time required for incompressible Navier-Stokes LCO simulation is about two orders of magnitude less than a transonic Navier-Stokes LCO simulation, due to the absence of transonic nonlinearity, thus allowing much coarser time steps and a reduction in subiterations. For transonic Navier-Stokes simulation of LCO, the requirements in time steps, grid, subiterations, etc., become much more stringent, resulting in days of computing time for one LCO case. This leads to the conclusion that, if a transonic Navier-Stokes simulation were demanded, a time-marching approach would be computationally inefficient as a viable approach for realistic 3D transonic LCO prediction/investigations. On the other hand, the Frequency-Domain POD/ROM (Proper Orthogonal Decomposition / Reduced Order Model) method of Duke University is considered a recent breakthrough in the transonic computational aeroelasticity. Within the last five years, the Frequency-Domain POD/ROM method of Dowell and Hall has been proven to be highly efficient and shown to be widely applicable to aeroelastic problems for turbomachinery cascades, control surface freeplay, airfoil/wing flutter and LCO (e.g., Refs [11, 14, 15, 16]). As evidenced by their recent studies, under AFOSR/STTR contract support, the Frequency-Domain method with the Harmonic Balance scheme is about two-orders of magnitude faster than conventional time-marching methods.

For example, the 3D Time Linearized code can generate the needed aerodynamic model in one day for a given Mach number and flutter points take less than 1 minute per Mach number on a workstation computer.

1.3.3 Frequency-Domain POD/ROM EigenMode Approach

Reduced-Order Models (ROM) EigenMode

The eigenmodes of a time-linearized system, which may be thought of as aerodynamic states, were computed and subsequently used to construct computationally efficient, reduced order models of the unsteady flow field. An important advantage of the eigenmode based reduced order modeling technique is that once the eigenmode information has been computed, reduced order models can be constructed and used to calculate the response at different frequencies and mode shapes for almost no additional computational effort. Furthermore, only a very few eigenmodes or states (degrees of freedom) need to be retained in the model to accurately predict the unsteady aerodynamic response, making the method ideally suited for rapid flutter calculation and active control.

The POD Technique

The Proper Orthogonal Decomposition (POD) technique, also known as Karhunen-Loeve (Ref. [12]) expansions, was originally introduced, to determine and model coherent structures in turbulent flow fields. Using the POD approach, one examines a series of "snapshots" of experimental or computational data, each at a different instant in time. These solution snapshots are used to form a small and more compact eigenvalue problem that is solved to determine a set of optimal basis functions for representing the flow field.

Frequency-Domain POD/ROM

Hall, Thomas, and Dowell (Ref [11]) developed a frequency-domain form of the POD technique, and applied it to transonic flows about airfoils. In particular, they used a time-linearized CFD analysis to compute unsteady small-disturbance flow solutions for vibrating airfoils in the frequency domain over a range of frequencies. Basis vectors were then extracted from this frequency-domain data set using the POD technique. The resulting basis vectors were then used to construct low degree of freedom reduced-order models of the unsteady flow. Finally, the reduced-order aerodynamic model was combined with a structural dynamic model resulting in a compact, but accurate, flutter model.

Harmonic-Balance Method for Nonlinear LCO (Refs [14, 15])

In conjunction with the frequency-domain POD/ROM method, the harmonic balance (HB) technique can be used in the treatment of nonlinear LCO problems for oscillating wings (with stores). The harmonic balance technique is used to recast the proposed Euler equations into a set of "higher-order" equations of like harmonics. After introducing a pseudo-time term into the harmonic-balance equations so that they may be solved by time marching, these equations are solved by conventional CFD techniques. The method has a number of advantages over the more conventional time domain solutions. Because the solutions are computed in the frequency domain, the time-marching algorithm is only used to converge the solution to steady state. Thus, accelerating techniques, including pseudo time-marching with multi-grid acceleration can be used. Moreover, for problems where "engineering accuracy"

is required, the harmonic balance series can be truncated into just a few harmonics. The result is that the proposed harmonic balance method is potentially two-orders of magnitude faster than conventional time-marching methods for determining LCO.

1.3.4 Merits of the Frequency-Domain Approach

There are several definite advantages of using the frequency-domain approach. First, the frequency-domain harmonic balance method, when applied to high-level equations, can be at least two-orders of magnitude faster than the nonlinear time-domain CFD simulations. Also, this method retains essential nonlinear features in an aeroelastic system, including nonlinear structural stiffness and damping as well as large transonic shock excursions including viscosity. Second, current transonic flutter methods using time-domain/time-marching CFD in conjunction with various versions of the indicial approach (Refs [17, 18]) are very tedious and computationally expensive and their accuracy usually depends on the indicial motion imposed. By contrast, the frequency-domain formulation of POD/ROM directly solves for convenient aerodynamic mode shapes which can be stored and repeatedly applied for a large range of frequencies; hence, its a much more efficient and accurate method. Third, the frequency-domain approach with an eigenvalue solution method is a familiar practice to the structures/loads and flutter engineers. The proposed method after ZONA's further modification is expected to be well accepted within the industrial environment.

1.4 The ZONA/Duke Team

ZONA Technology, Inc. (ZONA) and Duke University (Duke) have formed a strong team with a comprehensive background to handle the challenging tasks in Phase II. Professor Hall (P.I.) and Professor Dowell, one of the world's leading aeroelasticians, at Duke are the originators of the proposed ROM/POD method, which has gained much attention in the aerospace community in recent years.

P.C. Chen (P.I.) and Danny D. Liu at ZONA are the small business counterpart of this STTR/Phase II. ZONA has been extensively engaged in the R&D of LCO including its prediction methodology, control and F-16 and F-18 LCO data correlation. ZONA has collaborated closely with Lockheed-Martin/LMTAS and the Seek Eagle office of Eglin AFB on F-16 wing/store LCO investigations. The results including the definition of a NSD model were presented in two AIAA/SDM papers (Refs [7, 19]). Under a recent NAVAIR contract, ZONA also worked closely with team member Boeing/ St Louis on a successful R&D in the reconfigurable adaptive control of the F-18 LCO. (Ref [20]). Supported by NASA/Langley, onging development of the CFD/CSD interfacing using BEM solver (Refs [21, 22]) will provide a new spline methodology for tightly coupled aerodynamic-structural interaction for 3D multiple mode LCO studies in Phase II.

In August 1999, the AFOSR awarded an STTR Phase I contract to the ZONA Technology (ZONA) team to develop innovative computational aeroelasticity methodologies for un-

derstanding, predicting and controlling critical nonlinear aerostructural interaction (e.g., LCO/flutter) phenomena. The ZONA/Duke team has successfully accomplished the STTR Phase II contract.

In what follows, we present the technical content of the Phase II final report.

Chapter 2 presents a comprehensive LCO and flutter study of a nonlinear inviscid transonic unsteady flow over a NACA64A010A airfoil (Euler Method). Chapter 3 presents a comprehensive LCO and flutter study of a nonlinear viscous transonic unsteady flow over a NLR7301 supercritical airfoil (RANS Method). Both studies adopts Duke University's innovative Harmonic Balance method in the frequency domain. As a counterpart to Chapter 3, Chapter 4 presents the time-domain simulation of the nonlinear viscous flow over the same NLR7301 airfoil for LCO investigation and verification (RANS Method: CFL3D code). Chapter 5 presents the theoretical background of Duke's Harmonic Balance method in three-dimensions. Chapter 6 summarizes the ZONA effort in providing the structural modes and deforming CFD meshes for various wing planform candidates to support Duke's LCO/flutter investigation using Duke's Harmonic Balance in three-dimensions. Chapter 7 presents a comprehensive LCO and flutter study of a nonlinear inviscid transonic unsteady flow over an AGARD 445.6 wing (3D Euler Method). Chapter 8 presents the LCO and flutter study of a nonlinear viscous transonic unsteady flow over an F-16 wing including effects due to stores (3D RANS Method). The method used in chapters 7 and 8 demonstrates the significant achievement in the generalization of the two-dimensional Harmonic Balance (HB) into a three-dimensional one up to the level of RANS (Reynolds Average Navier-Stokes) for its LCO/flutter application to a complex wing-store system.

This Phase II final report intends to provide a comprehensive description of our approach and results obtained in achieving the Phase II technical objectives (see 1.2). These achievements provide a sound foundation upon which the Phase III effort for technology transfer for a production-ready LCO prediction software can be carried out thus rendering viable commercialization.

Chapter 2

Transonic Flutter and LCO in Nonlinear Inviscid Two Dimensional Flow: Frequency Domain

Summary

- *A parametric study of transonic flutter and LCO has been carried out for a NACA 64A010A airfoil in a two-dimensional, inviscid (Euler) flow. Among the principal findings are that the LCO may be either benign (stable) with the LCO existing only beyond the flutter boundary or dangerous (unstable) with LCO occurring below the flutter boundary if a sufficiently large disturbance is given to the airfoil. This change from benign to dangerous LCO occurs when the Mach number is varied, for example. Also it is found that LCO of either type will only be detectable over a narrow range of Mach number. Outside of this Mach number range the predicted LCO amplitudes are so large as to be indistinguishable from flutter.*
- *The work in this chapter has been presented at the AIAA/SDM 2002 Conference: "D.B. Kholodar, J.P. Thomas, E.H. Dowell, and K.C. Hall, A Parametric Study of Transonic Airfoil Flutter and Limit Cycle Oscillation Behavior, AIAA Paper 2002-1211, presented at the AIAA/ASME/ASCE/AHS SDM Conference, April 2002, Denver, CO; it starts with the following abstract:*
- *Using a state of the art inviscid computational fluid dynamic harmonic balance aerodynamic Euler based code, a systematic, parametric investigation is presented into how the several structural parameters and freestream Mach number of a transonic flow affect the flutter characteristics of a "typical" two degree-of-freedom transonic airfoil configuration. The computational efficiency of the time linearized option of the harmonic balance aerodynamic model allows a much more thorough exploration of the parameter range than has been possible previously.*

2.1 Introduction

Transonic flow flutter and limit cycle oscillations (LCO) are of significant interest in wing and aircraft design. The large expense incurred in both time- and frequency-domain tran-

sonic aerodynamic computations is the principal obstacle to the aeroelastician in obtaining a deeper understanding of these phenomena through a systematic parameter study.

Reduced order modeling (ROM) techniques have been developed and used to overcome this obstacle in recent work on this subject. For a general review of the latest studies involving ROM based methods see Ref. [23]. Pade approximants of transfer functions and various other rational polynomial curve fitting techniques also have been used in recent years for linear flutter analysis, e.g. see Refs. [24, 25, 26].

In the past few years at Duke University a number of CFD time (dynamically) linearized codes have been developed [27, 28] and converted to the frequency domain. ROM techniques have then been applied to these dynamically linearized CFD codes and then used for flutter analyses that are very computationally efficient.

Recently, a novel nonlinear harmonic balance (HB) method that extends the frequency domain CFD models to the fully dynamically nonlinear range has been developed. This method enables one to model efficiently nonlinear unsteady aerodynamic behavior corresponding to finite amplitude structural motion of a prescribed frequency, and which can be subsequently used for modeling LCO behavior [27, 28, 29]. We believe these two methods, ROM based flutter analysis and HB based LCO modeling, will significantly advance the aeroelastician's capability to do rapid parametric studies.

In the current study, a time linearized option of the Euler HB model is used to capture the effects of the mean position of the shock and small shock motions about this mean position on transonic flutter. The shock motion is assumed linearly proportional to the airfoil motion in this study.

This study also had another goal, i. e. finding a (flutter) boundary of neutrally stable points for further use in a subsequent Limit Cycle Oscillation (LCO) study [29] of the same model with large shock motion aerodynamic nonlinearities included.

Results for the flutter boundary using the present methodology for the famous Isogai typical section case have been discussed in Ref. [30] and a favorable comparison made with the results of other investigators who used potential or Euler flow models. Further comparisons with results of others from theory and experiment are included in this paper.

2.2 Governing Equations

Consider a "typical" two degrees-of-freedom (DOF) airfoil section as shown in Fig. 2.1. The equations of motion of this aeroelastic system can be written in the form:

$$\begin{aligned} m\ddot{h} + S_\alpha \ddot{\alpha} + K_h h &= -L \\ S_\alpha \ddot{h} + I_\alpha \ddot{\alpha} + K_\alpha \alpha &= M_{e.a.} \end{aligned} \quad (2.1)$$

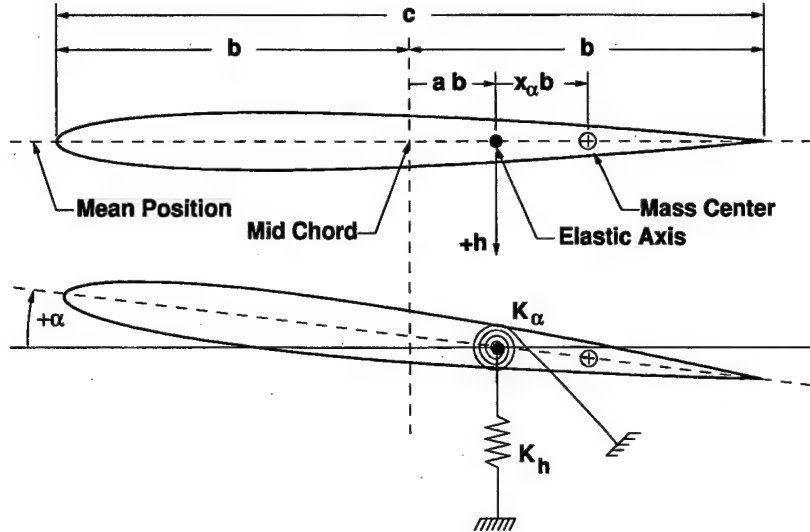


Figure 2.1: Sketch of Aeroelastic Typical Section.

Here the left-hand side terms represent a linear structural model approximation for the plunge and pitch coordinates. The right hand side terms represent the aerodynamic loading terms, which for this study are based upon the harmonic balance approach applied to a discrete CFD model of the inviscid Euler equations. Here we present a summary of the method. For a more detailed description see Refs. [27, 28].

In integral form, the unsteady Euler equations may be written as

$$\frac{\partial}{\partial t} \iint_{D(t)} \mathbf{U} dD + \oint_{\partial D(t)} \left(\mathbf{F}(\mathbf{U}) - \mathbf{U} \frac{\partial f}{\partial t} \right) dy - \oint_{\partial D(t)} \left(\mathbf{G}(\mathbf{U}) - \mathbf{U} \frac{\partial g}{\partial t} \right) dx = 0 \quad (2.2)$$

where x and y are the Cartesian coordinates, t is time, and D is a deforming control volume bounded by the control surface ∂D . The quantities $\partial f/\partial t$ and $\partial g/\partial t$ are the x and y components of the velocity of the control surface ∂D . The conservation fluid variables \mathbf{U} and flux vectors (\mathbf{F}, \mathbf{G}) are given by

$$\begin{aligned} \mathbf{U} &= \{\rho, \rho u, \rho v, E\}^T \\ \mathbf{F}(\mathbf{U}) &= \{\rho u, \rho u^2 + p, \rho u v, (E + p)u\}^T \\ \mathbf{G}(\mathbf{U}) &= \{\rho v, \rho u v, \rho v^2 + p, (E + p)v\}^T \end{aligned} \quad (2.3)$$

where ρ is the density, u and v are the velocity components in the x and y directions respectively, p is the pressure, and E is the total energy, which is the sum of the internal and kinetic energy:

$$E = \rho e + \frac{\rho}{2}(u^2 + v^2). \quad (2.4)$$

Considering a calorically perfect gas, the system of equations is completed via,

$$p = (\gamma - 1) \left\{ E - \frac{\rho}{2} [u^2 + v^2] \right\} \quad (2.5)$$

2.3 Frequency Domain Equations

The next step in the HB development is to consider strictly periodic unsteady flows of a fundamental frequency ω . The flow variables and flux vectors are then approximated using truncated Fourier series in time with spatially varying coefficients. For instance,

$$\iint_{D(t)} \mathbf{U} dD \approx \sum_{n=-N}^N \bar{\mathbf{U}}_n e^{in\omega t} \quad (2.6)$$

and

$$\oint_{\partial D(t)} \left(\mathbf{F}(\mathbf{U}) - \mathbf{U} \frac{\partial \mathbf{f}}{\partial \mathbf{x}} \right) dy - \oint_{\partial D(t)} \left(\mathbf{G}(\mathbf{U}) - \mathbf{U} \frac{\partial \mathbf{g}}{\partial \mathbf{y}} \right) dx \approx \sum_{n=-N}^N \bar{\mathbf{F}}_n e^{in\omega t} \quad (2.7)$$

where N is the number of harmonics used in the Fourier expansion. The time derivative of the vector of conservation fluid variables is then

$$\frac{\partial}{\partial t} \iint_{D(t)} \mathbf{U} dD \approx i\omega \sum_{n=-N}^N \bar{\mathbf{U}}_n e^{in\omega t} \quad (2.8)$$

Substituting (2.7) and (2.8) into the Euler equations (2.2), multiplying by $e^{-im\omega t}$, and integrating over one period yields a system of equations for the Fourier coefficients

$$\mathbf{A} \bar{\mathbf{U}} + \bar{\mathbf{F}} = \mathbf{0} \quad (2.9)$$

where the diagonal matrix \mathbf{A} and vectors $\bar{\mathbf{U}}$ and $\bar{\mathbf{F}}$ are

$$\begin{aligned} \text{diag} \mathbf{A} &= \{-iN, -i(N-1), \dots, iN\} \\ \bar{\mathbf{U}} &= \{\bar{U}_{-N}, \bar{U}_{-(N-1)}, \dots, \bar{U}_N\}^T \\ \bar{\mathbf{F}} &= \{\bar{F}_N, \bar{F}_{(N-1)}, \dots, \bar{F}_N\}^T \end{aligned} \quad (2.10)$$

As demonstrated by Hall [27] via a Fourier transform matrix, \mathbf{E} , one can relate the Fourier

coefficient variables, $\bar{\mathbf{U}}$, to the solution variables at $(2N + 1)$ discrete time levels within a period of motion. Hall also showed how one can express the Fourier Flux Coefficients in terms of time domain Flux term variables. This enables the HB methodology to be easily implemented within an existing steady CFD flow solver method. If one defines

$$\hat{\mathbf{U}} \equiv \begin{Bmatrix} \hat{U}(t_0) \\ \dots \\ \hat{U}(t_N) \end{Bmatrix} \equiv \begin{Bmatrix} \iint_{D(t_0)} \mathbf{U}(t_0) dD \\ \dots \\ \iint_{D(t_N)} \mathbf{U}(t_N) dD \end{Bmatrix} \quad (2.11)$$

and

$$\hat{\mathbf{F}} \equiv \begin{Bmatrix} \hat{F}(t_0) \\ \dots \\ \hat{F}(t_N) \end{Bmatrix} \equiv \begin{Bmatrix} \oint_{\partial D(t_0)} \left[(\mathbf{F}(\mathbf{U}) - \mathbf{U} \frac{\partial \mathbf{f}}{\partial \mathbf{x}}) |_{t_0} dy - \left(\mathbf{G}(\mathbf{U}) - \mathbf{U} \frac{\partial \mathbf{g}}{\partial \mathbf{y}} \right) |_{t_0} dx \right] \\ \dots \\ \oint_{\partial D(t_N)} \left[(\mathbf{F}(\mathbf{U}) - \mathbf{U} \frac{\partial \mathbf{f}}{\partial \mathbf{x}}) |_{t_N} dy - \left(\mathbf{G}(\mathbf{U}) - \mathbf{U} \frac{\partial \mathbf{g}}{\partial \mathbf{y}} \right) |_{t_N} dx \right] \end{Bmatrix} \quad (2.12)$$

where

$$t_n = \frac{2\pi n}{(2N + 1)\omega}, \quad n = 0, 1, \dots, 2N \quad (2.13)$$

then

$$\bar{\mathbf{U}} = \mathbf{E} \hat{\mathbf{U}}, \quad \bar{\mathbf{F}} = \mathbf{E} \hat{\mathbf{F}} \quad (2.14)$$

Substituting Eqs. (2.14) into the equation for the Fourier coefficients, Eq. (2.9), yields

$$\mathbf{A} \mathbf{E} \hat{\mathbf{U}} + \mathbf{E} \hat{\mathbf{F}} = \mathbf{0} \quad (2.15)$$

which after premultiplying by \mathbf{E}^{-1} results in

$$\mathbf{D} \hat{\mathbf{U}} + \hat{\mathbf{F}} = \mathbf{0} \quad (2.16)$$

where $\mathbf{D} \equiv \mathbf{E}^{-1} \mathbf{A} \mathbf{E}$ is the spectral source term operator that represents and approximates the temporal partial derivative, $\partial/\partial t$. As noted in Refs. [27, 28], to solve the harmonic balance equations, one can add a pseudo time derivative term $\partial \hat{\mathbf{U}}/\partial \tau$ to Eq. (2.16):

$$\frac{\partial \hat{\mathbf{U}}}{\partial \tau} + \mathbf{D} \hat{\mathbf{U}} + \hat{\mathbf{F}} = \mathbf{0} \quad (2.17)$$

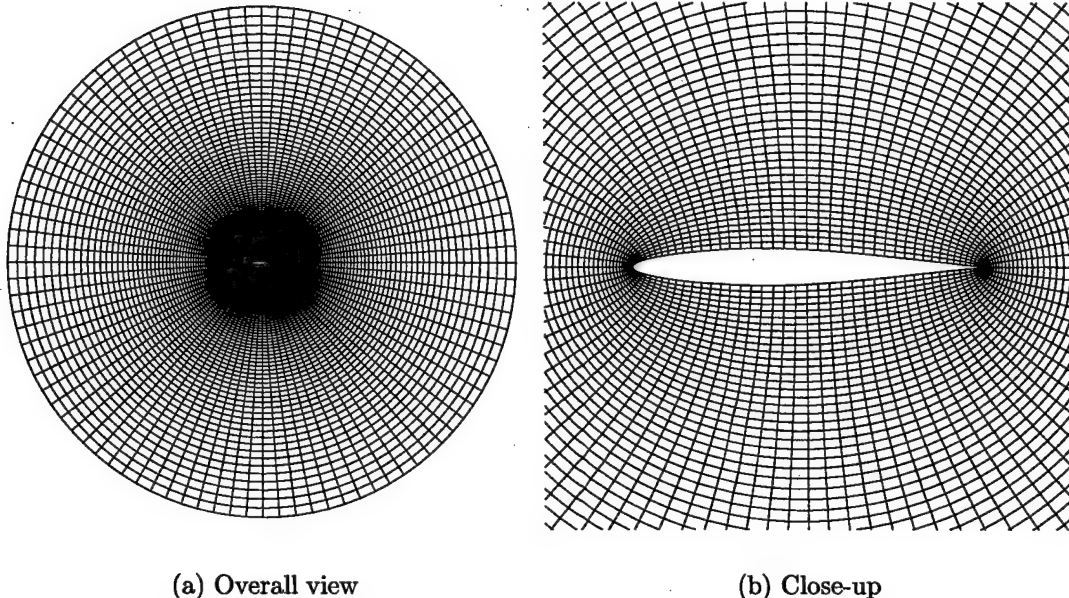


Figure 2.2: Depiction of the 97×97 , CFD Grid with Outer Boundary Radius of Ten Chord Lengths around a NACA 64A010A Airfoil.

where τ is a fictitious time. Since only a “steady-state”, temporally periodic solution is desired, local time stepping and multiple-grid acceleration techniques can be used to increase the speed of computational convergence. The above described procedures allow one to model nonlinear unsteady aerodynamic of a prescribed frequency very efficiently. Again, see Refs. [27, 28] for additional details.

2.4 Computational Model

Fig. 2.2a shows the “O”-type computational grid used; a close-up in Fig. 2.2b shows the grid cells that surround a symmetric NACA 64A010A airfoil. The mesh consists of $N_r \times N_\theta$ radial and circumferential nodes. Flutter results presented in this paper are computed using either 65×65 or 97×97 grids. However, grids of 25×25 , 33×33 , 49×49 and 129×129 were also considered for a grid convergence study. The outer boundary radius or domain radius, R , was chosen to be either 5 or 10 chord lengths however the domains of $R/c = 15$ and $R/c = 20$ chord lengths were also considered. The dependence of the calculated aerodynamic forces and flutter boundaries on the grid and domain size was investigated to ensure convergence of the numerical results. A slight variant of the standard node-centered Lax-Wendroff scheme was used to solve the Euler equations. See Refs. [31, 32] for further details.

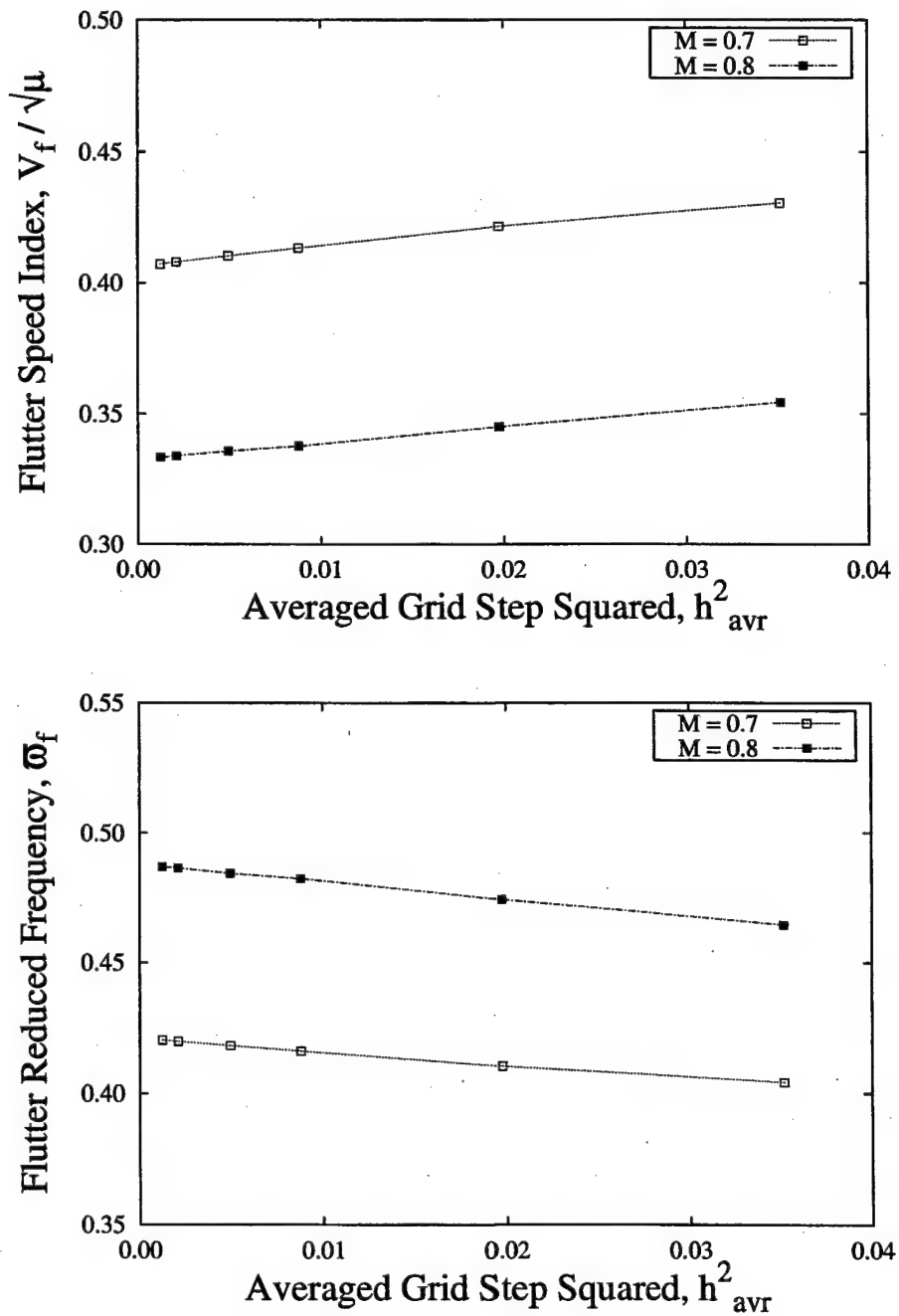


Figure 2.3: Flutter Speed Index (a) and Reduced Frequency (b) vs the Squared Value of the “Averaged” Grid Step for the Meshes $N \times N$ of $N = 129, 97, 65, 49, 33$, and 25 .

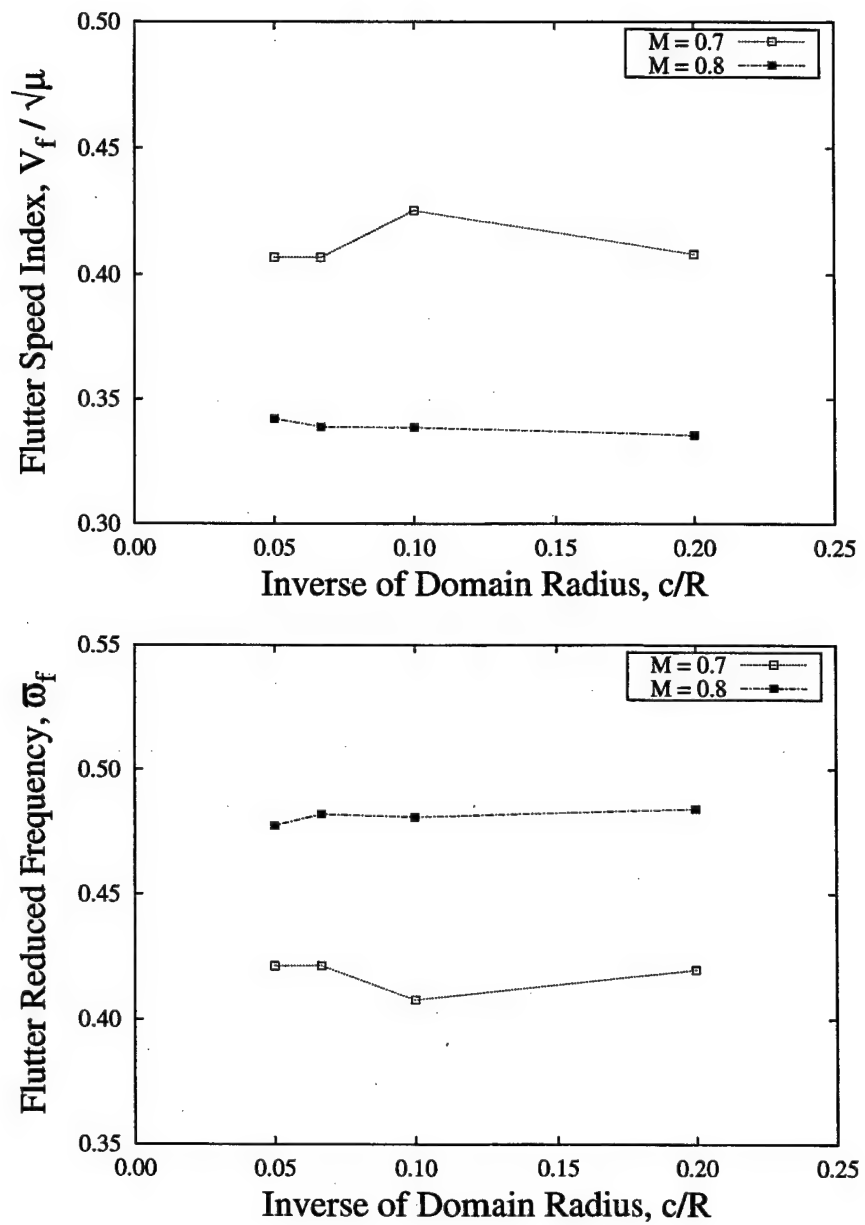
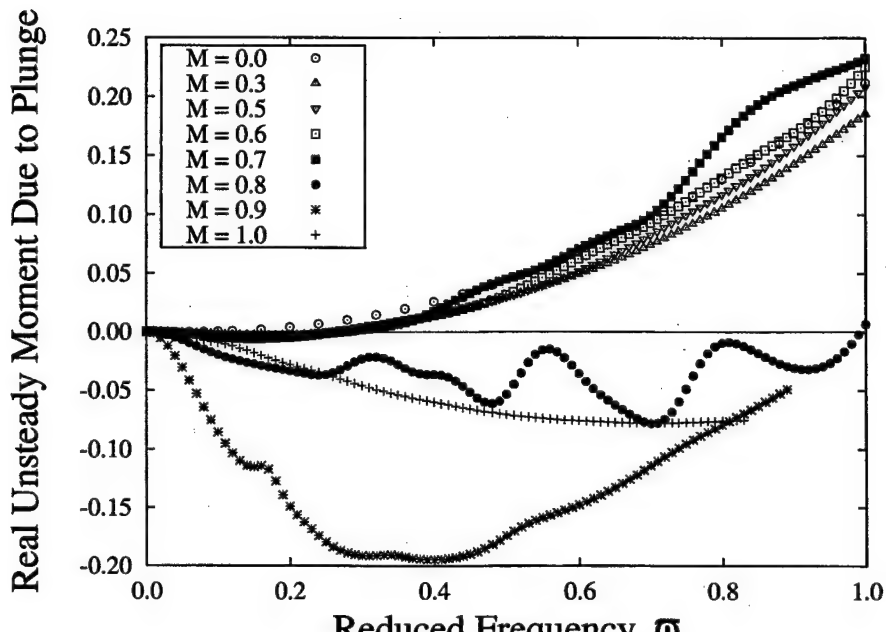


Figure 2.4: Flutter Speed Index (a) and Reduced Frequency (b) vs the Domain Radius.

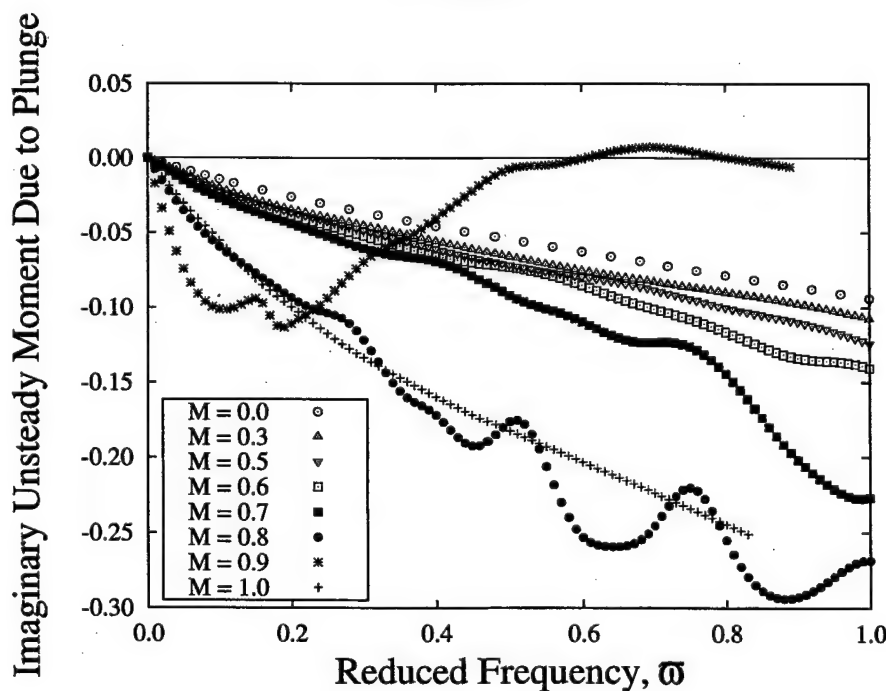
2.5 Convergence Study Results

The dependence of the calculated aerodynamic forces on the grid and domain size was investigated for Mach numbers of $M = 0.7$ and $M = 0.8$ for various values of the reduced frequency.

In the case of the grid size it was found that the variation of aerodynamic forces is monotonic and “close to linear” when plotted versus a squared measure of grid spacing. This is what one would desire since the CFD code used is a second order model in the spatial variables. The dependence of the aerodynamic forces on the domain size, however, is not monotonic. Shown here in Figs. 2.3 and 2.4 are the dependence of the flutter boundaries on the grid and domain size, respectively. In Fig. 2.3 the flutter speed index and reduced frequency appear to be nearly linear functions of the grid step. Moreover, noting the magnified scales of the vertical axes, one can conclude that flutter results (for these Mach numbers) are weakly influenced by the grid size. The flutter results in Fig. 2.4 show that increasing the domain size from $R/c = 5$ does not lead to substantial changes in the flutter velocity index or frequency. For more results on grid and domain convergence, see Ref. [33].

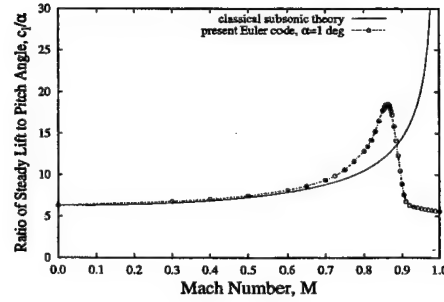


(a) $\text{Re}(\bar{c}_{m_{\bar{h}}})$

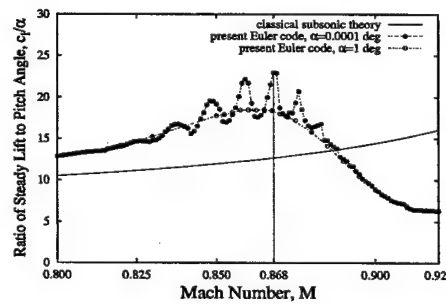


(b) $\text{Im}(\bar{c}_{m_{\bar{h}}})$

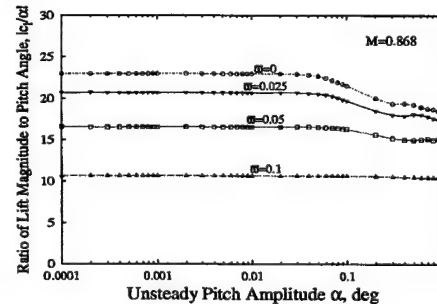
Figure 2.5: Real and Imaginary Parts of the Unsteady Aerodynamic Moment due to Plunge Motion vs Reduced Frequency $\bar{h} = 0.001$.



(a) Ratio of Steady Lift to Pitch Angle, c_l/α , vs Mach Number



(b) Ratio of Steady Lift to Pitch Angle, c_l/α , Deduced for $\alpha = 0.0001^\circ$ and 1° vs Mach Number



(c) Ratio of Lift Magnitude to Pitch Angle, $|c_l/\alpha|$, vs α for different reduced frequencies $0 \leq \bar{\omega} \leq 0.1$ at $M = 0.868$.

Figure 2.6: Lift Curve Slope Results.

2.6 Aerodynamic Lift and Moment

For a simple harmonic motion of the airfoil,

$$\frac{h}{b} = \bar{h} e^{i\omega t}, \quad \alpha = \bar{\alpha} e^{i\omega t}. \quad (2.18)$$

the aerodynamic forces will usually be periodic in time, and for aeroelastic analysis the first harmonic will be dominant. Thus to a good approximation,

$$\begin{aligned} L &= \frac{\rho U_\infty^2 c}{2} \bar{c}_l e^{i\omega t} \\ M_{\text{e.a.}} &= \frac{\rho U_\infty^2 c^2}{2} \bar{c}_m e^{i\omega t}. \end{aligned} \quad (2.19)$$

In general, the nondimensional lift and moment coefficients are expressed as

$$\begin{aligned} \bar{c}_l &= \bar{c}_l(\bar{\omega}, \text{geometry}, M, \bar{h}, \bar{\alpha}) \\ \bar{c}_m &= \bar{c}_m(\bar{\omega}, \text{geometry}, M, \bar{h}, \bar{\alpha}), \end{aligned} \quad (2.20)$$

where \bar{c}_l and \bar{c}_m are nonlinear functions of \bar{h} and $\bar{\alpha}$. However, in dynamically or time linearized aerodynamics (used in flutter analyses per se), the nondimensional lift and moment coefficients are linearly proportional to \bar{h} and $\bar{\alpha}$:

$$\begin{aligned} \bar{c}_l &= \bar{c}_{l\bar{h}}(\bar{\omega}, \text{geom}, M) \bar{h} + \bar{c}_{l\bar{\alpha}}(\bar{\omega}, \text{geom}, M) \bar{\alpha} \\ \bar{c}_m &= \bar{c}_{m\bar{h}}(\bar{\omega}, \text{geom}, M) \bar{h} + \bar{c}_{m\bar{\alpha}}(\bar{\omega}, \text{geom}, M) \bar{\alpha} \end{aligned} \quad (2.21)$$

For reference purposes, the case of zero Mach number was considered as well. The closed form expressions[33] for the lift and moment coefficients due to the pitch and plunge motion were obtained from the classical Theodorsen's formulas.

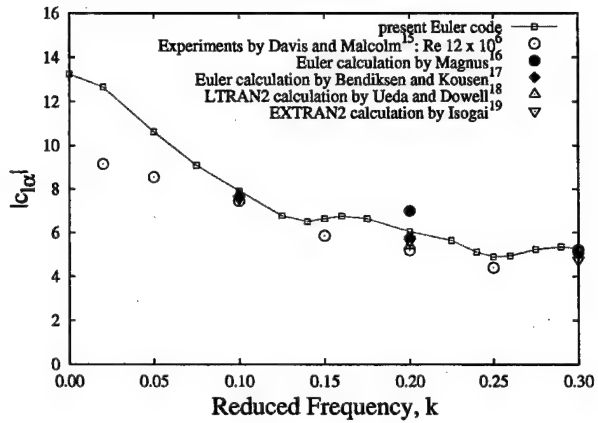
Some representative results for linear aerodynamic behavior computed by running the HB aerodynamic solver with very small amplitude motion ($\bar{h} = 0.001$) are presented in Fig. 2.5, which shows the real and imaginary parts of the aerodynamic moment due to the plunge motion, $\bar{c}_{m\bar{h}}$, versus reduced frequency. This (symmetric NACA 64A010A) airfoil has a strong shock in the range of $0.8 < M < 0.9$. For subsonic Mach numbers $0 < M < 0.7$, $\bar{c}_{m\bar{h}}$ is relatively constant (on the reduced frequency interval $[0, 1]$). For $M = 0.8$ a “wavy” pattern is very prominent in $\bar{c}_{m\bar{h}}$. This “wavy” pattern reflects the slow upstream acoustic waves typical of high subsonic/transonic flow [34]. The “wavy” pattern persists in the aerodynamic moment up to and including $M = 0.9$ (the Mach numbers of 0.82, 0.84, 0.86, and 0.88 were also studied, but the results are not shown in Fig. 2.5). At higher transonic numbers, from $M = 0.92$ and to $M = 1.0$, the shock location is at the trailing edge of the chord, the flow over the airfoil chord is supersonic, and the “wavy” pattern is no longer present. (Not plotted here are curves for Mach numbers of 0.92, 0.94, 0.96, and 0.98 as they correspond very closely to $M = 1.0$ results shown in Fig. 2.5.) The oscillatory behavior of $\bar{c}_{m\bar{h}}$ is attributed to the tendency of the fluid dynamic eigenspectrum to become less damped for transonic Mach numbers. See Ref. [23]. Previous investigators have noted that computational waviness of

this sort may be due to inadequate computational grid convergence, Ref. [35]. However, it has also been known since the classical results of Landahl [36] that such waviness may arise from physical effects. The grid convergence study previously discussed confirmed that the waviness in the present study is physical in origin.

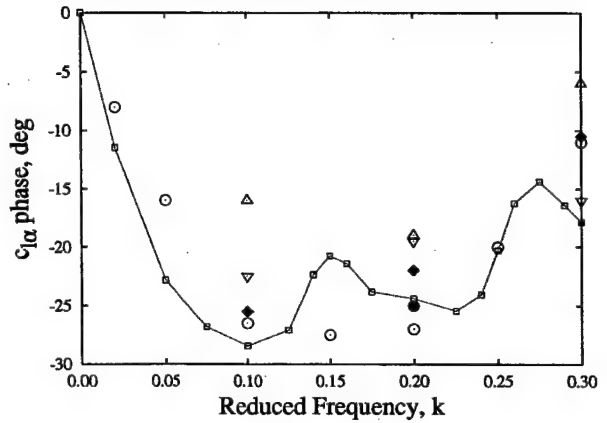
Shown in Fig. 2.6a is a plot of the ratio of steady lift to pitch angle versus Mach number (for $\bar{\omega} = 0$) as obtained from this Euler flow model. For reference the classical results as obtained from potential thin airfoil theory, $dc_l/d\alpha = 2\pi/\sqrt{1-M}$ at $\alpha = 0$, are also shown. The effects of airfoil profile (thickness) are clearly seen. Fig. 2.6a presents the Euler flow model result for c_l divided by α (in radians) for $\alpha = 1^\circ$. However, it is found that for the reduced frequency of zero, $\bar{\omega} = 0$, c_l/α is an erratic function of Mach number in the range $0.83 \leq M \leq 0.89$ for sufficiently small α , see Fig. 2.6b. Note this is true even though for a fixed M , c_l/α is a smooth function of α , see Fig. 2.6c. However, for the reduced frequencies of interest for the flutter boundaries studied here, $\bar{\omega} > 0.1$, these erratic variations in c_l/α are not present. To illustrate this the case of Mach number $M = 0.868$ is considered. As one can see in Fig. 2.6b, at this value (marked by the vertical line) of M there is a noticeable variation in the values of c_l/α with α when $\bar{\omega} = 0$. By contrast, as shown in Fig. 2.6c for $M = 0.868$, as the reduced frequency increases above $\bar{\omega} = 0.05$, the ratio of lift to pitch angle, c_l/α , is virtually constant with respect to α . Similar results were obtained for other Mach numbers, but are not presented here. It was also found that the degree of numerical smoothing in the CFD code could change the details of the results for lift at very small angles and very low reduced frequencies in the Mach number range where a rapid variation in lift occurs.

Finally, a comparison of aerodynamic transfer functions for this (NACA 64A010A) airfoil has been performed for $M = 0.8$. See Fig. 2.7. Lift $\bar{c}_{l\alpha}$ and moment $\bar{c}_{m\alpha}$ coefficients (both per radian) obtained by the present Euler code are compared to experimental values of Davis and Malcom[37], other Euler calculations performed by Magnus[38] and Bendiksen and Kousen[39]. Also shown are the results of Ueda and Dowell[40] obtained by a describing function method based on LTRAN2 solver for transonic small-disturbance potential theory as well as similar results by Isogai[41]. The results of Refs. [37, 38, 39, 40, 41] shown in Fig. 2.7 were taken from Figs. 3 and 4 of Ref. [39]. The results obtained by the present Euler code were computed using one harmonic in the aerodynamic solution. No significant variations in lift and moment coefficients for the fundamental harmonic were observed when calculations were performed using two harmonics.

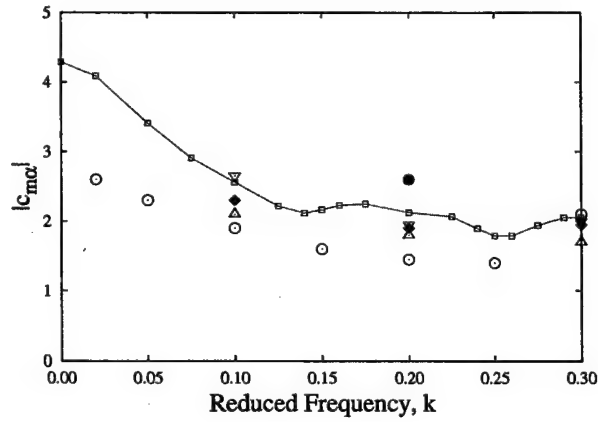
The several theoretical results shown in Fig. 2.7 for the lift and moment as a function of reduced frequency are on the whole consistent. However there is some significant variation among them especially for phase angle, but less variation for magnitude. The trends predicted by the present theory and those from experiment are in encouragingly good agreement. Previous theoretical work provided data at relatively few reduced frequencies. The computational efficiency of the present theoretical method has allowed a more complete data set to be obtained.



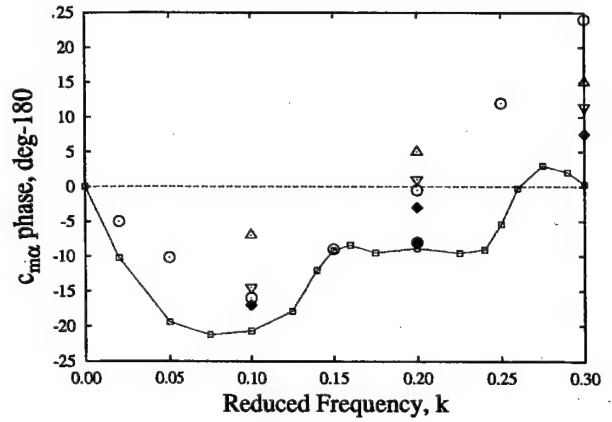
(a) Unsteady Lift due to Pitch Magnitude, $|\bar{c}_{l\alpha}|$



(b) Unsteady Lift due to Pitch Phase Angle

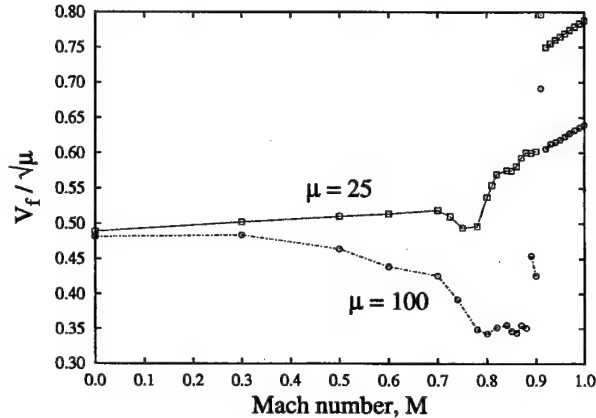


(c) Unsteady Moment due to Pitch Magnitude, $|\bar{c}_{m\alpha}|$

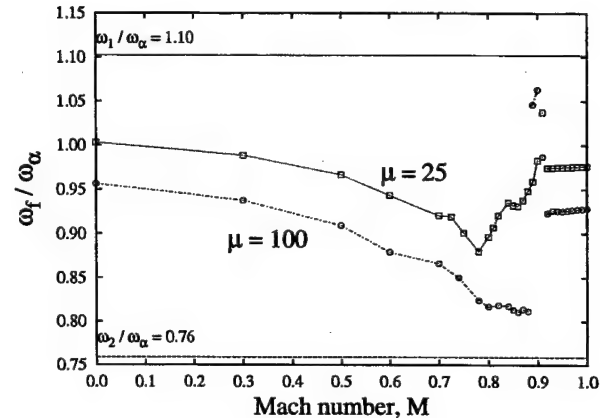


(d) Unsteady Moment due to Pitch Phase Angle

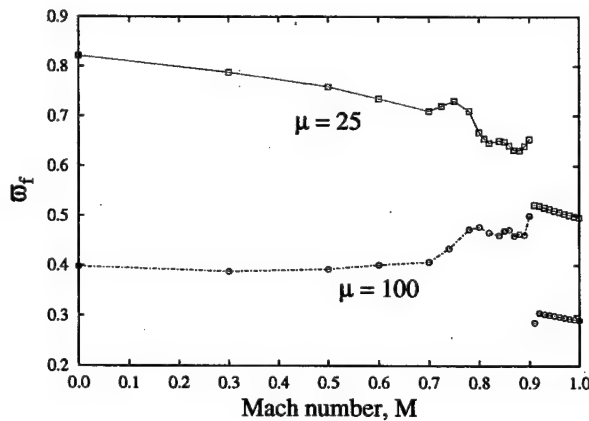
Figure 2.7: Lift and Leading-Edge Moment Coefficients (both per Radian) as Functions of Reduced Frequency $k \equiv \frac{\omega b}{U_\infty}$ due to Pitching $\pm 1^\circ$ at the quarter-chord for $M = 0.8$.



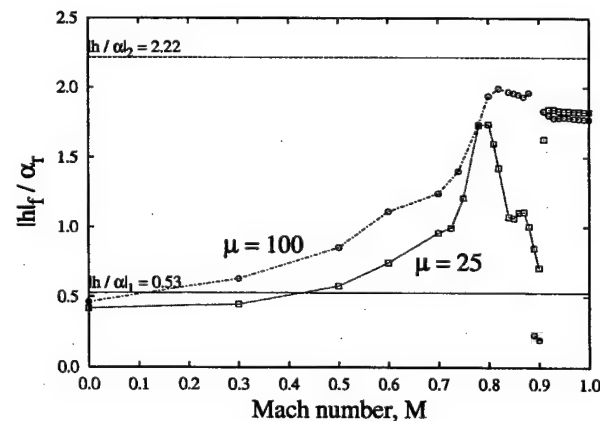
(a) Flutter Speed Index, $\frac{V_f}{\sqrt{\mu}}$



(b) Flutter Frequency Ratio, $\frac{\omega_f}{\omega_\alpha}$

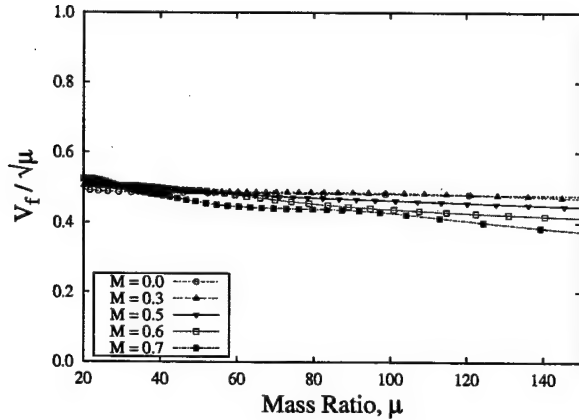


(c) Flutter Reduced Frequency, $\bar{\omega}_f$

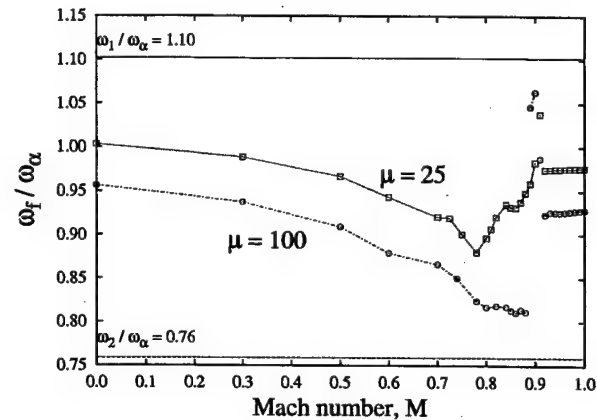


(d) Amplitude of Flutter (Aeroelastic) Eigen-vector, $|\mathbf{h}_f|/\alpha_r$

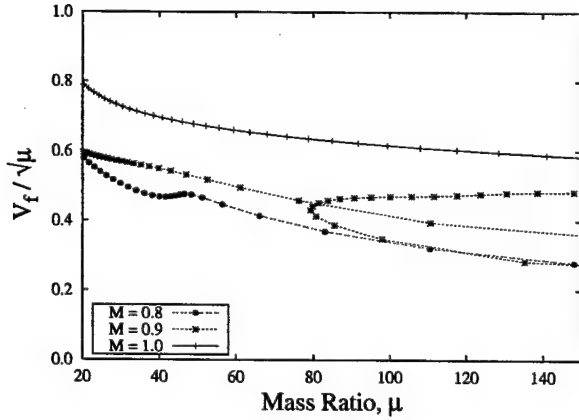
Figure 2.8: Flutter Behavior as a Function of the Mass Ratio for $\frac{\omega_h}{\omega_\alpha} = 0.5$.



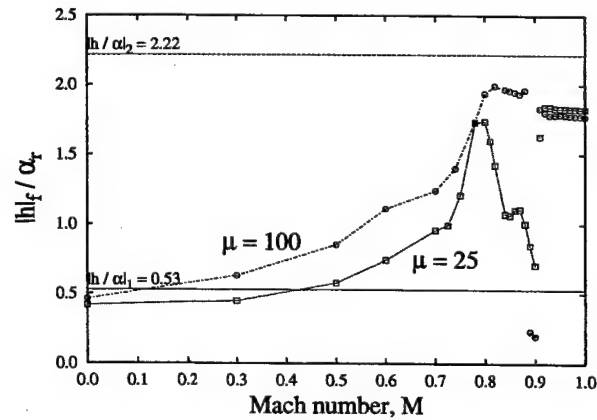
(a) Flutter Speed Index, $\frac{V_f}{\sqrt{\mu}}$



(b) Flutter Frequency Ratio, $\frac{\omega_f}{\omega_\alpha}$



(c) Flutter Speed Index, $\frac{V_f}{\sqrt{\mu}}$



(d) Amplitude of Flutter (Aeroelastic) Eigen-vector, $|h_f| / \alpha_r$

Figure 2.9: Flutter Behavior as a Function of the Mass Ratio for $\frac{\omega_h}{\omega_\alpha} = 0.8$.

2.6.1 Mass Ratio Effect

Dependence of the flutter boundaries (flutter speed index, flutter frequency and eigenvector) on the mass ratio, μ , was investigated first. Two cases for the ratio of uncoupled frequencies are presented here: $\omega_h/\omega_\alpha = 0.5$ (Fig. 2.8) and $\omega_h/\omega_\alpha = 0.8$ (Fig. 2.9).

$\frac{\omega_h}{\omega_\alpha} = 0.5$:

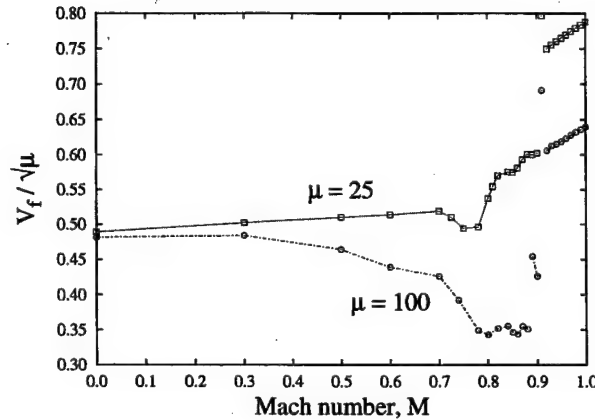
For $\omega_h/\omega_\alpha = 0.5$, the flutter speed index (Fig. 2.8a) is seen to be weakly dependent on μ for subsonic Mach numbers. For transonic Mach numbers of $M = 0.8$ and $M = 0.9$ the flutter speed index decreases with μ at a much higher rate. For $M = 1.0$ the flutter speed index becomes very large (well beyond the scale of the graph). Note that the flutter reduced frequency (Fig. 2.8c) for $M = 0.9$ is distinctly higher than for other Mach numbers. The flutter frequency (Fig. 2.8b) and flutter eigenvector (Fig. 2.8d) are also less sensitive to mass ratio at low subsonic Mach numbers with a more significant dependency occurring at higher subsonic and transonic Mach numbers. Coupled in vacuuuo natural frequencies, ω_1 and ω_2 , were also computed for easy reference and as can be seen in Fig. 2.8b, the flutter motion is pitch dominated for $M = 0.9$. One may also see this from Fig. 2.8d, where coupled in vacuuuo eigenvectors, $(h/\alpha)_1$ and $(h/\alpha)_2$, are indicated. The flutter eigenvector for $M = 0.9$ is essentially the same as $(h/\alpha)_1$, which corresponds to the pitch dominated mode. This is an example of single DOF flutter, but note the critical aeroelastic mode is a *coupled* natural mode, albeit one that is pitch dominated.

$\frac{\omega_h}{\omega_\alpha} = 0.8$:

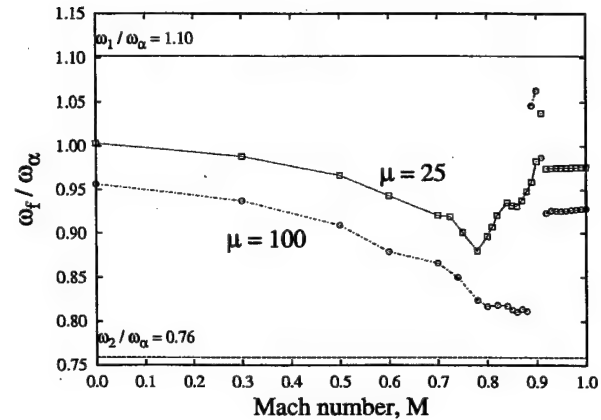
For $\omega_h/\omega_\alpha = 0.8$, the flutter speed index (Fig. 2.9a) is even more weakly dependent on μ for subsonic Mach numbers. In Fig. 2.9c, the flutter speed index behavior for transonic Mach numbers of $M = 0.8$, $M = 0.9$ and $M = 1.0$ is shown. As in the case of $\omega_h/\omega_\alpha = 0.5$, the flutter speed index for the transonic Mach numbers is more sensitive to μ than for the lower, subsonic Mach numbers. Moreover, for this frequency ratio, when $M = 0.9$, multiple flutter velocities occur for mass ratios $\mu \geq 80$. To determine the stability of the regions created by such multiple branches of flutter boundaries a root-loci analysis for fixed values of ω_h/ω_α and μ can be employed [42, ?, 43] using reduced order aerodynamic models. However in this study only flutter boundaries were determined. The flutter frequency (Fig. 2.9b) and flutter eigenvector (Fig. 2.9d) are distributed over the full range between coupled natural frequencies and eigenvectors and none of Mach number cases appears to be primarily pitch or plunge dominated.

2.6.2 Ratio of Uncoupled Natural Frequencies Effect

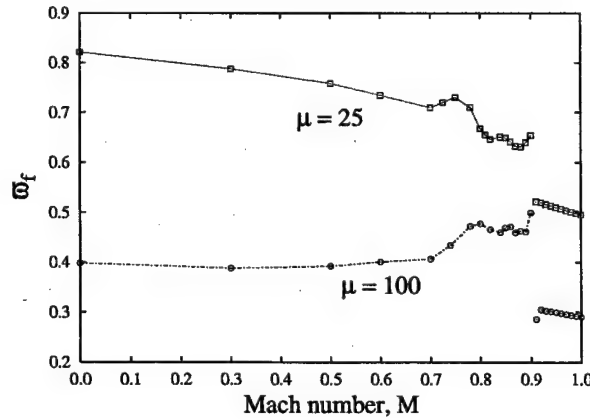
Dependence of the flutter boundary on the ratio of uncoupled natural frequencies, ω_h/ω_α , is next investigated, and two mass ratios are considered: $\mu = 25$ (Fig. 2.10 and 2.11) and $\mu = 100$ (Fig. 2.12).



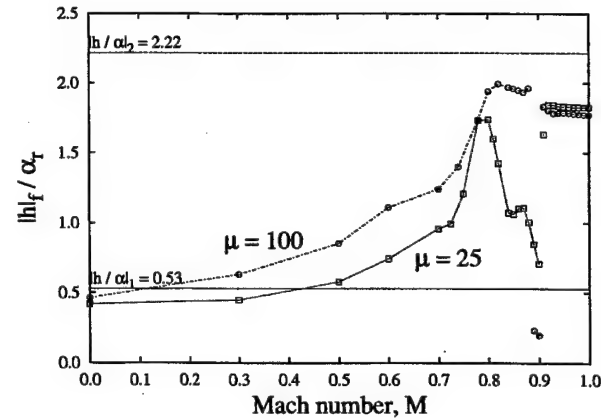
(a) Flutter Speed Index, $\frac{V_f}{\sqrt{\mu}}$



(b) Flutter Frequency Ratio, $\frac{\omega_f}{\omega_\alpha}$

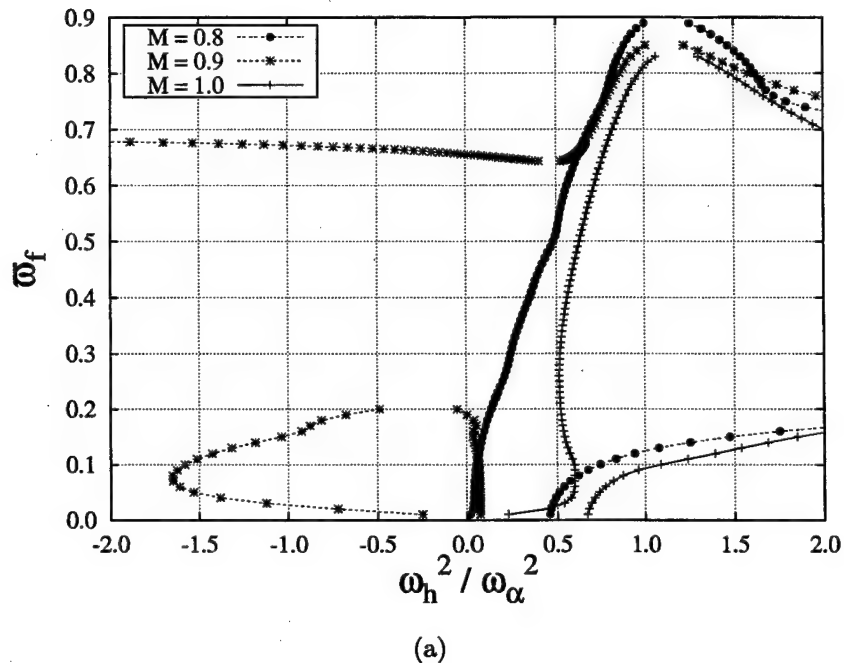


(c) Flutter Reduced Frequency, $\bar{\omega}_f$

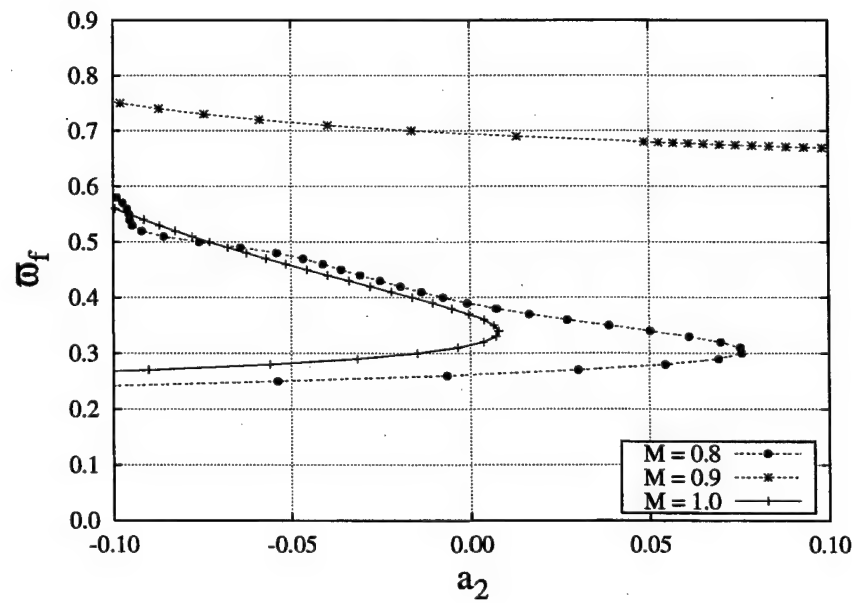


(d) Amplitude of Flutter (Aeroelastic) Eigen-vector, $|h_f|/\alpha_r$

Figure 2.10: Flutter Behavior as a Function of the Ratio of Uncoupled Frequencies for $\mu = 25$.

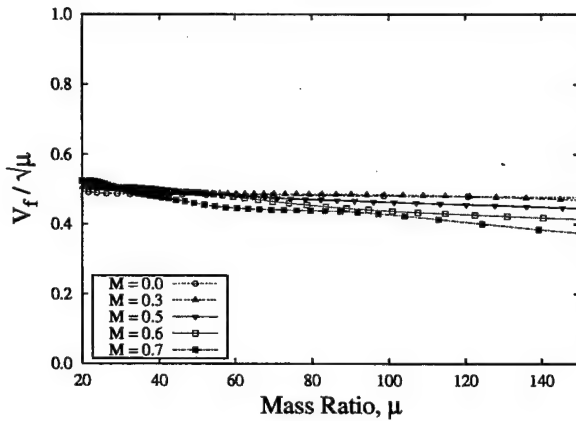


(a)

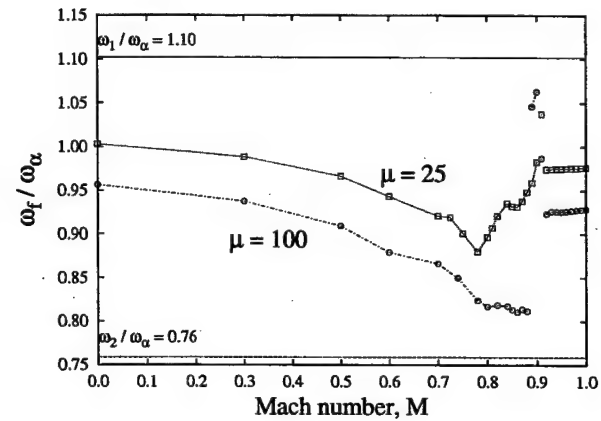


(b)

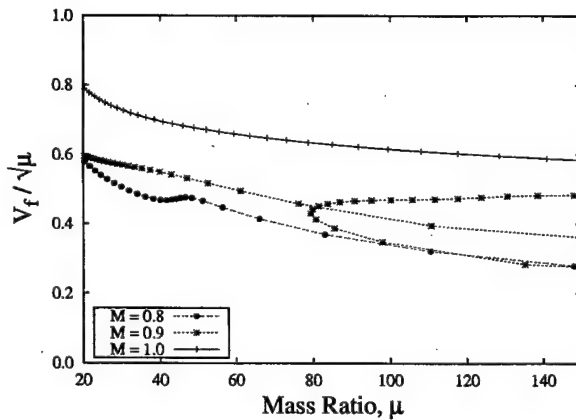
Figure 2.11: Flutter Reduced Frequency, $\bar{\omega}_f$, versus a) $\frac{\omega_h^2}{\omega_\alpha^2}$ and b) the coefficient a_2 of $a_2(\frac{\omega_h^2}{\omega_\alpha^2})^2 + a_1 \frac{\omega_h^2}{\omega_\alpha^2} + a_0 = 0$ for $\mu = 25$.



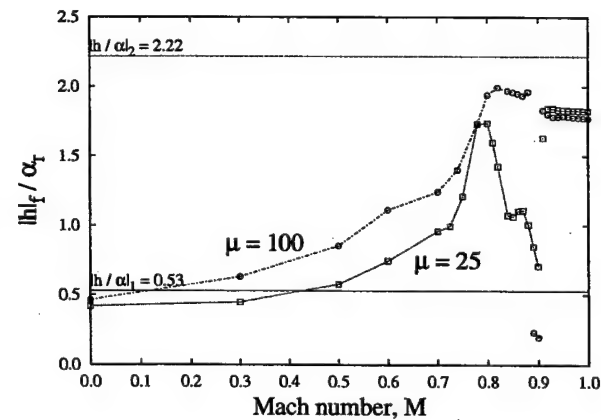
(a) Flutter Speed Index, $\frac{V_f}{\sqrt{\mu}}$



(b) Flutter Frequency Ratio, $\frac{\omega_f}{\omega_\alpha}$



(c) Flutter Speed Index, $\frac{V_f}{\sqrt{\mu}}$



(d) Amplitude of Flutter (Aeroelastic) Eigen-vector, $|\mathbf{h}_f|/\alpha_r$

Figure 2.12: Flutter Behavior as a Function of the Ratio of Uncoupled Frequencies for $\mu = 100$.

$\mu = 25$:

For $\mu = 25$, the flutter speed index (Fig. 2.10a) has a minimum near $\omega_h/\omega_\alpha = 1$. For typical airfoils, ω_h/ω_α is usually between 0.2 and 0.8. In that range, the flutter speed index decreases steadily and is almost constant for Mach numbers less than 0.7. However, as can be seen and is well known, the flutter speed index becomes very sensitive to the Mach number for high subsonic or transonic conditions.

For a better understanding of how the flutter speed index results are obtained one can show that the flutter reduced velocity may be expressed as

$$V_f^2 = \frac{d_1 \frac{\omega_h^2}{\omega_\alpha^2} + d_2}{d_3}, \quad (2.22)$$

where d_1 , d_2 , and d_3 are coefficients dependent on the reduced frequency. Eq. (2.22) is obtained from the imaginary part of Eq. (??). Substitution of Eq. (2.22) into the real part of Eq. (??), leads to a quadratic equation in $\omega_h^2/\omega_\alpha^2$,

$$a_2 \left(\frac{\omega_h^2}{\omega_\alpha^2} \right)^2 + a_1 \frac{\omega_h^2}{\omega_\alpha^2} + a_0 = 0 \quad (2.23)$$

with the roots given by

$$\left(\frac{\omega_h^2}{\omega_\alpha^2} \right)_{1,2} = \frac{-a_1 \pm \sqrt{a_1^2 - 4a_2a_0}}{2a_2}, \quad (2.24)$$

where the coefficients a_i may also change the sign for different $\bar{\omega}$. Obviously, only positive real values of $\omega_h^2/\omega_\alpha^2$ in Eq. (2.24) have physical meaning. Moreover, only such values of $\omega_h^2/\omega_\alpha^2$ are kept for which V_f^2 in Eq. (2.22) is positive. Real roots of Eq. (2.24) are shown in Fig. 2.11a. When the coefficient a_2 passes through zero, branches of $\omega_h^2/\omega_\alpha^2$ asymptotically go to $\pm\infty$. The dependence of a_2 with respect to $\bar{\omega}_f$ is shown in Fig. 2.11b. For example, in Fig. 2.10c for $M = 0.9$, a_2 goes through zero at $\bar{\omega}_f \simeq 0.7$, which is when the branches of $\omega_h^2/\omega_\alpha^2$ go to $\pm\infty$ in Fig. 2.11a.

Note that the difference between the two coupled natural frequencies (ω_1 and ω_2 as indicated in Fig. 2.10b) is the smallest near $\omega_h/\omega_\alpha = 1$. This is likely responsible for the minimum in the flutter speed index in the vicinity of that point: the closer the coupled natural frequencies are initially, the more readily, when increasing velocity, “coalescence” or “merging frequency” flutter can occur (see p. 112 of Ref. [34]).

$\mu = 100$:

For $\mu = 100$, the flutter speed index (Fig. 2.12a and c) again has the tendency to have a minimum near $\omega_h/\omega_\alpha = 1$, and especially so for subsonic Mach numbers (Fig. 2.12a). As in

the case for $\mu = 25$, the flutter speed index is nearly constant with M for subsonic conditions. At higher transonic Mach numbers (Fig. 2.12c), the flutter speed index becomes very sensitive to Mach number.

This behavior is associated with the “transonic flutter dip”. Also note that the flutter speed index can be a multivalued function of ω_h/ω_α for $M = 0.8$ and $M = 0.9$.

Note that (Fig. 2.12b) the flutter frequency is very close to the coupled natural pitch frequency, ω_1/ω_α , for $M = 0.9$ (pitch dominated motion). This is indicative of “single-degree-of-freedom” flutter (see p. 113 of Ref. [34]).

2.6.3 Mach Number Effect

The dependence of the flutter boundary on Mach number (see Figs. 2.13 and 2.14) for the cases of $\mu = 25, 100$ and $\omega_h/\omega_\alpha = 0.5, 0.8$ is presented next.

$$\frac{\omega_h}{\omega_\alpha} = 0.5:$$

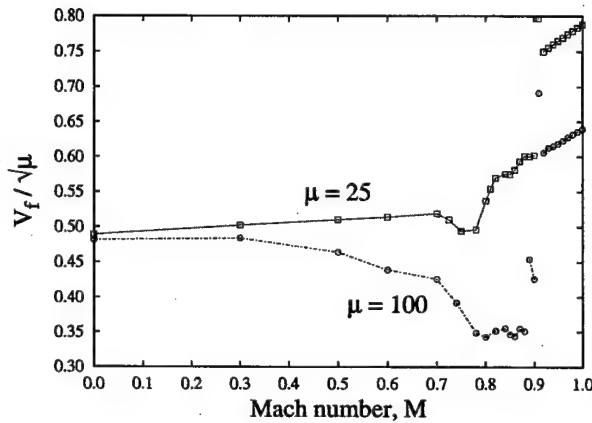
Fig. 2.13 shows the flutter boundary behavior versus Mach number for $\omega_h/\omega_\alpha = 0.5$. Squares represent the case of $\mu = 25$ and circles the case of $\mu = 100$. Note a rather weak dependence of the flutter boundaries on the mass ratio.

As the Mach number is increased past $M = 0.8$, a sharp drop in the flutter reduced frequency occurs. That is accompanied by a sharp increase in the flutter speed index. As the Mach number is increased further, another branch of flutter points appears. These low flutter speed index values correspond to the “transonic flutter dip”.

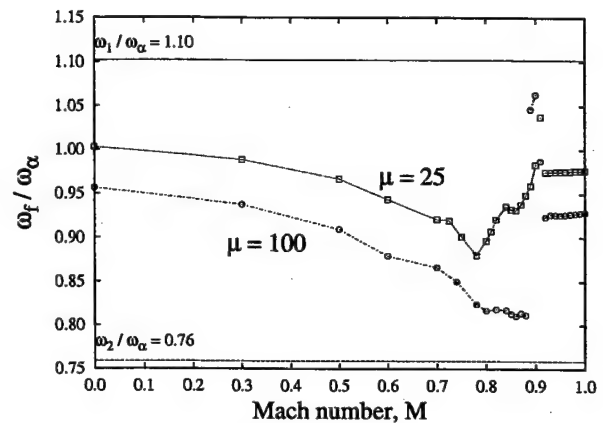
For an explanation to the abrupt change in flutter mode at $M = 0.82$ and $M = 0.91$ one may ask whether the steady flow shock position is changing and where the shock location is relative to the elastic axis and mode nodes.

The steady flow pressure contours for $M = 0.81$ and $M = 0.82$ did not show any significant changes in the pressure distribution. However the situation is different for Mach numbers above $M = 0.9$. Here the location of the shock moves to the trailing edge as the Mach number is increased above $M = 0.9$. For $\omega_h/\omega_\alpha = 0.8$, the flutter behavior also changes in the vicinity of these Mach numbers. Note that in the Mach number range $0.82 < M < 0.92$ (Fig. 2.15) the position of the shock on the airfoil moves appreciably. To develop an improved understanding of the behavior of the flutter boundaries one could perform a root locus analysis which would enable one to view the migration of the aeroelastic eigenvalues as a function of the nondimensional airspeed for each Mach number. Representative root locus analyses for transonic Mach numbers of similar airfoil models can be found in Refs. [42, 30, 43]. Root loci however have not been part of the present study.

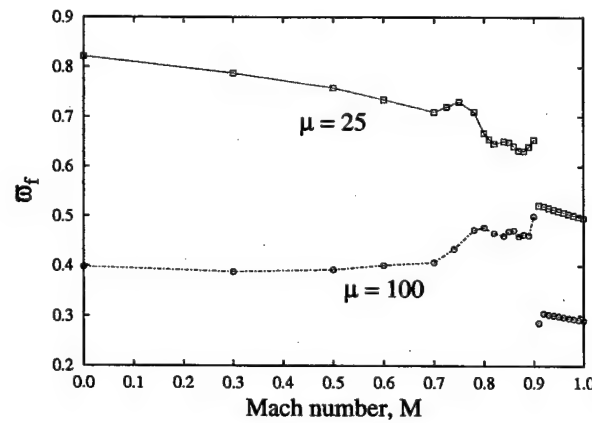
The reduced flutter frequency behavior is shown in Fig. 2.13c. For subsonic and low transonic



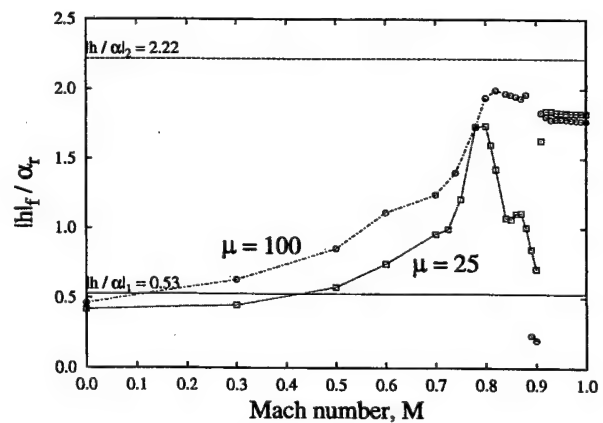
(a) Flutter Speed Index, $\frac{V_f}{\sqrt{\mu}}$



(b) Flutter Frequency Ratio, $\frac{\omega_f}{\omega_\alpha}$

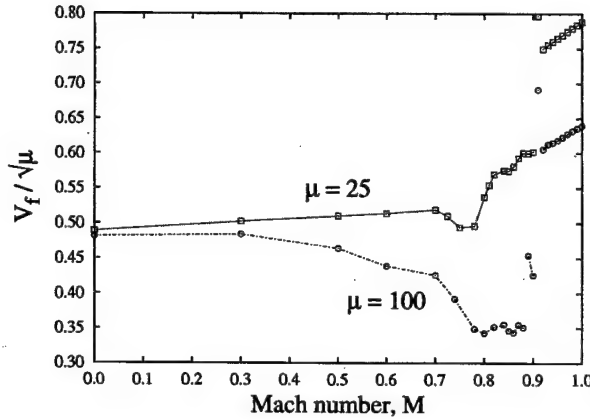


(c) Flutter Reduced Frequency, $\bar{\omega}_f$

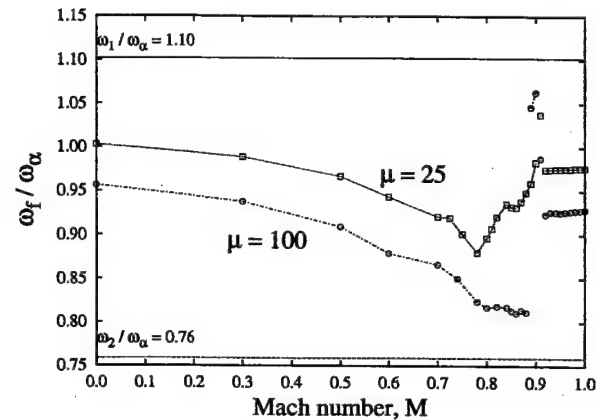


(d) Amplitude of Flutter (Aeroelastic) Eigenvector, $|h_f|/\alpha_r$

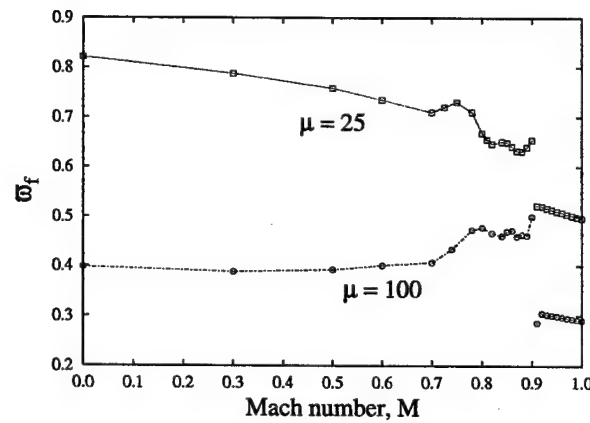
Figure 2.13: Flutter Behavior as a Function of Mach Number for $\frac{\omega_h}{\omega_\alpha} = 0.5$ and $\mu = 25, 100$.



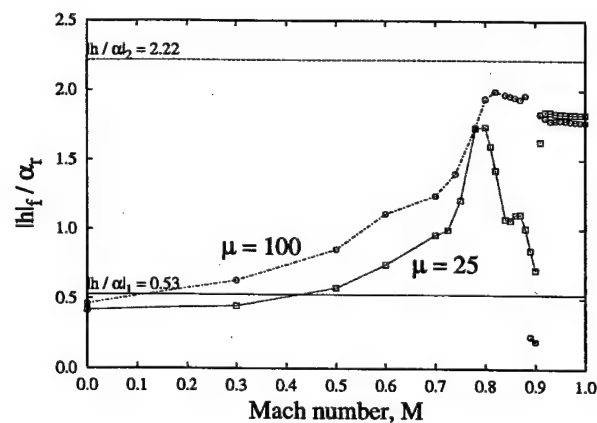
(a) Flutter Speed Index, $\frac{V_f}{\sqrt{\mu}}$



(b) Flutter Frequency Ratio, $\frac{\omega_f}{\omega_\alpha}$



(c) Flutter Reduced Frequency, $\bar{\omega}_f$



(d) Amplitude of Flutter (Aeroelastic) Eigen-vector, $|\mathbf{h}_f|/\alpha_r$

Figure 2.14: Flutter Behavior as a Function of Mach number for $\frac{\omega_h}{\omega_\alpha} = 0.8$ and $\mu = 25, 100$.

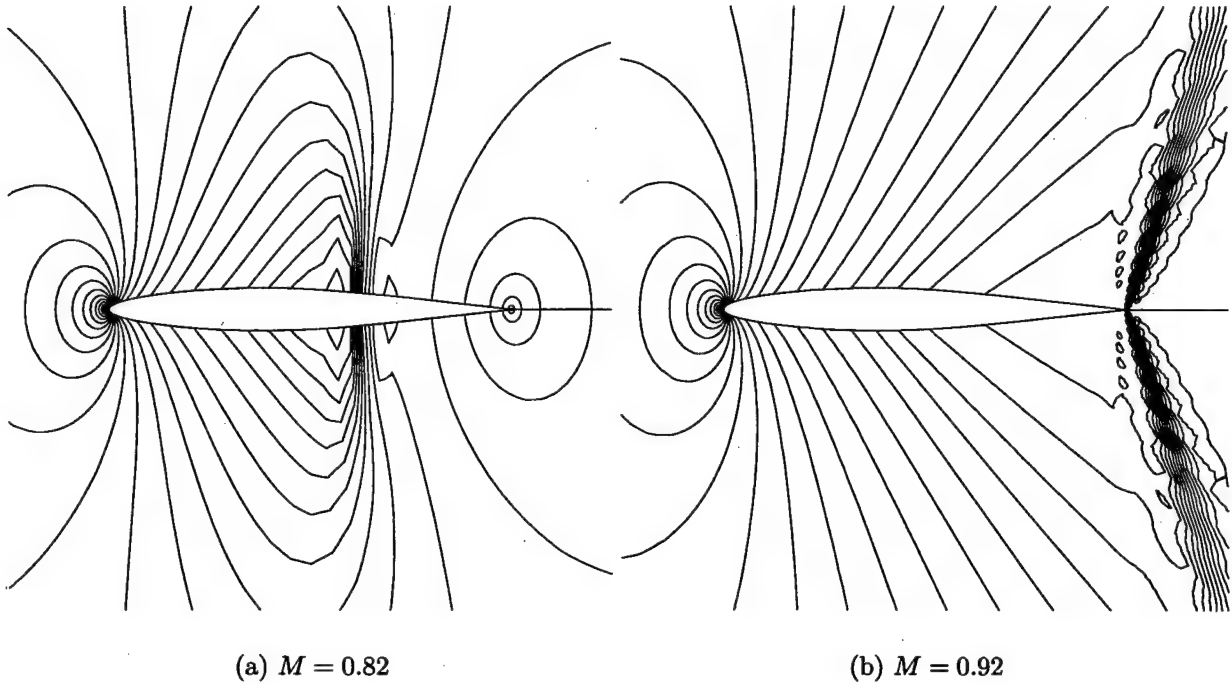


Figure 2.15: Steady Flow Pressure Contours.

Mach numbers ($0 \leq M \leq 0.8$), $\bar{\omega}_f$ is much higher for the lower mass ratio ($\bar{\omega}_f \approx 0.4$) than for the higher mass ratio ($\bar{\omega}_f \approx 0.2$). At high transonic Mach numbers ($0.82 \leq M < 0.92$), the flutter reduced frequency is about the same for either mass ratio.

The flutter (aeroelastic) eigenvector is shown in Fig. 2.13d and provides a possible explanation for the low flutter speed index values for the transonic dip Mach number region. In this range, the flutter mode becomes pitch dominated for both values of mass ratio. The flutter mode is markedly different from that for $M < 0.82$, for example.

$$\frac{\omega_h}{\omega_\alpha} = 0.8:$$

The flutter speed index for $\omega_h/\omega_\alpha = 0.8$ is shown in Fig. 2.14a. For this rather high value of pitch to plunge frequency ratio, there is no transonic dip in the flutter speed index at the lower mass ratio. Moreover the system appears to be more stable at the high transonic Mach numbers. For the higher mass ratio as the Mach number increases, the flutter velocity index reaches its minimum in the range $0.78 < M < 0.88$. The flutter mode then appears to change twice for even higher Mach numbers. Contrary to the results for $\omega_h/\omega_\alpha = 0.5$, here the flutter frequency shown in Fig. 2.14b is not very close to either the pitch or plunge coupled natural frequency. So the flutter mode (Fig. 2.14d) is not a single degree of freedom flutter motion, but rather a combined pitch-plunge motion.

Conclusions

Using a state of the art Euler based time linearized aerodynamic code, an investigation is presented of how structural and aerodynamic parameters including freestream (transonic) Mach number affect flutter and LCO characteristics of a "typical" two degree-of-freedom airfoil configuration. Convergence of the CFD code with respect to grid spacing and computational domain size was also considered.

The following conclusions have been drawn:

- I When examining the dependence of the flutter on the mass ratio, μ , it was found that the flutter variables (i.e. reduced velocity, frequency and structural eigenmode) vary little with μ , especially for subsonic Mach numbers.
- II As expected, a study of the effect of the ratio of uncoupled natural frequencies, ω_h/ω_α , determined that flutter reduced velocities have a minimum near $\omega_h/\omega_\alpha \approx 1$. Multiple values of the flutter velocity can occur at high transonic Mach numbers for some ω_h/ω_α .
- III Most significantly perhaps, it was demonstrated that flutter solutions are very sensitive to Mach number especially in the transonic range. Depending on the frequency and the mass ratios, there may or may not be sudden and significant changes (e.g. the "transonic dip") in the flutter reduced velocity and the type of flutter motion as the Mach number is varied.
- IV Finally it is noted that viscous effects may be important. It has been our experience that when the aerodynamic flow is attached an inviscid analysis is adequate, but for separated flows a viscous analysis is required.

An extensive parameter analyses of an airfoil aeroelastic configuration has been achieved using a highly efficient time linearized CFD computational technique. Correlation with experiment remains an open challenge, however a comparison of results from our CFD model with results from an unsteady aerodynamic experiment by Davis and Malcom[37] for lift and moment shows encouraging agreement.

Nomenclature

a = nondimensional location of airfoil elastic axis, $a = e/b$
 b, c = semi-chord and chord, respectively
 \bar{c}_l, \bar{c}_m = first harmonic coefficient of lift and moment about elastic axis, respectively
 $\bar{c}_{l_h}, \bar{c}_{l_\alpha}$ = first harmonic coefficient of lift due to plunge and pitch motions, respectively
Note: $\bar{c}_{l_\alpha} \equiv \bar{c}_l/\bar{\alpha}$ for $\bar{h} \equiv 0$, as $\bar{\alpha} \rightarrow 0$ $\bar{c}_{l_\alpha} = d\bar{c}_l/d\bar{\alpha}|_{\bar{\alpha}=0}$.
Similar definitions hold for $\bar{c}_{l_h}, \bar{c}_{m_h}$ and \bar{c}_{m_α} .
 $\bar{c}_{m_h}, \bar{c}_{m_\alpha}$ = first harmonic coefficient of moment due to plunge and pitch motions, respectively
 e = location of airfoil elastic axis, measured positive aft of airfoil midchord
 h, α = airfoil plunge and pitch degree-of-freedom, respectively

$\bar{h}, \bar{\alpha}$	= first harmonic amplitude of plunge nondimesionalized by semi-chord, $\bar{h} = h/b$, and pitch motion, respectively
h_{avr}	= “averaged” grid step in the radial direction, $h_{avr} \equiv (R/c - 1/2)/(N_r - 1)$
I_α	= second moment of inertia about elastic axis
$L, M_{e.a.}$	= lift and moment about elastic axis, respectively
K_h, K_α	= airfoil plunge stiffness and torsional stiffness about elastic axis, respectively
k	= reduced frequency based on airfoil semi-chord, $k \equiv \omega b/U_\infty$
M	= freestream Mach number
m	= airfoil sectional mass
μ	= mass ratio, $\mu \equiv m/\pi \rho_\infty b^2$
N	= number of harmonics used in harmonic balance solver
N_r, N_Θ	= number of grid points in radial and circumferential direction, respectively
R	= radius of computational domain
r_α	= radius of gyration of airfoil about elastic axis, $r_\alpha^2 \equiv I_\alpha/m b^2$
S_α	= first moment of inertia about elastic axis
U_∞	= freestream velocity
V	= reduced velocity, $V \equiv U_\infty/\omega_\alpha b$
$V_f/\sqrt{\mu}$	= flutter speed index, $V_f/\sqrt{\mu} \equiv U_{\infty f}/\sqrt{\mu} \omega_\alpha b$
$\omega, \bar{\omega}$	= frequency and reduced frequency based on airfoil chord, $\bar{\omega} \equiv \omega c/U_\infty$
ω_α, ω_h	= uncoupled natural frequencies of pitch and plunge DOF
ω_1, ω_2	= coupled structural natural frequencies
x_α	= airfoil static unbalance, $x_\alpha \equiv S_\alpha/m b$

Subscripts

f	= flutter onset condition
-----	---------------------------

Chapter 3

Transonic Flutter and LCO in Nonlinear Viscous Two Dimensional Flow: Frequency Domain

Summary

- As an improvement to the inviscid model presented in the previous chapter, the effects of viscosity have been added and initial results obtained for LCO. Comparisons have been made with the results of more computationally intensive time marching CFD solutions and also with the results of experiments done at DLR in Göttingen on a supercritical airfoil. The HB and time marching results are in good agreement, but because of the greater computational efficiency of the HB method a much broader range of parameter values has been considered which allows a more complete comparison with the experimental data. Based upon the calculations done to date, it appears that the effects of viscosity on LCO are most pronounced when flow separation occurs as is the case for the DLR study of a supercritical airfoil. On the other hand, for the attached flows that occur for a conventional airfoil (NACA 64A010) at small mean angle of attack, the results from the inviscid and viscous flow calculations are more closely correspond.
- The work in this chapter has been presented at the AIAA/SDM 2002 Conference: "J.P. Thomas, E.H. Dowell, and K.C. Hall, Modeling of Viscous Transonic Limit Cycle Oscillation Behavior Using a Harmonic Balance Approach, AIAA Paper 2002-1414, presented at the AIAA/ASEM/ASCE/AHS SDM Conference, April 2002, Denver, CO.", it starts with the following abstract:
- Presented is a harmonic-balance computational fluid dynamic approach for modeling limit cycle oscillation behavior of aeroelastic airfoil configurations in a viscous transonic flow. For the NLR 7301 airfoil configuration studied, accounting for viscous effects is shown to significantly influence computed limit cycle oscillation trends when compared to an inviscid analysis. Methodology for accounting for changes in mean angle-of-attack during limit cycle oscillation is also developed.

3.1 Introduction

A novel approach for modeling limit cycle oscillation (LCO) behavior of aeroelastic airfoil configurations in viscous transonic flows is presented. The method is based on a harmonic balance (HB) flow solver technique for efficiently modeling nonlinear unsteady aerodynamics (see Hall et. al. [44] and Thomas et. al. [45]). The primary objective of the current study is to assess the capability of the HB/LCO solution methodology to model transonic viscous flow phenomena such as shock induced boundary layer separation, and to determine if such effects have an influence on LCO behavior. Recent two-dimensional experimental LCO investigations by Schewe et. al. [46, 47] and Knipfer and Schewe [48] have also motivated the present research. In addition to viscous effects, and unlike the NACA 64A010 airfoil configuration studied in Thomas et. al. [45], we now also consider nonsymmetric airfoil sections at nonzero angles-of-attack. As will be shown in the following, this requires the solution of one additional equation for the mean (i.e. zeroth harmonic) angle-of-attack of the LCO.

The primary motivation for developing the HB/LCO solution methodology has been to construct an efficient computational procedure for modeling LCO behavior. Figure 3.1a illustrates a "typical" flutter onset boundary in the reduced velocity versus Mach number plane, including the commonly observed "flutter speed dip". As one moves from point A, a reduced velocity below the flutter onset condition, to point B, a reduced velocity above the flutter onset condition, LCO may be encountered. Figure 3.1b illustrates three possible types of LCO behavior one might observe.

Curve I represents a stable LCO behavior with no LCO occurring below the linear flutter speed. This type of LCO behavior is also sometimes referred to as "soft flutter" or "benign LCO" per se in that the nonlinear effects help to reduce the amplitude of the oscillations. Of course, structural failure may eventually be an issue if the amplitude of the LCO becomes too large. For the type of LCO behavior illustrated by Curve II, as soon as one reaches the flutter onset condition, any further increase in reduced velocity immediately results in very large LCO motion. Finally, curve III illustrates unstable LCO behavior. A configuration exhibiting this very dangerous type of LCO trend is susceptible to "explosive" LCO whereby a disturbance of sufficient magnitude may be capable of triggering LCO at reduced velocities even below the flutter onset condition. As will be shown, the HB/LCO solution methodology is a computationally efficient technique for determining such LCO trends.

3.2 Theoretical Development

3.2.1 Fluid Dynamic Model

For the model configuration studied in this investigation, we consider both viscous and inviscid fluid dynamic models. The harmonic balance flow solver technique provides an efficient method for modeling nonlinear unsteady aerodynamic effects for finite amplitude motions of a prescribed frequency.

As is discussed in Hall et. al. [44] and Thomas et. al. [45], the HB method is implemented within the framework of a conventional CFD solver. The vector of unsteady flow conservation variables $\mathbf{U}(\mathbf{x}_i, t)$ at each computational mesh point \mathbf{x}_i is approximated in a truncated Fourier expansion as

$$\mathbf{U}(\mathbf{x}_i, t) \approx \sum_{n=-N_H}^{N_H} \hat{\mathbf{U}}_n(\mathbf{x}_i) e^{jn\omega t} \quad (3.1)$$

where $\hat{\mathbf{U}}_n(\mathbf{x}_i)$ is the n^{th} harmonic coefficient, and N_H is number of harmonics used in the expansion. McMullen et. al. [49, 50] are also investigating a similar expansion technique for unsteady Euler and Navier-Stokes flows.

Normally, the harmonic balance development proceeds by first substituting Eq. 3.1 into the governing flow equations. One then subsequently goes through the process of "balancing" all the resulting terms proportional to $e^{jn\omega t}$ for each n ($-N_H \leq n \leq N_H$). This in turn yields $2N_H + 1$ equations for the $2N_H + 1$ harmonic coefficients $\hat{\mathbf{U}}_n$. This straight-forward approach to the harmonic balance formulation is however typically difficult to implement for complex systems of equations such as those arising from Euler and Navier-Stokes flows.

Hall et. al. [44] however recently devised an alternative approach to the harmonic balance derivation whereby the method is formulated in terms of time-domain variables. That is, instead of working in terms of the Fourier coefficient variables $\hat{\mathbf{U}}_n(\mathbf{x}_i)$, one instead considers as dependent variables, flow solutions stored at $2N_H + 1$ equally spaced "sub-time" levels ($\mathbf{U}(\mathbf{x}_i, t_n)$) over the period of one cycle of motion. The Fourier and time-domain variables are in fact related to one another via a constant Fourier transformation matrix.

Working in terms of "sub-time" level variables circumvents the necessity of having to go though the "balancing" step of the HB method, and in fact, it allows one to easily formulate the harmonic balance technique within the framework of an existing steady CFD solver (See Hall et. al. [44] and Thomas et. al. [45] for further details). For the results presented here, the CFD method is a variant of standard Lax-Wendroff scheme [51, 52] in conjunction with the one-equation turbulence model of Spalart and Allmaras [53].

3.2.2 Two-Dimensional Airfoil Aeroelastic Model

The frequency domain form of the unsteady aeroelastic equations governing the "typical" pitch/plunge airfoil configuration (Fig. 3.2) can be written as

$$\mathbf{G}\mathbf{u} = \frac{V^2}{\pi} \mathbf{f}, \quad (3.2)$$

where

$$\mathbf{G} = -\frac{\mu}{4} \bar{\omega}^2 V^2 \mathbf{M} + j\sqrt{\mu} \bar{\omega} V \mathbf{D} + \mathbf{K}, \quad (3.3)$$

and

$$\mathbf{M} = \begin{bmatrix} m_h/m & x_\alpha \\ x_\alpha & r_\alpha^2 \end{bmatrix}, \quad \mathbf{D} = \begin{bmatrix} \zeta_h(\omega_h/\omega_\alpha) & 0 \\ 0 & \zeta_\alpha r_\alpha^2 \end{bmatrix},$$

$$\mathbf{K} = \begin{bmatrix} (\omega_h/\omega_\alpha)^2 & 0 \\ 0 & r_\alpha^2 \end{bmatrix}, \quad \mathbf{u} = \begin{Bmatrix} \bar{h}_1/b \\ \bar{\alpha}_1 \end{Bmatrix}, \quad \mathbf{f} = \begin{Bmatrix} -\bar{c}_{l_1} \\ 2\bar{c}_{m_1} \end{Bmatrix}. \quad (3.4)$$

3.2.3 Static Aeroelastic Equation

For the present investigation, since nonsymmetric airfoil sections and/or nonzero angles-of-attack are being considered, one must also include the effects of changes in the computed mean flow (e.g. zeroth harmonic) for different LCO amplitudes, which in turn effect the mean angle-of-attack $\bar{\alpha}_0$ of the LCO. This requires that one must also satisfy the static (e.g. zeroth harmonic) aeroelastic equation for the pitch degree-of-freedom

$$K_\alpha(\bar{\alpha}_0 - \alpha_{e_0}) = q_\infty c^2 s \bar{c}_{m_0}(\bar{\omega}, \bar{\alpha}_0, \bar{\alpha}_1, \bar{h}_1/b), \quad (3.5)$$

where α_{e_0} is the angle-of-attack for zero spring stiffness in the pitch coordinate. After some rearrangement, this equation can be written as

$$\bar{\alpha}_0 = \alpha_{e_0} + \frac{2V^2}{\pi r_\alpha^2} \bar{c}_{m_0}. \quad (3.6)$$

The static aeroelastic equation for the plunge coordinate \bar{h}_0 establishes the vertical position of the airfoil. This equation is decoupled from both the static pitch equation and the first harmonic unsteady aeroelastic equations (Eq. 3.2) and thus is neglected in the following theoretical development.

3.2.4 LCO Solution Procedure

In the following, we describe the technique in which the harmonic balance method can be used for modeling limit cycle oscillations. The methodology was initially developed and presented in Thomas et. al. [45]. The HB/LCO solution procedure starts by rewriting Eq. 3.2 as

$$\mathbf{Gv} = \frac{V^2}{\pi \bar{\alpha}_1} \mathbf{f}, \quad (3.7)$$

where

$$\mathbf{v} = \begin{Bmatrix} \bar{h}_1/\bar{\alpha}_1 b \\ 1 \end{Bmatrix}. \quad (3.8)$$

In this form, Eq. 3.2 has been divided through by the first harmonic unsteady pitch amplitude $\bar{\alpha}_1$. This enables one to consider $\bar{\alpha}_1$ as the independent variable in the HB/LCO solution process.

Defining $\mathbf{R}(\mathbf{L})$ as the vector operator representing residual of Eq. 3.6 together with the residual of the real and imaginary parts of Eq. 3.7, one may write the governing steady and unsteady aeroelastic equations in vector form as

$$\mathbf{R}(\mathbf{L}) = \left\{ \begin{array}{l} \bar{\alpha}_0 - \alpha_{e0} - \frac{2V^2}{\pi r_\alpha^2} \bar{c}_{m0} \\ \tilde{\mathbf{G}} \tilde{\mathbf{v}} - \frac{V^2}{\pi \bar{\alpha}_1} \tilde{\mathbf{f}} \end{array} \right\} = \mathbf{0}, \quad (3.9)$$

where $\tilde{\mathbf{G}}$ is the 4×4 matrix

$$\tilde{\mathbf{G}} = \begin{bmatrix} \mathbf{G}_{\text{Re}} & -\mathbf{G}_{\text{Im}} \\ \mathbf{G}_{\text{Im}} & \mathbf{G}_{\text{Re}} \end{bmatrix}, \quad (3.10)$$

$\tilde{\mathbf{v}}$ and $\tilde{\mathbf{f}}$ are

$$\tilde{\mathbf{v}} = \begin{Bmatrix} \text{Re}(\bar{h}_1/\bar{\alpha}_1 b) \\ 1 \\ \text{Im}(\bar{h}_1/\bar{\alpha}_1 b) \\ 0 \end{Bmatrix}, \quad \tilde{\mathbf{f}} = \begin{Bmatrix} -\text{Re}(\bar{c}_{l1}) \\ 2 \text{Re}(\bar{c}_{m1}) \\ -\text{Im}(\bar{c}_{l1}) \\ 2 \text{Im}(\bar{c}_{m1}) \end{Bmatrix}, \quad (3.11)$$

and \mathbf{L} is the vector of unknown LCO variables

$$\mathbf{L} = \begin{Bmatrix} \bar{\alpha}_0 \\ V \\ \bar{\omega} \\ \text{Re}(\bar{h}_1/\bar{\alpha}_1 b) \\ \text{Im}(\bar{h}_1/\bar{\alpha}_1 b) \end{Bmatrix}. \quad (3.12)$$

We have found that a Newton-Raphson nonlinear root finding technique is an efficient and stable method for quickly solving for a root \mathbf{L} of Eq. 3.9. That is, for a specified unsteady pitch amplitude $\bar{\alpha}_1$, one can implement an iterative process whereby the $(n + 1)^{\text{th}}$ update to the LCO solution \mathbf{L} is given by

$$\mathbf{L}^{n+1} = \mathbf{L}^n - \left[\frac{\partial \mathbf{R}(\mathbf{L}^n)}{\partial \mathbf{L}} \right]^{-1} \mathbf{R}(\mathbf{L}^n), \quad (3.13)$$

where

$$\left[\frac{\partial \mathbf{R}(\mathbf{L})}{\partial \mathbf{L}} \right] = \left[\begin{array}{ccccc} \frac{\partial \mathbf{R}}{\partial \bar{\alpha}_0} & \frac{\partial \mathbf{R}}{\partial V} & \frac{\partial \mathbf{R}}{\partial \bar{\omega}} & \frac{\partial \mathbf{R}}{\partial \text{Re}(\bar{h}_1/\bar{\alpha}_1 b)} & \frac{\partial \mathbf{R}}{\partial \text{Im}(\bar{h}_1/\bar{\alpha}_1 b)} \\ | & | & | & | & | \end{array} \right] \quad (3.14)$$

We have also found that one can get very good convergence by simply approximating the column vectors of $\partial \mathbf{R}(\mathbf{L}^n)/\partial \mathbf{L}$ using forward differencing. That is,

$$\frac{\partial \mathbf{R}(\mathbf{L}^n)}{\partial \bar{\alpha}_0} \approx \frac{\mathbf{R}(\mathbf{L}^n, \bar{\alpha}_0^n + \epsilon) - \mathbf{R}(\mathbf{L}^n, \bar{\alpha}_0^n)}{\epsilon}, \quad (3.15)$$

$$\frac{\partial \mathbf{R}(\mathbf{L}^n)}{\partial V} \approx \frac{\mathbf{R}(\mathbf{L}^n, V^n + \epsilon) - \mathbf{R}(\mathbf{L}^n, V^n)}{\epsilon}, \quad (3.16)$$

etc. for a small ϵ .

For each step of the LCO solution procedure, the harmonic balance flow solver is implemented using the current LCO frequency $\bar{\omega}$ and structural mode shape $(\bar{h}_1/\bar{\alpha}_1 b)$, for the prescribed LCO pitch amplitude $\bar{\alpha}_1$, to provide an update for the LCO aerodynamic loading (i.e. \bar{c}_l , \bar{c}_{m_0} , and \bar{c}_{m_1}). The technique is marched until a suitable level of convergence is achieved, and the linear flutter solution has been found to provide an excellent starting solution for the iterative process. Typically, only a few iterations are required to achieve convergence.

3.3 Steady and Unsteady Aerodynamic Modeling of the NLR 7301 Airfoil

The model configuration under consideration is the NLR 7301 constant airfoil section wing tested extensively by Schewe et. al. [46, 47] and Knipfer and Schewe [48]. Transonic two-degree of freedom aeroelastic experimental studies were conducted for various Mach numbers and angles-of-attack, and in some instances, LCO was observed.

The experimental condition we model using the HB/LCO solution methodology is referred to by Schewe et. al. [47] as "measured point" condition MP77. This is an LCO condition where the wind-tunnel test section Mach number, mean angle-of-attack, and Reynolds number are reported to be [48, 47] $M_\infty = 0.768$, $\bar{\alpha}_0 = 1.28$ degree, and $Re_\infty = 1.727 \times 10^6$, respectively. The experimental model [46, 48, 47] consists of a one meter span ($s = 1.0m$) by 0.3 meter chord ($c = 0.3m$) NLR 7301 constant airfoil section wing placed in a one meter by one meter cross section wind tunnel test section. The elastic axis of the model is positioned at the wing quarter chord. Due to the relatively large size of the model in relation to the wind tunnel cross section, wind tunnel interference effects are known to be significant.

The harmonic balance based CFD flow solver used in the present investigation is capable of only modeling isolated airfoil sections in an unbounded freestream. As such, a method of accounting for wind-tunnel wall interference effects is necessary. Unfortunately, simple classical analytical wind-tunnel wall interference correction methods have the tendency to breakdown for transonic Mach numbers. As such, one method to account for wind-tunnel wall interference effects is to seek out a combination of Mach number and angle-of-attack for the CFD method such that the computed surface pressure distribution matches as best as possible the experimental distribution. Investigators such as Weber et. al. [54] and Tang et. al. [55], who are also studying computational techniques for modeling test condition MP77, have reported recently however that such a combination of corrected Mach number and angle-of-attack has been quite elusive to determine, and appears perhaps not to exist. In fact, Castro et. al. [?, 57] have recently taken the approach of adding appropriate boundary conditions to their CFD flow solver to account for the wind-tunnel walls. However, Castro et. al. have noted that there is still much difficulty in correctly accounting for wind-tunnel wall porosity effects.

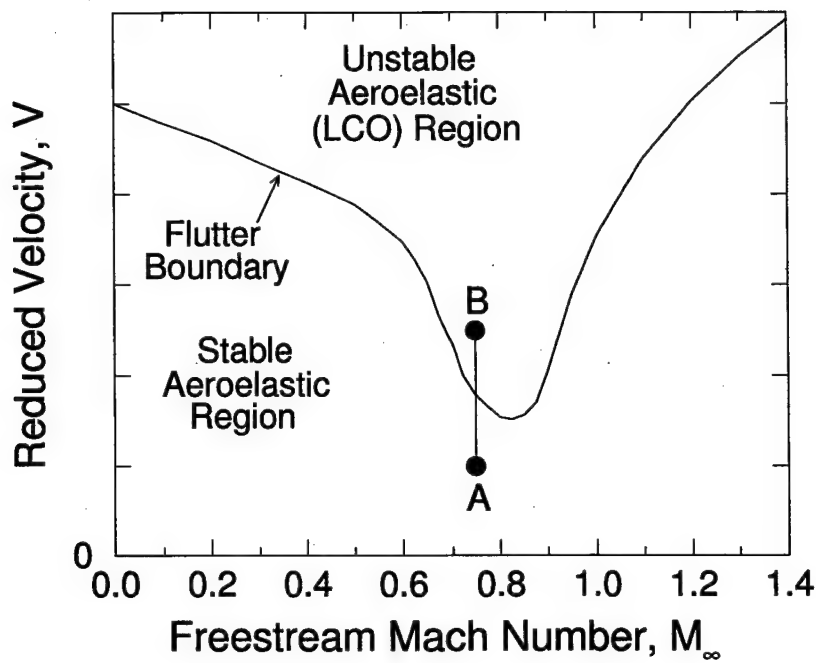
Rather than go through a similar and time consuming exercise of trying to determine a combination of corrected Mach number and angle-of-attack in an effort to precisely match the experimental surface pressure distribution, we have decided as a first approximation to proceed by fixing the Mach number to $M_\infty = 0.75$, and to then simply adjust the angle-of-attack until the computed CFD solution steady flow lift matches the experimental lift.

3.3.1 Computational Mesh

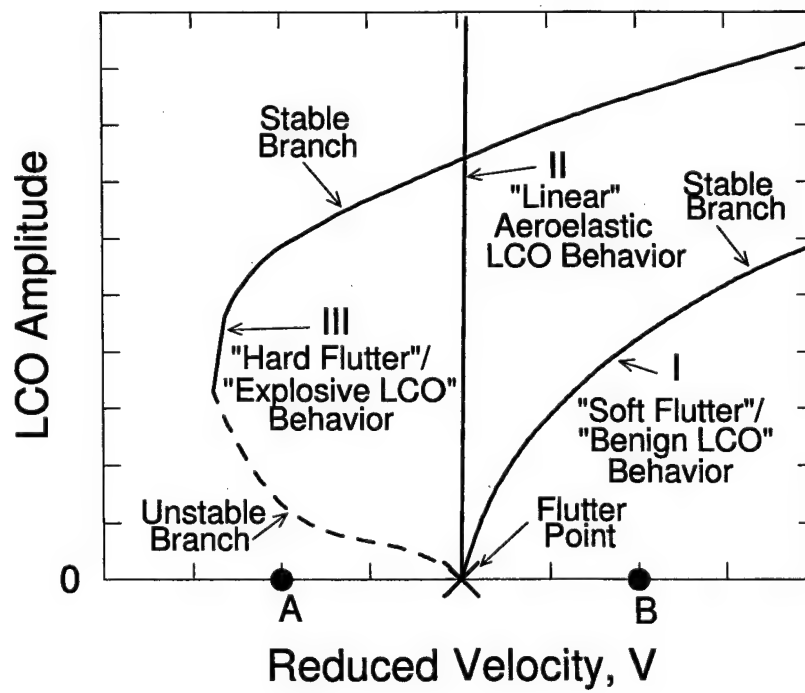
Figure 3.3 shows sample inviscid and viscous computational grids used by the HB CFD solver for the NLR 7301 airfoil configuration. A "C-grid" structured mesh topology is used. The "fine" mesh viscous grid shown in Fig. 3.3c and Fig. 3.3d consists of 65 mesh points radially and 257 mesh points circumferentially, with a total of 193 mesh points surrounding the airfoil surface, and the remainder of the circumferential mesh points being distributed in the wake. For all grids, the outer boundary extends to a distance of 10 chord lengths from the center of the airfoil. Similar 129×33 and 193×49 meshes have also been created. Figure 3.3a and Fig. 3.3b show an inviscid 193×49 mesh.

For viscous simulations, the grid spacing has been placed close enough to the airfoil surface such that the maximum computed value for the nondimensional distance to the wall spacing parameter y^+ is everywhere less than 2.0 for the three mesh resolutions considered.

3.3.2 Steady Flow Simulations



(a) Mach Number Flutter Speed Dip Trend



(b) LCO Behavior Trends Near Flutter Onset Condition

Figure 3.1: Example LCO Behavior Trends.

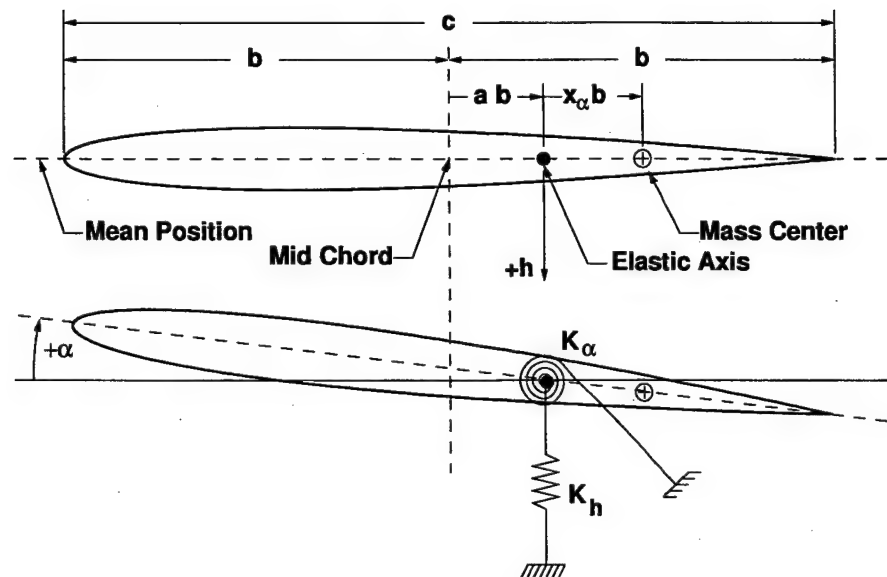
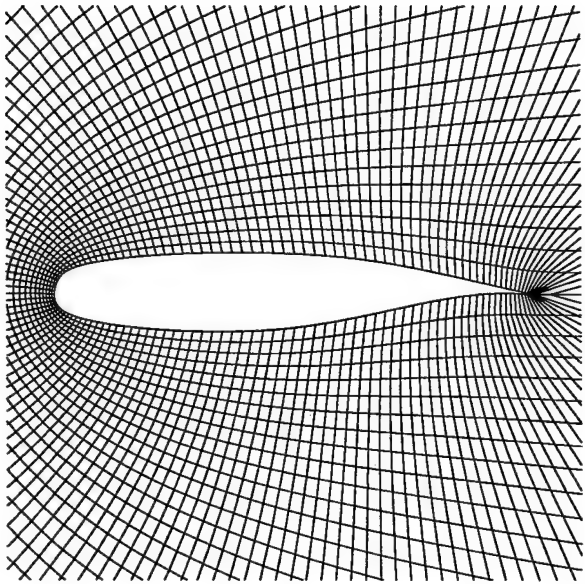
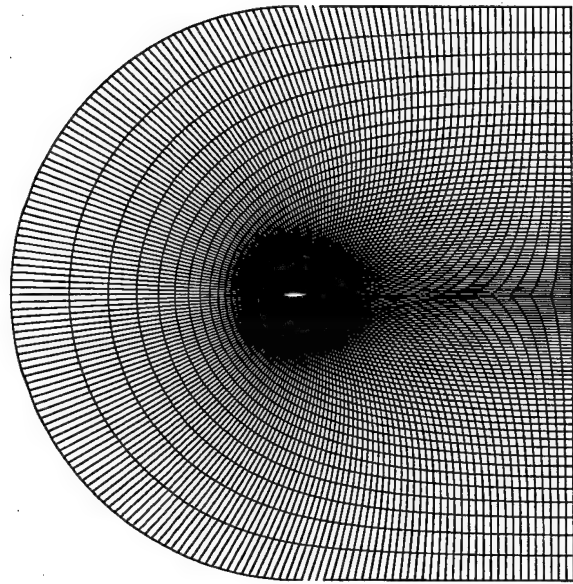


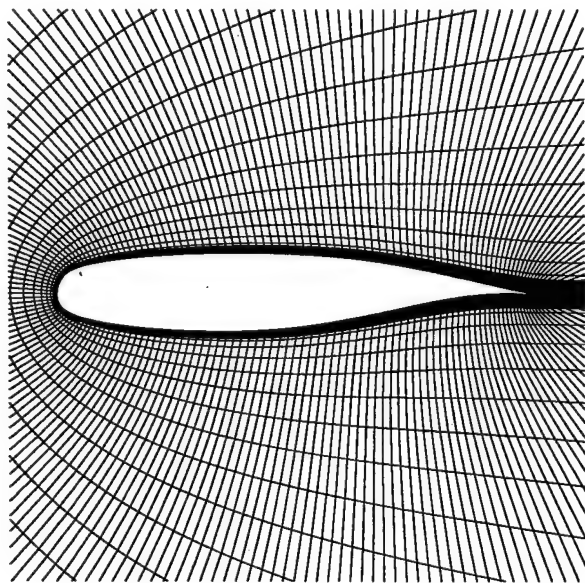
Figure 3.2: Geometry for "Typical" (Pitch/Plunge) Two-Degree-of-Freedom Airfoil Section Aeroelastic Model.



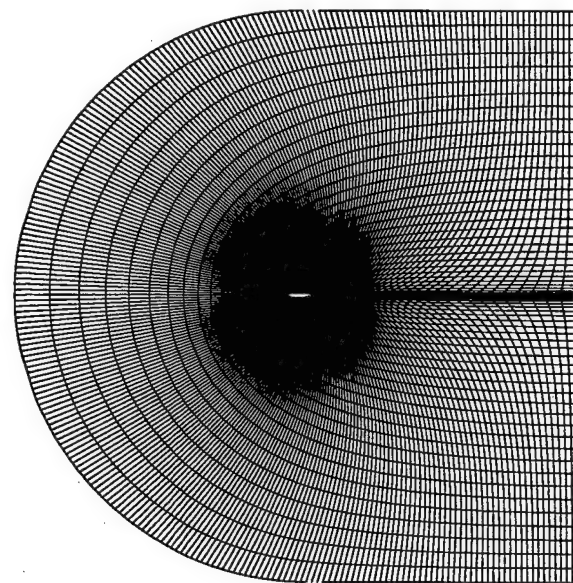
(a) Inviscid Mesh Close-Up



(b) Inviscid Mesh Overall



(c) Viscous Mesh Close-Up



(d) Viscous Mesh Overall

Figure 3.3: Computational Grids Used for the NLR 7301 Airfoil Configuration.

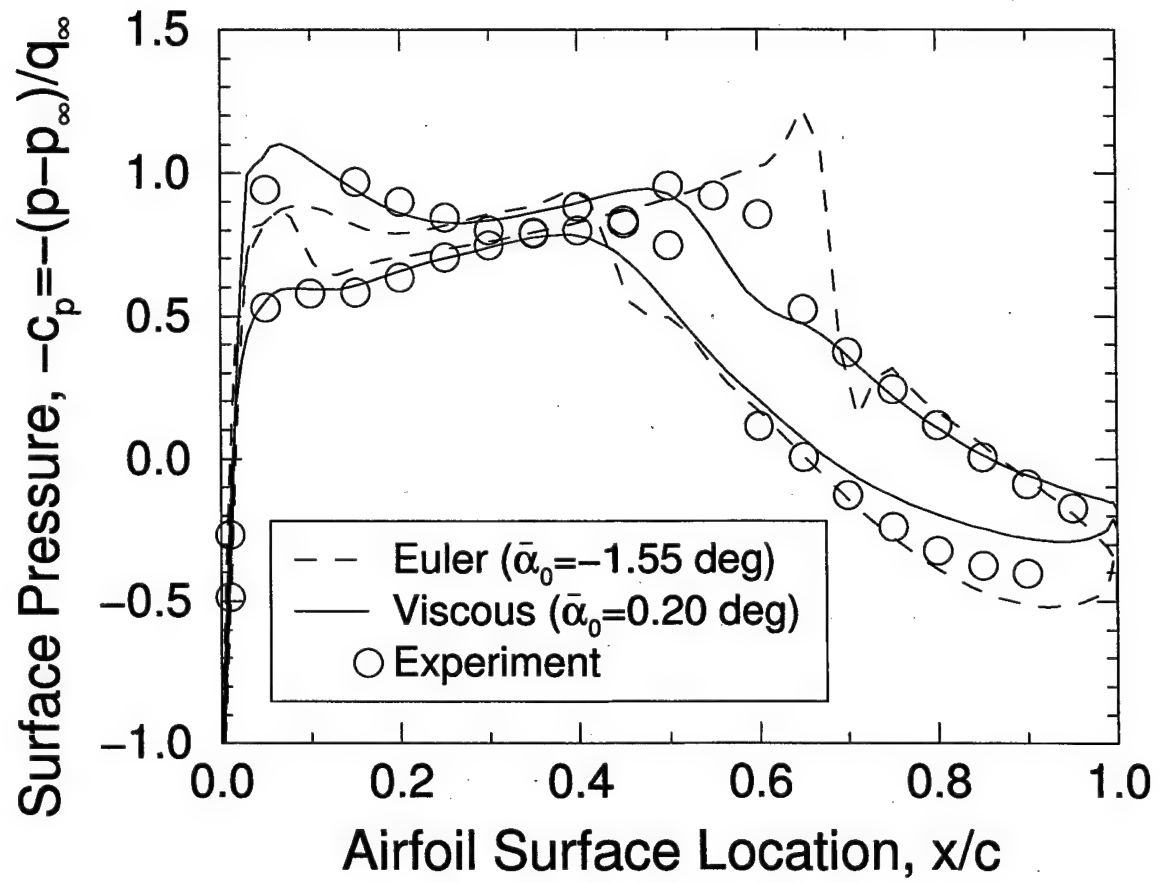
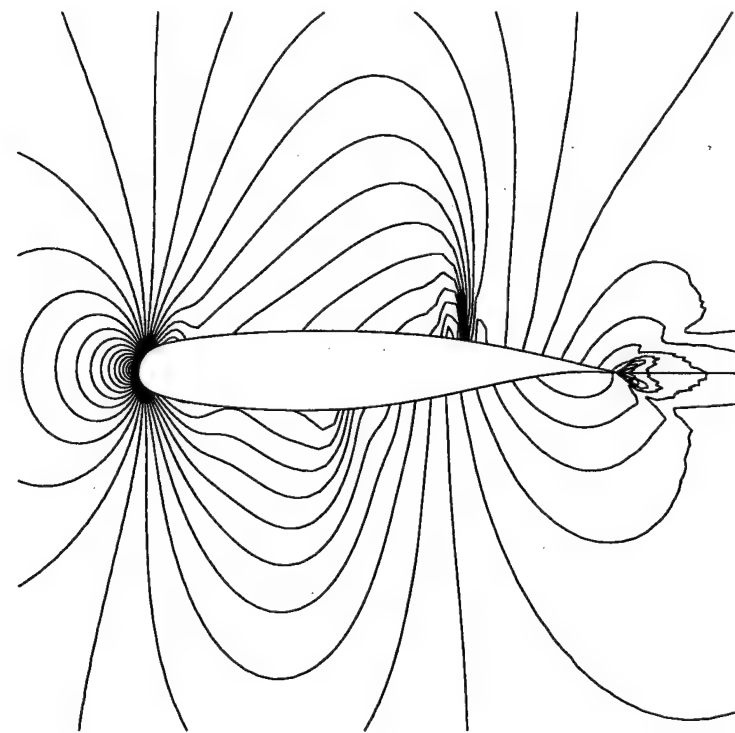
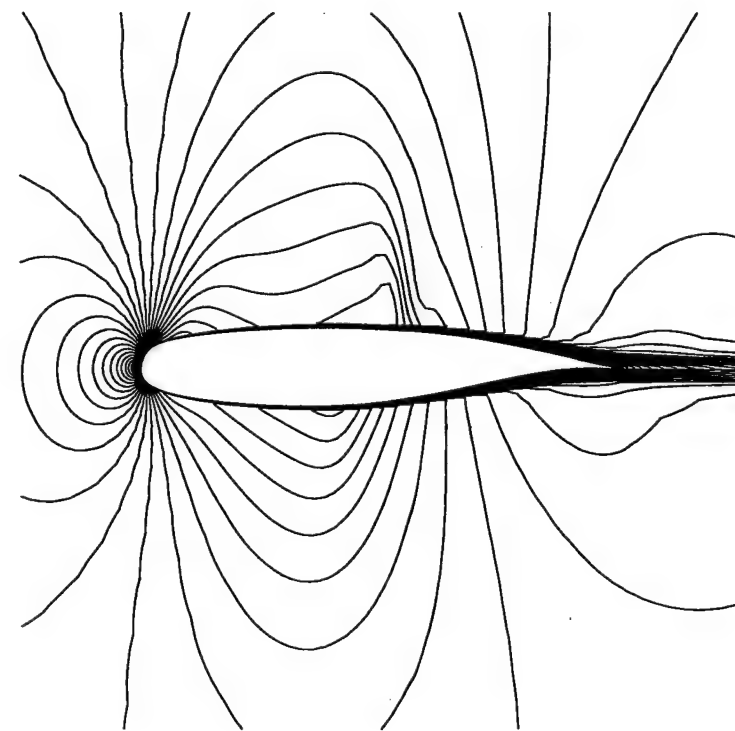


Figure 3.4: Computed Steady Flow Surface Pressure Distributions: NLR 7301 Airfoil Section, $M_\infty = 0.75$, $Re_\infty = 1.727 \times 10^6$.



(a) Inviscid



(b) Viscous

Figure 3.5: Computed Steady Flow Mach Number Contours: NLR 7301 Airfoil Section, $M_\infty = 0.75$, $Re_\infty = 1.727 \times 10^6$. 46

Mesh Size	Number of Harmonics		
	1	2	3
129 × 33	(-0.18,-0.40)	(-0.31,-0.29)	(-0.27,-0.26)
193 × 49	(-0.11,-0.54)	(-0.34,-0.44)	(-0.28,-0.39)
257 × 65	(-0.08,-0.60)	(-0.32,-0.52)	(-0.28,-0.47)

Table 3.1: Mesh Resolution and Number of Harmonic Used in Harmonic Balance Solver Trends for Computed First Harmonic Unsteady Moment Coefficient $\bar{c}_{m_1}/\bar{\alpha}_1$: $M_\infty = 0.75$, $Re_\infty = 1.727 \times 10^6$, $\bar{\alpha}_0 = 0.2$ (deg), $\bar{\alpha}_1 = 5.$ (deg), $\bar{\omega} = 0.3$, and $a = -0.5$.

With the Mach number set to $M_\infty = 0.75$, steady flows are computed by simply running the HB flow solver with zero harmonics. In order to match the experimentally observed lift coefficient of $\bar{c}_l = 0.27$, an angle-of-attack of $\bar{\alpha}_0 = 0.2$ degree is needed for the viscous flow model, while an angle-of-attack of $\bar{\alpha}_0 = -1.55$ degree is required for the inviscid model.

For both the inviscid and viscous flow models, Fig. 3.4 shows the computed and experimental steady surface pressure distributions, while Fig. 3.5 shows computed steady Mach contours. In this instance, a 257×65 grid has been used for the viscous model, and a 193×49 grid has been used for the inviscid model. A strong shock is readily apparent for the inviscid model.

3.3.3 Unsteady Flow Simulations

Next, Fig. 3.6 shows computed Mach contours during one cycle of motion for the fine mesh (257×65) viscous flow CFD model of the NLR 7301 airfoil when oscillating about the quarter-chord at a pitch amplitude of $\bar{\alpha}_1 = 5.$ degrees and a reduced frequency $\bar{\omega} = 0.3$. Clearly evident is shock induced boundary layer separation over both the upper and lower surfaces during a cycle of motion.

3.3.4 Mesh and Harmonic Convergence Issues

To have confidence in the LCO solutions, one needs to determine whether or not a sufficient level of grid resolution is being used to model the correct flow physics accurately. For the harmonic balance solver, the issue of solution resolution is further complicated by the fact that one must also consider harmonic convergence. That is, whether or not a sufficient number of harmonic expansion terms N_H are being used in the HB flow solver.

Thus, much like when working with time domain methods where one must also be concerned with temporal accuracy in addition to spatial accuracy, for the HB method, both mesh and harmonic resolution must be considered. To help give a sense if sufficient mesh resolution and harmonics are being utilized, one can define a "most difficult" test case. For example, consider a configuration that is moving at the largest amplitude that one wishes to model, and also near the reduced frequency that is of interest, say the flutter reduced

Dimensional Quantities	
m	4.65 kg
m_{SD}	8.24 kg
m_{SP}	13.75 kg
I_α	0.086 kg m^2
K_h	$1.21 \times 10^6 \text{ N/m}$
K_α	$6.68 \times 10^3 \text{ N m/rad}$
S_α	0.387 kg m
D_h	82.9 kg/sec
D_α	$0.197 \text{ kg m}^2/(\text{sec rad})$
ρ_∞	0.383 kg/m^3
Nondimensional Quantities	
μ	172
x_α	0.555
r_α^2	0.822
ω_h/ω_α	1.83
ζ_h	0.0175
ζ_α	0.00411

Table 3.2: Structural Parameter Values for the NLR 7301 Aeroelastic Configuration.

frequency. One can then create a table of computed unsteady aerodynamic lift or moment values for different mesh resolutions and numbers of harmonics (N_H) used in the HB flow solver.

Table 3.1 in fact shows a total of nine individually computed values for unsteady moment for the three different mesh resolutions (129×33 , 193×49 , 257×65) and either one, two, or three harmonics (N_H) used in the HB algorithm. An unsteady pitch amplitude of $\bar{\alpha}_1 = 5$. degrees is chosen, which is the maximum amplitude we consider in the LCO analysis to follow, along with a reduced frequency of $\bar{\omega}=0.3$. As can be seen, the unsteady solution for this "most difficult" test case appears to be rapidly converging. Therefore, for the LCO studies presented in the following, results are based on the 193×49 mesh using two harmonics ($N_H = 2$) in the HB flow solver.

3.4 Limit Cycle Oscillation Modeling for the NLR 7301 Configuration

3.4.1 Structural Parameters

The structural parameters used for the LCO analysis are those presented in Knipfer and Schewe [48] and Schewe et. al. [47]. Table 3.2 summarizes values for dimensional and nondimensional quantities.

3.4.2 Flutter Point Prediction

Computing the LCO behavior via the HB/LCO solution methodology proceeds by first determining the flutter onset condition. As noted before, experimental measured point condition MP77 corresponds to an LCO condition. However, the observed LCO amplitude is very small. Approximately $|\bar{\alpha}_1| = 0.18$ degree (Fig. 15 of Knipfer and Schewe [48]). As will be shown subsequently, based on the predicted LCO behavior using the HB/LCO method, for such a small amplitude, the flow conditions at measured point MP77 are likely to be very near the flutter onset condition. For this analysis, we are considering this to be the case. As such, we are in effect assuming that the lift coefficient at the flutter onset condition is also $\bar{c}_{l_0 f} = 0.27$.

Rather than use a separate linearized unsteady aerodynamic solver to determine the flutter onset condition, one can instead simply run the HB CFD flow solver with a single harmonic ($N_H = 1$) and consider a very small amplitude motion. As the amplitude of motion goes to zero, the HB solver yields exactly the same answer as a linearized unsteady solver. This is another useful feature of the HB solver.

Predicting the linear flutter point condition thus consists of first tabulating linear unsteady aerodynamic loading data for plunge and pitch motions, respectively, for discrete reduced frequencies $\bar{\omega}$ over a range of reduced frequencies where flutter is presumed to occur. In this instance, we have chosen small unsteady motion amplitudes of $\bar{h}_1/b = 0.001$ and $\bar{\alpha}_1 = 0.001$ degree, respectively for the plunge and pitch degrees-of-freedom, in order to simulate dynamically linear unsteady aerodynamics. Normalizing the calculated unsteady lift and moment coefficients by the respective amplitudes of either the plunge or the pitching motions, one then can obtain tabulated data for the unsteady aerodynamic transfer functions $\bar{c}_{l_1 \bar{h}_1/b}(\bar{\omega})$, $\bar{c}_{l_1 \bar{\alpha}_1}(\bar{\omega})$, $\bar{c}_{m_1 \bar{h}_1/b}(\bar{\omega})$, and $\bar{c}_{m_1 \bar{\alpha}_1}(\bar{\omega})$ at the preselected reduced frequencies $\bar{\omega}$. The 2×2 linear unsteady aerodynamic transfer function matrix $\mathbf{F}(\bar{\omega})$ is

$$\mathbf{F} = \begin{bmatrix} \bar{c}_{l_1 \bar{h}_1/b}(\bar{\omega}) & \bar{c}_{l_1 \bar{\alpha}_1}(\bar{\omega}) \\ \bar{c}_{m_1 \bar{h}_1/b}(\bar{\omega}) & \bar{c}_{m_1 \bar{\alpha}_1}(\bar{\omega}) \end{bmatrix}, \quad (3.17)$$

and for dynamically linear unsteady aerodynamics,

$$\mathbf{f} = \mathbf{F} \mathbf{u}. \quad (3.18)$$

With the linear unsteady aerodynamic transfer functions tabulated for a range of real reduced frequencies, one can then use a "V-g" or similar type of method to solve for the flutter onset conditions. For example, by rewriting Eq. 3.2 as

$$\left(\mathbf{G} - \frac{V^2}{\pi} \mathbf{F} \right) \mathbf{u} = \mathbf{H}(V, \bar{\omega}) \mathbf{u} = \mathbf{0}, \quad (3.19)$$

one can search the plane of values for reduced velocity and reduced frequency, $(V, \bar{\omega})$, for the

Variable	Inviscid	Viscous	Experiment
$\bar{\alpha}_0$ (deg)	-1.55	0.20	
\bar{c}_{l_0}	0.267	0.272	0.27
\bar{c}_{m_0}	-0.140	-0.0646	-0.082
V	0.371	0.385	0.488
$\bar{\omega}$	0.312	0.301	0.242
$\bar{\alpha}_1$ (deg)	0.0001	0.0001	0.18
$(\bar{h}_1/\bar{\alpha}_1 b)$	(1.15,0.141)	(1.12,0.172)	(1.66,0.)

Table 3.3: Computed Flutter Point Conditions and NLR 7301 Aeroelastic Configuration Experimental Test Case MP77 LCO Conditions.

condition(s) where the magnitude of the determinant of the 2×2 matrix \mathbf{H} is a minimum. Using this technique provides a quick and easy way of determining a good approximation of the flutter onset condition(s). This approximate flutter solution then provides a good starting solution for the HB/LCO method, which when then run for a very small amplitude motion, can be used to seek out the precise flutter onset condition. This is what has been done for the current flutter analysis of the NLR 7301 configuration, and the results for the precise flutter onset conditions for the viscous and inviscid flow models are shown in Table 3.3, which also presents data for the LCO condition of experimental test point MP77.

As can be seen from Table 3.3, the computed flutter onset conditions are somewhat different than those observed for the MP77 test case. The numerical model predicts a lower flutter reduced velocity, and a higher flutter reduced frequency, respectively for both the inviscid and viscous flow models. The MP77 experimental result for the structural eigenvector is also somewhat more plunge dominated than the computed values. Figure 15 of Knipfer and Schewe [48] was used to determine the value of $(\bar{h}_1/\bar{\alpha}_1 b)$ for the MP77 experimental condition. Note, Knipfer and Schewe [48] define the plunge coordinate h positive upward, opposite to our definition. We have corrected for this sign difference for the experimental value listed in Table 3.3.

We are currently trying to ascertain what possible causes might explain the differences between the experimental and computed conditions. Perhaps the steady flow CFD solution based on adjusting the angle-of-attack to match the experimental lift coefficient does not provide a sufficient approximation of the true wind-tunnel aerodynamic environment, or perhaps the MP77 test case corresponds to a flow condition more removed from the flutter onset condition.

We wish to also point out that we define mass ratio μ based on the wing model mass m , whereas Schewe et. al. [46, 47] and Knipfer and Schewe [48] define the mass ratio based on the total plunge coordinate mass m_h . This in turn means that the reduced velocity is also defined somewhat differently. One may relate the two definitions for reduced velocity via $\sqrt{(m_h/m)}$. That is, our definition for reduced velocity is the product of the Schewe et.

al. [46, 47] and Knipfer and Schewe [48] definition multiplied by $\sqrt{(m_h/m)}$.

3.4.3 Zero Spring Stiffness Angle-of-Attack

Next, the angle-of-attack corresponding to zero torsional spring stiffness, α_{e0} , is computed for both the viscous and inviscid models. Once the flutter point is established, this value is easily determined using Eq. 3.6. For the inviscid flow model, the value is $\alpha_{e0} = -0.692$ (deg), and for the viscous flow model, the value is $\alpha_{e0} = 0.645$ (deg).

3.4.4 Computed LCO Behavior

With the flutter onset condition established, along with a computed value for the angle-of-attack for zero torsional spring stiffness α_{e0} , one can proceed with the LCO analysis for finite amplitude motions. Figure 3.7 shows computed LCO solution behavior trends for both the viscous and inviscid models of the NLR 7301 configuration. Also shown in Figure 3.7 are the experimental LCO conditions as reported by Schewe et. al. [46, 47] along with computed LCO conditions as determined by the investigations of Weber et. al. [54] and Tang et. al. [55].

Clearly from the LCO amplitude versus reduced velocity curves shown in Fig. 3.7a, modeling viscous flow effects leads to a nonlinear soft or benign LCO behavior trend as discussed in the introduction, whereas the inviscid model exhibits a nearly linear aeroelastic LCO behavior trend. The flutter onset condition is also indicated in the figures and is less sensitive to viscous effects. Fig. 3.7b and Fig. 3.7c show, respectively, LCO behavior trends for the frequency ratio and reduced frequency. The reduced frequency can be seen to change by a significant amount in the viscous case for large amplitudes. Finally, Fig. 3.7d shows the change in the LCO mean angle-of-attack $\bar{\alpha}_0$ with respect to reduced velocity. The LCO mean angle-of-attack is observed to decrease by approximately 0.5 degree from the flutter onset condition for the range of LCO amplitudes considered in the case of the viscous model. Since the aerodynamics are known to be extremely sensitive to small changes in the transonic region, it is likely to be important to model this effect.

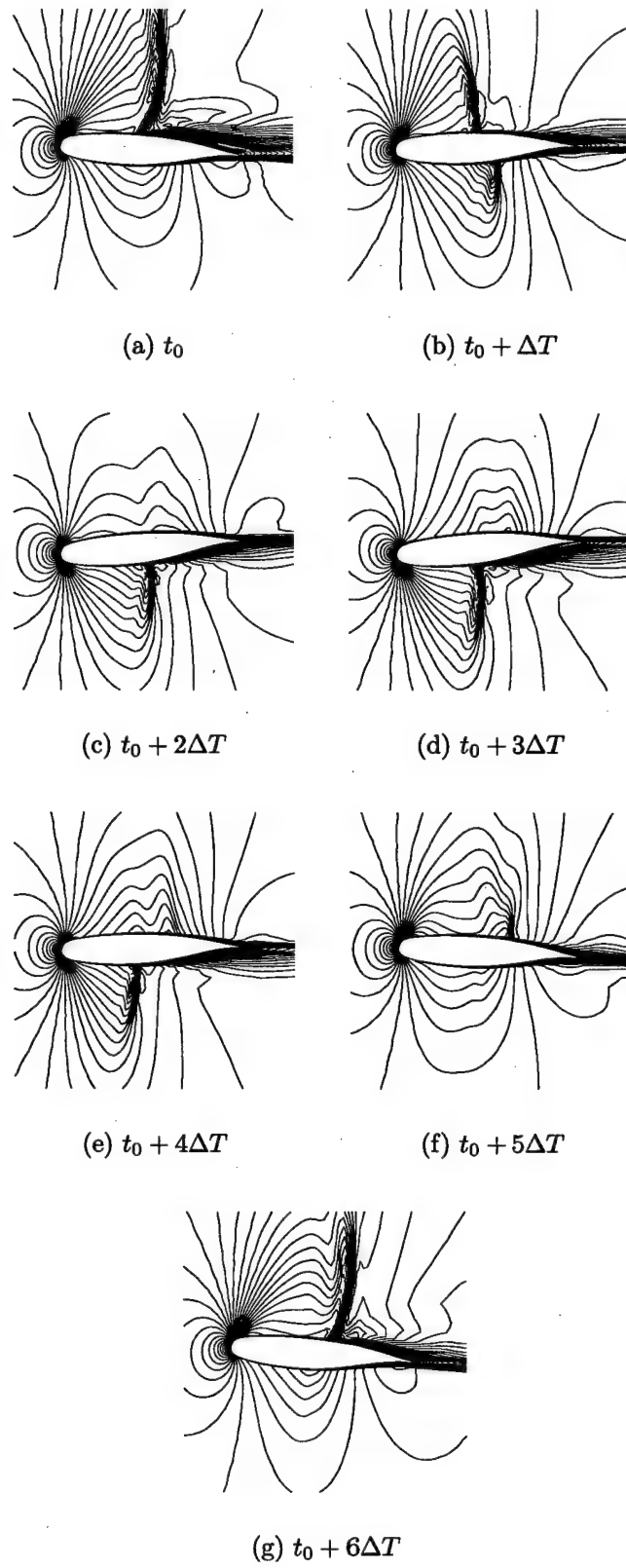
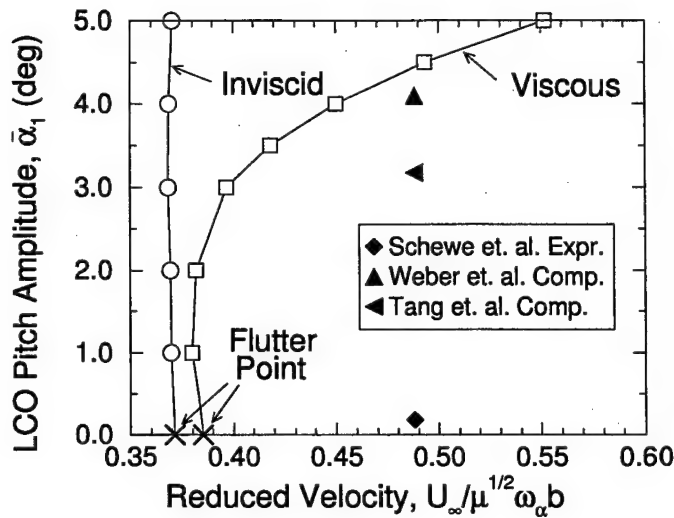
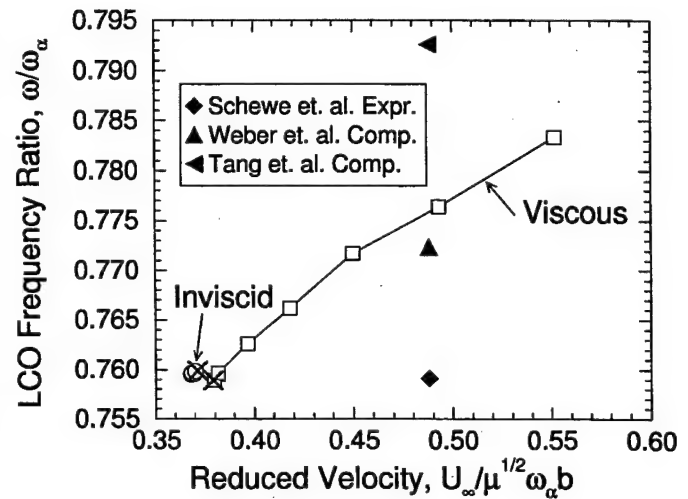


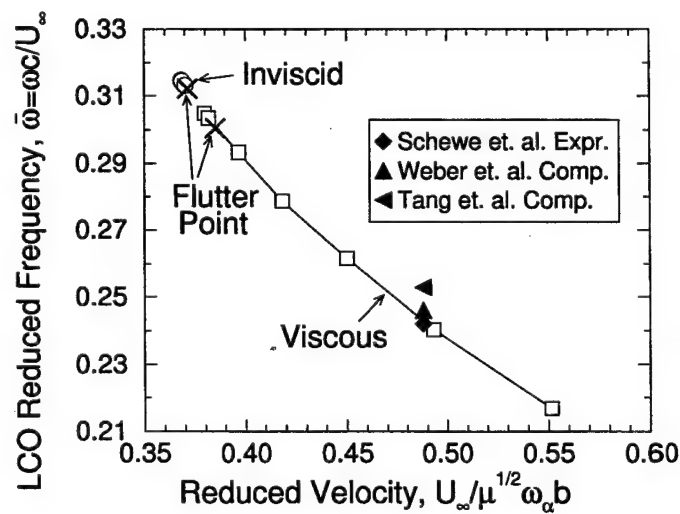
Figure 3.6: Computed HB Method Unsteady Mach Number Contours: NLR 7301 Airfoil Section, $M_\infty = 0.75$, $Re_\infty = 1.727 \times 10^6$, $\bar{\alpha}_0 = 0.2$ (deg), $\bar{\alpha}_1 = 5.$ (deg), $\bar{\omega} = 0.3$, $a = -0.5$, $N_H = 3$ ($\Delta T = T/(2N_H + 1)^{5/2} = T/7$).



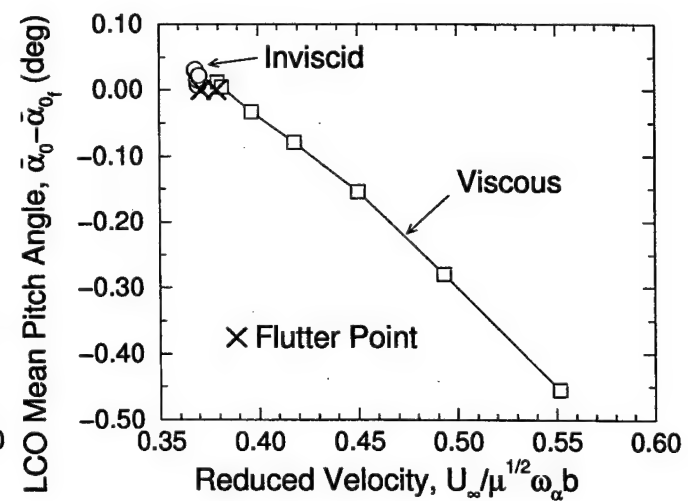
(a) LCO Amplitude



(b) LCO Frequency Ratio



(c) LCO Reduced Frequency



(d) LCO Mean Pitch Angle

Figure 3.7: LCO Behavior Trends for the NLR 7301 Configuration

3.5 Conclusions

An efficient procedure for computing the LCO behavior of aeroelastic airfoil configurations in viscous transonic flows is presented. Viscous effects are demonstrated to be an important factor in determining the behavior of LCO response with respect to reduced velocity. Viscous effects for the NLR 7301 aeroelastic configuration under investigation lead to a much more gradual rate of increase in LCO amplitude with respect to reduced velocity when compared to an inviscid model. The rapid increase in the computed LCO response beyond the flutter point emphasizes the importance of making careful and comprehensive experimental measurements of LCO response over a range of reduced velocities or other parameters as the flutter boundary is exceeded.

Nomenclature

a	= nondimensional location of airfoil elastic axis, $a = e/b$ (see Fig. 3.2)
b, c	= semi-chord and chord, respectively
c_l, c_m	= coefficient of lift and moment about elastic axis, respectively
$\bar{c}_{l_0}, \bar{c}_{m_0}$	= zeroth harmonic or mean coefficient of lift and moment about elastic axis, respectively
$\bar{c}_{l_1}, \bar{c}_{m_1}$	= first harmonic unsteady coefficient of lift and moment about elastic axis, respectively
D_h, D_α	= airfoil plunge damping and torsional damping, respectively
e	= location of airfoil elastic axis, measured positive aft of airfoil midchord
h, α	= airfoil plunge and pitch coordinate degree of freedom, respectively
$\bar{h}_0, \bar{\alpha}_0$	= zeroth harmonic or mean airfoil plunge and pitch amplitude, respectively
$\bar{h}_1, \bar{\alpha}_1$	= first harmonic unsteady airfoil plunge and pitch amplitude, respectively
I_α	= second moment of inertia of airfoil about elastic axis
j	$= \sqrt{-1}$
K_h, K_α	= airfoil plunge stiffness and torsional stiffness about elastic axis, respectively
M_∞	= freestream Mach number
m	= wind-tunnel experimental wing mass

m_{SD}	= wind-tunnel shift device mass
m_{SP}	= wind-tunnel suspension device mass
m_h	= wind-tunnel plunge coordinate total mass, $m_h = m + m_{SD} + m_{SP}$
μ	= mass ratio, $\mu = m/\pi\rho_\infty b^2 s$
ν	= kinematic viscosity
N_H	= number of harmonics used in harmonic balance CFD flow solver method
Re_∞	= freestream Reynolds number
r_α	= radius of gyration of airfoil about elastic axis, $r_\alpha^2 = I_\alpha/m b^2$
ρ, ρ_∞	= local and freestream density, respectively
S_α	= first moment of inertia of airfoil about elastic axis
s	= wind-tunnel experimental model span
T	= period, time for one cycle of oscillation
τ_w	= airfoil surface tangential shear stress
T	= period, time for one cycle of oscillation
U_∞	= freestream velocity
V	= reduced velocity, $V = U_\infty/\sqrt{\mu\omega_\alpha b}$
$\omega, \bar{\omega}$	= frequency and reduced frequency based on airfoil chord $\bar{\omega} = \omega c/U_\infty$, respectively
ω_h	= plunge coordinate natural frequency based on wing mass, $\omega_h = \sqrt{K_h/m}$
ω_α	= pitch coordinate natural frequency, $\omega_\alpha = \sqrt{K_\alpha/I_\alpha}$
x_α	= airfoil static unbalance, $x_\alpha = S_\alpha/m b$
y	= dimensional distance normal to the airfoil surface
y^+	= nondimensional distance normal to the airfoil surface, $y^+ = y\sqrt{\tau_w/\rho}/\nu$
ζ_h	= plunge coordinate damping coefficient, $\zeta_h = D_h/2m\omega_h$
ζ_α	= pitch coordinate damping coefficient, $\zeta_\alpha = D_\alpha/2I_\alpha\omega_\alpha$

Subscripts/Superscript

f = flutter point condition

Re, Im = real and imaginary part, respectively

Chapter 4

ZONA 2-DOF Airfoil LCO: CFL3D.AE

Summary

- Several efforts were directed toward the validation of the measured LCO/flutter data of DLR and the verification of the results due to Duke University using the frequency-domain POD/ROM eigenmode approach. In Phase II, the work in this chapter using a time-marching CFD method in two dimensions for the simulation of the transonic LCO/flutter of a supercritical airfoil (NLR 7301) are presented in three parts
 1. Fundamentals and preliminary formulations and result comparison with DLR's measured data which is presented in this chapter.
 2. Further refinement of (1) in various details, which is published in the *Journal of Fluid and Structures* (17 (2003)29-41).
 3. Extension of parts (1) and (2) in the investigation on the impact of initial condition on the transonic LCO to the same NLR airfoil, which is presented in Appendix A.

The work in this part is necessary, as such impact on LCO by initial conditions could not be so investigated by the frequency-domain approach of Duke using harmonic balance (HB) technique. (This work is presented in *Symposium Transsonicum IV* held in Göttingen, Germany, Sept. 2002 and is published as *Symposium Transsonicum IV* by Kluwer Academic Publishers Nov. 2003 (ISBN1-4020-1608-5))

- CFD-based aeroelastic computation is performed to investigate the effect of nonlinear aerodynamics on transonic LCO (Limit Cycle Oscillations) characteristics of a two-dimensional supercritical wing with the NLR 7301 section. It is found that LCO amplitude given by Navier-Stokes computation is less than 1/3 of the one given by Euler computation, much closer to the experimental data. But Navier-Stokes computation of LCO is turbulence model dependent. Baldwin-Lomax model with Degani-Schiff modification seems to produce spurious vorticity for moving grids. Contrary to common sense, a larger amplitude initial perturbation produces an smaller amplitude LCO for

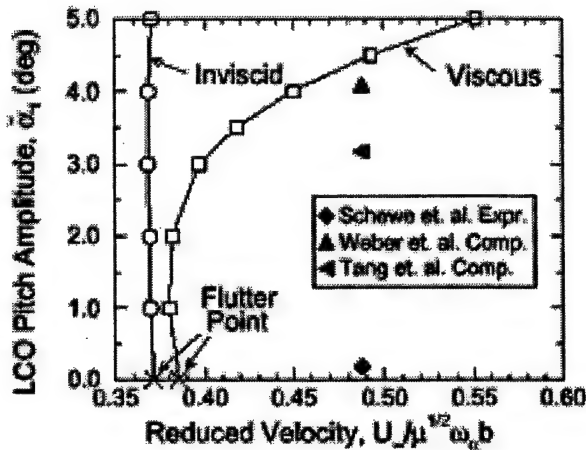


Figure 4.1: Transonic LCO Solutions and DLR Test Data for the NLR7301 Supercritical Airfoil at $M=0.75$.

the present case. The mean positions may change with the amplitude of the initial perturbation. Also addressed in the paper are certain aspects of multiblock MPI (Message Passing Interface) parallel computation related to the present problem. Taken from the abstract of the paper entitled "Numerical Investigation of Transonic Limit Cycle Oscillations of a Two Dimensional Supercritical Wing." (above part (2))

- A CFD time-marching method, CFL3D v6, is employed to investigate the influences of viscosity, initial airfoil position, and initial perturbation on the amplitudes of the transonic limit cycle oscillations (LCO) of a supercritical airfoil. As expected, stronger aerodynamic nonlinearity leads to smaller LCO amplitudes, even a damped solution while weaker aerodynamic nonlinearity incurs larger LCO amplitudes, even a divergent solution. Taken from the abstract of the paper entitled, "Nonlinear Aerodynamic Effects on Transonic LCO Amplitude of a Supercritical Airfoil." (above part (3))
- The computed results due to different methods on the transonic LCO solution for NLR7301 supercritical airfoil at $M = 0.75$ can be summarized by the following figure prepared by Duke University. It is seen that the DLR measured LCO amplitude (Schewe) is only a fraction of the computed results including that of ZONA (Tang et al), Naval Postgraduate School (Weber et al) and Duke University (Hall and Dowell, Hollow Symbols).

4.1 Introduction

LCO has been a persistent problem on several current fighter aircraft and is generally encountered with external store configurations. Denegri (2000) provided a detailed description of the aircraft/store LCO phenomenon. Norton (1990) gave an excellent overview of LCO

of fighter aircraft carrying external stores and its sensitivity to store carriage configuration and mass properties.

LCO can be characterized as sustained periodic oscillations which neither increase nor decrease in amplitude over time for a given flight condition. Using an s-domain unsteady aerodynamic model of the aircraft and stores, Chen et al. (1998) have shown that wing/store LCO can be a post-flutter phenomenon whenever the flutter mode contains low unstable damping. This type of flutter mode is called a "hump mode". Since the aircraft structure usually contains structural nonlinearity such as friction damping, this amplitude-dependent friction damping can suppress the growth of amplitude, thus resulting in a steady state oscillation. This is known as the nonlinear structural damping (NSD) model of the wing/store LCO. Although not thoroughly proven through tests or numerical simulations, results of the NSD show excellent correlation with flight test LCO data of F-16 throughout subsonic and transonic Mach numbers. On the other hand, other researchers, notably Cunningham and Meijer (1995), believe that the wing/store LCO is due largely to the transonic shock oscillation and shock induced flow separation, called Transonic Shock/Separation (TSS) model. Edwards has suggested the TSS model and viscous effects are two major factors that cause transonic LCO for wings. He also has studied the shock buffet phenomenon in addition to transonic LCO [65]. It should be noted that, however, there is no conflict in the NSD model and the TSS model in that both physical effects may contribute to the various instances of LCO.

Recent renewed interest in LCO is perhaps motivated by the need to further understand the physics of LCO and the current advent of CFD methodology in aeroelasticity. Among the potential computational methods for LCO prediction/investigation, two will be mentioned here: the CFL3D code (version 6) [59], [69, 72], developed and supported by NASA/Langley and the POD/ROM EigenMode approach [67], originated by Dowell and Hall of Duke University. The former is a conventional time-domain CFD method whereas the latter a frequency-domain CFD method, using aerodynamic eigenmodes.

The present study uses the CFD time-marching method, CFL3D v6, to numerically investigate transonic LCO of a two-dimensional supercritical wing under a plunging/pitching spring-mounting system [70, 71, 75]. It is reasonable to start by investigating a two-dimensional LCO case in order to better understand the physics of LCO. However, because of the complexity of a two-dimensional LCO experimental test, there are few experimental data available for comparison. To the best of our knowledge, the experimental work performed by Schewe et. al. [70, 71, 75], is perhaps the only two-dimensional LCO experimental test available in the literature. Those test data were immediately used by Platzer et. al. to validate their thin-layer Navier-Stokes aeroelastic solver [60, 77]. While the emphasis of [60, 77], was on the predictive capability of the thin-layer Navier-Stokes aeroelastic solver, our emphasis here is to investigate the effect of aerodynamic viscosity, turbulence modeling and solution strategies, such as initial perturbation size, on transonic LCO of the supercritical airfoil. Also addressed in the paper are some of the issues related to multiblock MPI parallel aeroelastic computation of this problem.

4.2 Numerical Methodology

The computer code used in this study is CFL3D v6, which solves the three-dimensional thin-layer Reynolds averaged Navier-Stokes equations with an upwind finite volume formulation [72]. A two-dimensional problem can be calculated by using two identical grid planes, created by duplicating the two-dimensional grid.

The code uses formally third-order upwind-biased spatial differencing for the inviscid terms with flux limiting in the presence of shocks. Either flux-difference or flux-vector splitting are available. The flux-difference splitting method of Roe (1981) is employed in the present computations to obtain fluxes at cell faces. Viscous terms are discretized with second-order central differencing. There are two types of time discretization available in the code. The first-order backward time differencing is used for steady calculation while the second-order backward time differencing with t-TS subiterations is used for static and dynamic aeroelastic calculation. Furthermore, grid sequencing for steady state and multigrid and local pseudo-time stepping for time marching solutions are employed. Also available in the code are many turbulence models, although here only the Spalart-Allmaras model [76], and Baldwin-Lomax model [58], with the Degani-Schiff modification have been used. A detailed description of the methodology of the code can be found in [72].

One of the important features of the CFL3D code is its capability of solving multiple zone grids with one-to-one connectivity. Spatial accuracy is maintained at zone boundaries, although subiterative updating of boundary information is required. Coarse-grained parallelization using the MPI protocol can be utilized in multiblock computations by solving one or more blocks per processor. When there are more blocks than processors, optimal performance is achieved by allocating an equal number of blocks to each processor. As a result, the time required for a CFD-based aeroelastic computation can be dramatically reduced. In this paper, both single and multiblock MPI parallel aeroelastic computations near the onset of flutter LCO are compared with experiment and with other computations. Figure 4.2 shows a C-type grid with 273 x 93 mesh points around the NLR 7301 airfoil that has been divided into eight 69x47 blocks. This and a single block version of this grid are used in the computations to follow.

In order to accommodate multiblock computation, the mesh deformation scheme in [59] is modified. In [59], the remeshing scheme uses a modified spring analogy with solid body translation/rotation of the fluid mesh near solid surfaces. Initialization of the grid deformation at each step is performed using a TFI (Transfinite Interpolation) step. The mesh interior is then smoothed and grid orientation near boundaries is preserved using the modified spring analogy.

In the present implementation, the subgrid based TFI scheme of [68], has been employed for initialization at each time step. That scheme uses subgrids consisting of "slave vertices" to move both block boundaries and interiors. In some instances, in order to achieve an optimal division of grid points, it is necessary to place flow field block boundaries near a moving solid

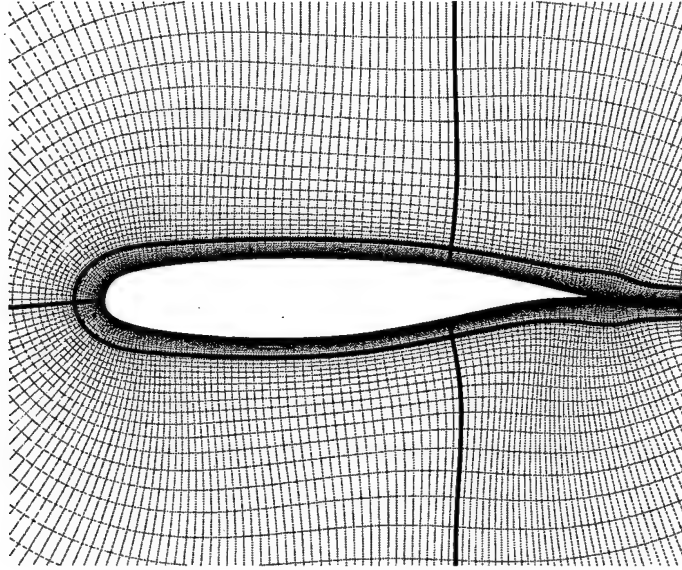


Figure 4.2: Multiblock C-type grid around NLR 7301 airfoil (eight 69x47 blocks).

surface. An example of this is shown in Figure 4.2. The multiblock boundary and interior movement scheme allows the user to place block boundaries near surfaces as necessary for optimal parallelization. Boundaries interior to the fluid domain near a surface respond to the local surface motion. As the airfoil moves, block boundaries move to maintain integrity of block interfaces and the airfoil surface.

User controlled input makes it possible to update the mesh using this subgrid/TFI-based scheme alone or to update with an initialization using this scheme plus additional smoothing steps. These added smoothing steps, the number of which can be defined by the user, employ the modified spring analogy scheme [59]. In the current implementation the spring analogy scheme updating the mesh interior is now written in delta formulation so that the relative orientation of the original grid is retained. The solid body rotation/translation of the fluid grid is also now performed near both solid surface and block fluid boundaries.

The time-marching simulation of the aeroelastic responses is obtained using the state transition matrix solution from t to $t+\Delta t$ of the state variable representation of the decoupled modal equations [62, 65]. The state transition matrix based scheme is optimal in the sense that it is derived from an exact solution of the free response of the modal equations. The actual scheme uses predictor/corrector steps. The predictor step marches the structure using the solution of the modal equations at the step n to get the surface deflection at the time step $n+1$. This provides the surface shape for a recomputation of the fluid mesh and the fluid domain solution at $n+1$. After a solution of the fluid domain involving multiple subiterations, the corrector step then solves the modal equations at the time step $n+1$ using the averaged generalized forces at n and $n+1$.

Because the CFD and CSM meshes usually do not match at the interface, CFD/CSM cou-

pling requires a surface spline interpolation between the two domains. The interpolation of CSM mode shapes to CFD surface grid points is done as a preprocessing step. Modal deflections at all CFD surface grids are first generated. Modal data at these points are then segmented based on the splitting of the flow field blocks. Mode shape displacements located at CFD surface grid points of each segment are used in the integration of the generalized modal forces and in the computation of the deflected surface. The final surface deformation at each time step is a linear superposition of all the modal deflections.

The following is an account of our theoretical modeling of Schewe's experiment on transonic flutter of a two-dimensional supercritical wing with an NLR7301 airfoil section [70, 71, 75]. Figure 4.3 depicts a simplified model of the two-degree-of-freedom test set-up. The two-dimensional wing has a chord length of 0.3 m ($c = 0.3$ m) and a span of 1 m ($b = 1$ m). The pitching spring and the plunging spring are attached to the same $c/4$ position. The corresponding two-degree-of-freedom equation of motion of the set-up reads

$$\begin{bmatrix} m_h & -s_\alpha \\ -s_\alpha & I_{c/4} \end{bmatrix} \begin{Bmatrix} \ddot{h} \\ \ddot{\alpha} \end{Bmatrix} + \begin{bmatrix} D_h & 0 \\ 0 & D_\alpha \end{bmatrix} \begin{Bmatrix} \dot{h} \\ \dot{\alpha} \end{Bmatrix} + \begin{bmatrix} K_h & 0 \\ 0 & K_\alpha \end{bmatrix} \begin{Bmatrix} h \\ \alpha - \alpha_0 \end{Bmatrix} = \begin{Bmatrix} L(t) \\ M(t) \end{Bmatrix} \quad (4.1)$$

where m_h is the total mass ($m_h = 26.64$ kg), $I_{c/4}$ is the mass moment of inertia about $c/4$ ($I_{c/4} = 0.086$ kg-m²), s_α is the static unbalance ($s_\alpha = 0.378$ kg-m), D_h and D_α are the damping factors of the plunging motion (h) and the pitching motion (α) respectively ($D_h = 82.9$ kg/s and $D_\alpha = 0.197$ kg-m²/(rad-s)), K_h and K_α are the stiffness of the plunging spring and the pitching spring respectively ($K_h = 1.21 \times 10^6$ N/m and $K_\alpha = 6.68 \times 10^3$ N-m/rad), and $L(t)$ and $M(t)$ are the aerodynamic lift and moment respectively in Newtons.

The aeroelastic equations and the CFD grid are maintained in dimensional form. To perform the time-marching CFD computation in CFL3D v6.0, it is necessary to convert equation (1) into modal coordinates, i.e.,

$$\begin{Bmatrix} h \\ \alpha \end{Bmatrix} = [\phi]q \quad (4.2)$$

where q is the modal coordinate and ϕ is the modal matrix of the undamped structure. For this numerical example we have

$$\phi = \begin{bmatrix} -0.1735 & 0.1004 \\ 0.9277 & 3.403 \end{bmatrix} \quad (4.3)$$

Substituting equation (2) into equation (1) and pre-multiplying the resulting equation by ϕ^T yields

$$[I]\ddot{q} + \begin{bmatrix} 2\omega_h\zeta_h & 0 \\ 0 & 2\omega_\alpha\zeta_\alpha \end{bmatrix} \{\dot{q}\} + \begin{bmatrix} \omega_h^2 & 0 \\ 0 & \omega_\alpha^2 \end{bmatrix} \{q\} = \phi^T \begin{Bmatrix} L(t) \\ M(t) \end{Bmatrix} \quad (4.4)$$

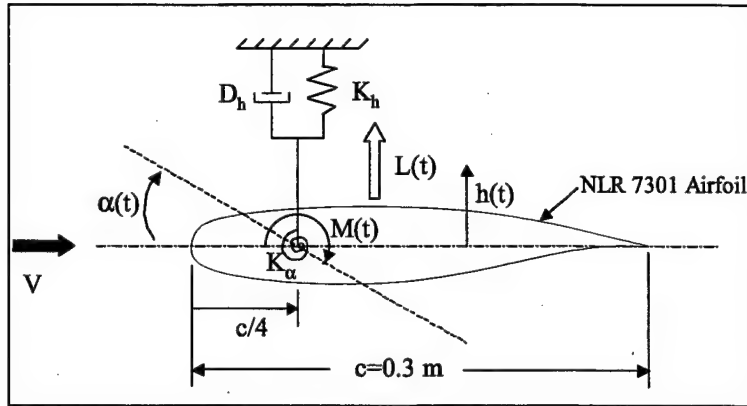


Figure 4.3: Two-Degree-of-Freedom Dynamic Model.

where ω_h and ω_α are the undamped natural frequencies of the plunging and pitching motions respectively ($\omega_h = 205.4$ rad/s and $\omega_\alpha = 299.3$ rad/s), ζ_h and ζ_α are the plunging and pitching damping ratios respectively ($\zeta_h = 0.00649$ and $\zeta_\alpha = 0.00521$). Note that the off-diagonal terms in the damping matrix are assumed to be zero for simplicity.

4.3 Results and Discussion

The simulated case here is the measurement No.77 documented in [71]. As mentioned before, the experimental model was a two-dimensional supercritical wing with NLR7301 section. The chord length of the wing was 0.3 m and the angle of attack was 1.28°. The experimental conditions were the freestream Mach number of 0.768 and the Reynolds number of 1.727×10^6 based on the chord length. A transonic LCO in two-degrees-of-freedom was found at the dynamic pressure of 0.126 bar. The corresponding free-stream velocity was 254.7 m/s. The total pressure was 0.45 bar.

As discussed in [60, 77], because of the relatively large chord length of the airfoil with respect to the wind tunnel test section (1 m x 1 m), both the freestream Mach number and the angle of attack need to be corrected to take into account wind tunnel wall effects. The criterion used in [60, 77] was to match the computed to the measured time-averaged surface pressure distribution.

4.4 Time-Averaged Surface Pressure Distribution

An Euler computation is first performed on a C-type grid with 293 x 61 points. The best agreement with the experimental data is found at $M = 0.734$ and $\alpha = -0.25^\circ$. Figure 4.4 indicates that even for this corrected Mach number and the corrected angle of attack, the predicted shock strength is stronger than the experimental result and the location of the shock is behind the measured one. It seems impossible to match both the measured

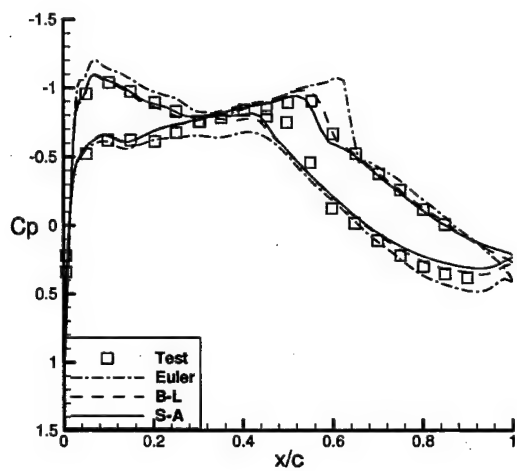


Figure 4.4: Time-Averaged Surface Pressure Distribution (spring-off).

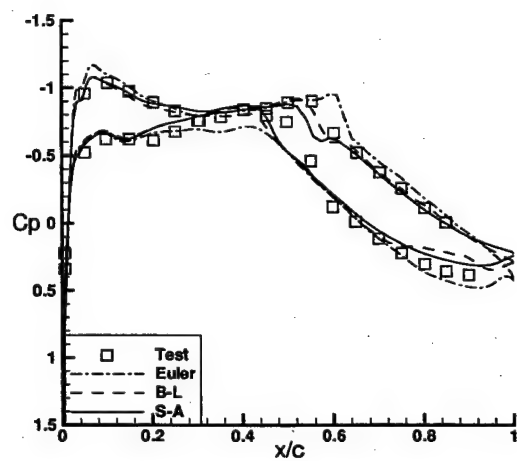


Figure 4.5: Time-Averaged Surface Pressure Distribution (spring-on).

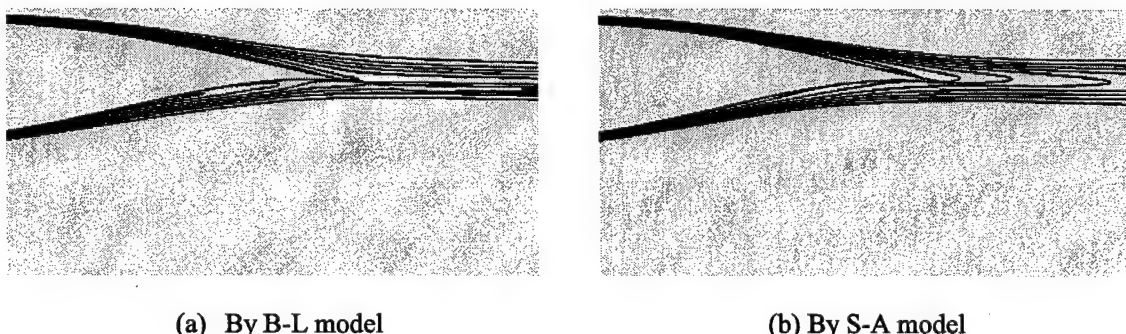


Figure 4.6: Entropy Contours (spring-on): (a) by B-L-D-S model; (b) by S-A model.

strength and location of the shock with Euler computation. Two viscous computations are then performed on a C-type grid with 293×93 points. One uses the Degani-Schiff modified Baldwin-Lomax turbulence model (B-L), and the other uses Spalart-Allmaras turbulence model (S-A). The corrected Mach number is found to be 0.748 for both models while the corrected angle of attack is -0.02° for the B-L model and 0.15° for the S-A model. It is found in Figure 4.4 that both viscous results have a closer agreement with the experimental data, especially for shock strength and location, clearly showing that viscous effects are important for the accurate prediction of the shock.

The above computed results are for the spring-off condition. With taking into account the contribution from the structure part, the corrected angle of attack becomes -0.1° for Euler computation, 0.15° for the B-L model, and 0.32° for the S-A model. The corrected Mach number does not change for both Euler computation and the B-L model but shifts to 0.75 for the S-A model. These numbers will be used as inputs for the further dynamic aeroelastic computations.

One important phenomenon in Figure 4.5 is that the B-L model produces a pressure or lift loss on the lower surface near the trailing edge, which is not found in Figure 4.4, the spring-off condition. In order to understand the mechanism behind this phenomenon, Figure 4.6 presents the entropy contours given by the two turbulence models. It is found that the B-L model seems to produce spurious vorticity on the lower surface near the trailing edge for the static aeroelastic computation.

4.5 Performance and Time Step Convergence

The static aeroelastic case is used to compare run times between the single and 8 block/MPI parallel computations. Starting from a steady state a time-accurate aeroelastic solution is marched for 800 time steps at 5 multigrid subiterations each. The S-A turbulence model is used in each case.

Table 1 gives performance data for the various grids, run modes, and code configurations. The first two rows in the table represent sequential computation of the 1 and 8 block versions of the grid. The 8-block grid takes 28% less CPU time than the 1-block grid, apparently due to better caching of the smaller sized blocks. The parallel computation with 8 processors runs 7.8 times faster than the same run sequentially. The last two rows present the computational effort required for the spring analogy smoothing step and the combined TFI and aeroelasticity. Three iterations of the spring analogy scheme add about 1.5% computing time to the solution. The TFI grid movement and the aeroelastic computation add about 10% to the run time.

Table 2 shows solution behavior for the single block grid for successive time step sizes. These are computed at $M_\infty = 0.753$, $\alpha = 0.6^\circ$ and a dynamic pressure of 0.126 *bar*, using the S-A model. Initialization is accomplished with a static aeroelastic solution, followed by an initial

Grid/Comp. Type	TFI	Spr. Anal. Smoothing	CPU Time/Processor (seconds)
1 block/seq	Yes	Yes	8800
8 block/seq	Yes	Yes	5430
8 block/MPI	Yes	Yes	690
8 block/MPI	Yes	No	680
8 block/MPI*	No	No	610

* also without aeroelasticity

Table 4.1: Cost/Performance

Δt	$a_h(\text{mm})$	$a_\alpha(\text{Deg.})$	$\omega_h(\text{Hz})$	$\omega_\alpha(\text{Hz})$
0.128	11.2	3.72	34.5	34.5
0.040	9.17	3.24	34.3	34.3
0.0125	8.99	3.17	34.3	34.3

Table 4.2: Time Step Convergence, 1 Block Grid

perturbation of the dynamic simulation of -0.00114 in the velocity of the second mode. The time step sizes give 80, 250, and 800 time steps per pitch/plunge cycle. Nine subiterations per time step are used. Columns two and three are half amplitudes of the fully developed LCO plunge and pitch, while columns four and five are the plunge/pitch frequencies. Frequencies and amplitudes are computed based on a sampling of the last 8-10 cycles of motion; from this sampling the data appears to be nearly converged at the smallest time step. At the largest time step, even after 100 cycles, the amplitude slowly continued to grow while at the two smaller time steps the amplitude fully converged to LCO. In all of the remaining dynamic computations, the smallest time step size with nine multigrid subiterations is used.

The speed increase offered by computing in parallel is appealing. There are trade offs of course when using coarse grain parallelization. Depending on the block splitting and problem, the multiblock computations can require substantially more subiterations. This fact is most evident in the problem at hand. Figure 4.7 shows a comparison between the same LCO computed on a single flow field block and the same grid divided into 8 blocks. The 8-block grid is shown in Figure 4.2. By viewing the right hand plots in that figure it is clear that eventually the amplitude and frequency of the multiblock pitch and plunge had settled out and converged to values virtually identical to that of the single block grid ($a_h = 8.87 \text{ mm}$, $a_\alpha = 3.13^\circ$, $\omega_h = \omega_\alpha = 34.3 \text{ Hz}$). This would not be the case if the multiblock aeroelastic coupling and integration were not consistent with that of the single block configuration. Yet as shown in Figure 4.7 the time at which the LCO can be considered converged is different between the two computations. This accounts for the different values of t_0 for the 1 block and 8 block computations. As seen in the left hand plots in Figure 4.7, the LCO computed with 8 flow field blocks takes much longer to develop than does an identical LCO computed on a single flow field block.

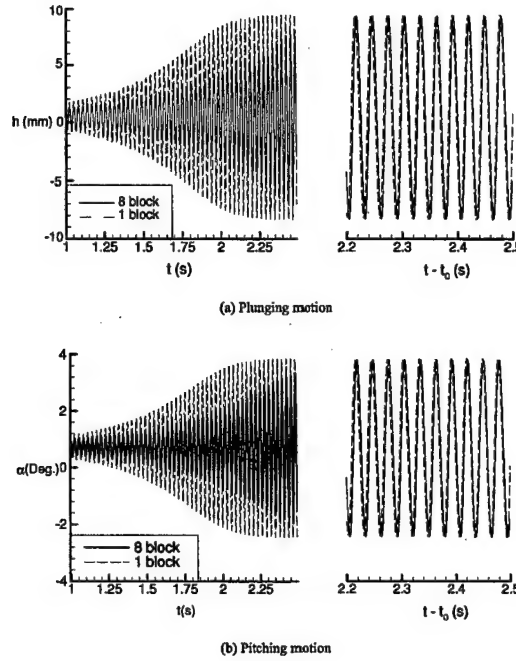


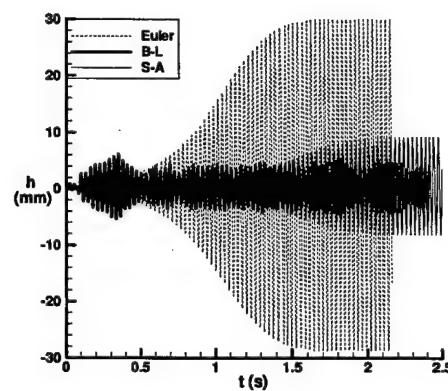
Figure 4.7: Comparison of Single/Multiblock Grid Computations ($N-S$, $M_\infty = 0.753$, $\alpha = 0.6^\circ$) $t_0=4.5s$ (8 blocks): (a) Plunge Motion; (b) Pitch Motion.

4.6 Effect of Viscosity and Turbulence Modeling

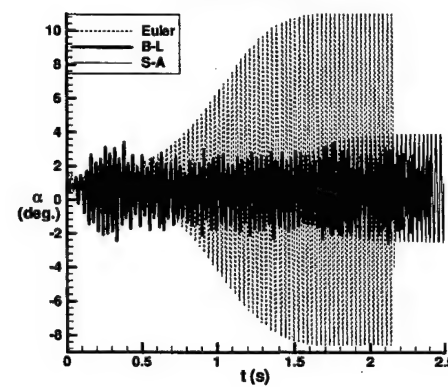
Figure 4.8 compares LCO predicted by Euler and Navier-Stokes methods. It is found that although both inviscid and viscous computations are able to predict LCO, the amplitude of LCO given by viscous computations is less than 1/3 of that predicted by inviscid computation, much closer to the experimental data (plunging and pitching amplitudes are 0.65 mm and 0.18° respectively). Therefore, it is important to include the viscous terms in LCO computations, which effect is to limit the amplitude of the flutter LCO.

Also shown in Figure 4.8 is the difference between LCO predicted by the two turbulence models. It is found that the B-L model reaches large amplitude limit cycle quite rapidly. Plunge and pitch amplitudes of the B-L result are around 4 mm and 2° respectively. The predicted frequency is 32.2 Hz. On the other hand, the S-A model reaches LCO much later. Its plunge and pitch amplitudes are larger than those given by the B-L model, around 9 mm and 3° respectively. Furthermore, the B-L LCO is a random/chaotic output while the S-A LCO is a perfect sine-wave output. It is clear that the turbulence model significantly alters the nature of the solution.

In order to understand the mechanism behind the differences caused by the two turbulence models, Figure 4.9 further presents the predicted density contours at 8 time steps uniformly

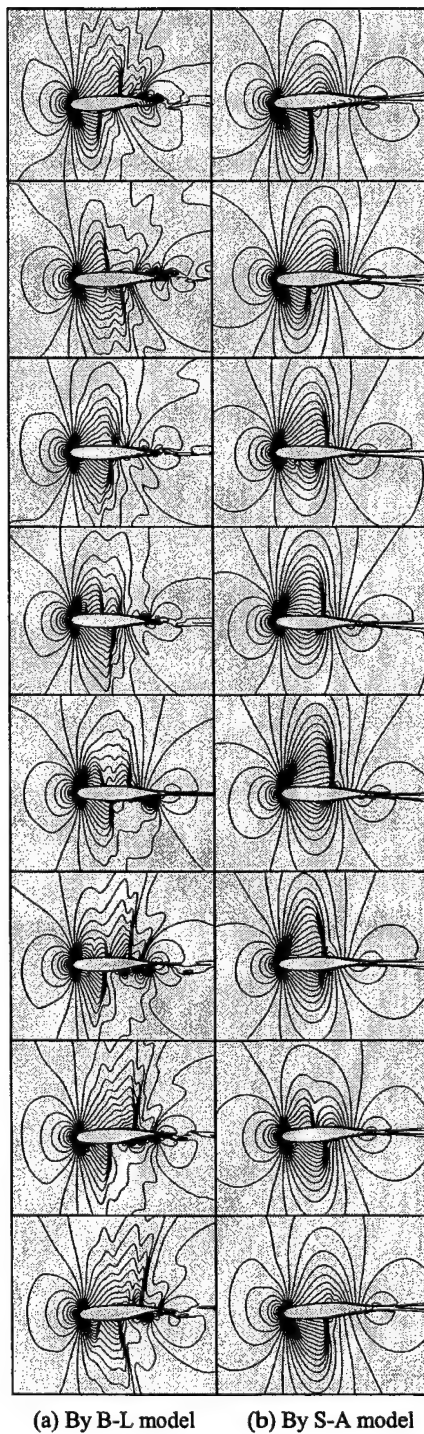


(a) Plunging motion



(b) Pitching motion

Figure 4.8: LCO Predicted by Euler/N-S Methods: (a) Plunge Motion; (b) Pitch Motion.



(a) By B-L model (b) By S-A model

Figure 4.9: Predicted Density Contours: (a) by B-L-D-S Model; (b) by S-A Model.

distributed in the last cycle. The B-L results presented at the left hand side clearly show multishocks with large excursions possibly caused by spurious vorticity separation. This is why the B-L LCO exhibits chaotic behavior. On the other hand, no visible vorticity separation is found in the S-A results presented at the right hand side. As a result, the flow pattern is much more regular.

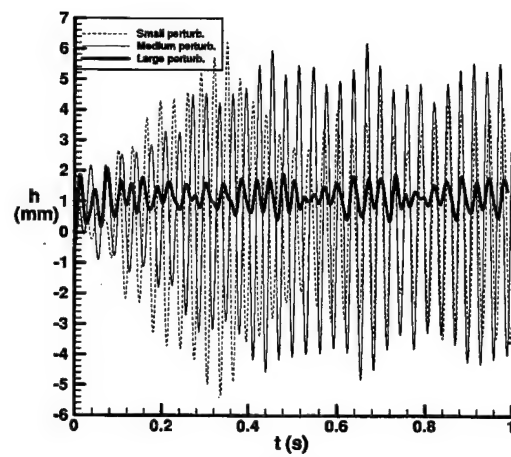
4.7 Effect of Perturbation Size

The above LCO computations are performed with a small initial perturbation (-0.0012 in the velocity of the second mode). In order to investigate the effect of initial perturbation size, the earlier simulations are repeated with the two larger initial perturbations. The one referred to as the medium perturbation in Figures 4.10 and 4.11 has 5 times of the original perturbation size (-0.006 in the velocity of the second mode), and that referred to as the large perturbation has 10 times of the original perturbation size (-0.012 in the velocity of the second mode).

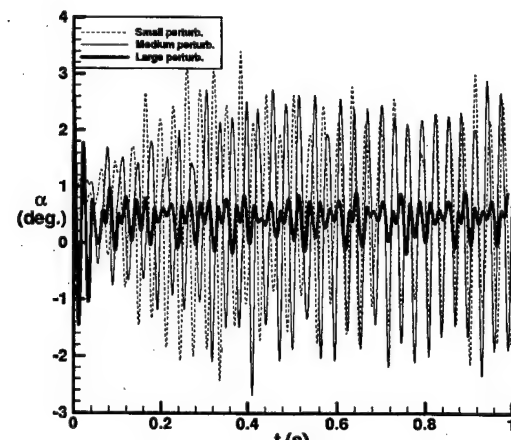
Results given by the B-L model are shown in Figure 4.10. It is found that although the LCO amplitudes are in the same level for small and medium perturbations, the LCO amplitudes for large perturbation is significantly reduced. This is contradicted to common sense. However, this phenomenon can even be more clearly seen in Figure 4.11, which are S-A results. From small perturbation to medium perturbation, LCO occurs earlier and the amplitudes of both plunging and pitching modes are slightly reduced. Further increasing the perturbation size by two, a converged solution is achieved. Larger perturbation sizes correspond to stronger nonlinear aerodynamic effects. So, the above results mean that nonlinear aerodynamic effects tend to stabilize the flutter.

4.8 Conclusions

Stronger nonlinear aerodynamic effects, including adding the viscous terms and increasing perturbation size, tend to reduce LCO amplitudes and even stabilize the dynamic solution. Viscous LCO computation is turbulence model dependent. Specifically, B-L model with Degani-Schiff modification results in multishocks with large excursions possibly caused by spurious vorticity generation.

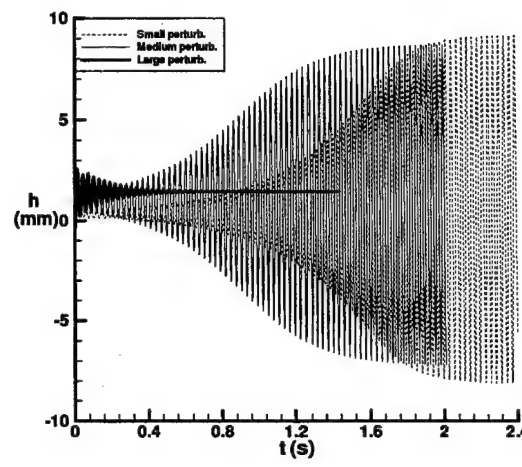


(a) Plunging mode

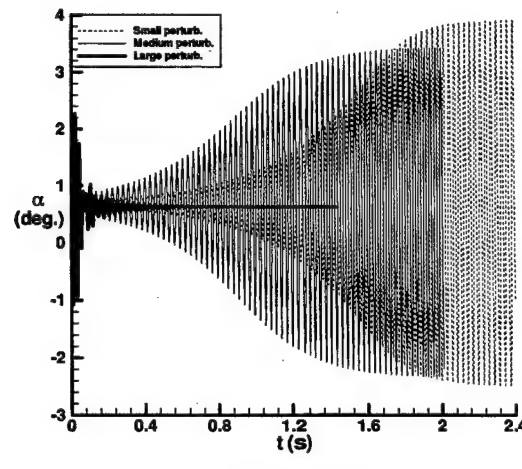


(b) Pitching mode

Figure 4.10: Effect of Initial Perturbation Sizes: (a) Plunge Motion; (b) Pitch Motion.



(a) Plunging mode



(b) Pitching mode

Figure 4.11: Density Contours Showing Effect of Initial Perturbation Sizes: (a) 1st Cycle; (b) 2nd Cycle; (c) 3rd Cycle; (d) Final LCO Cycle.

Chapter 5

Theoretical Background of the Harmonic Balance Method in Three-Dimensions

Summary

In order to facilitate the three-dimensional work in the following chapters. Theoretical background of the Harmonic Balance Method in three dimensions will be described in this chapter. The sections that follow include:

- *Three Dimensional Navier-Stokes and Euler Equations*
- *Harmonic Balance*
- *Time-Linearized Flow/Three Dimensional Flow Solver*
- *Reduced Order Modeling of Time-Linearized Aerodynamic Models*
- *Reduced Order Aeroelastic Model for Multi-Degree-Of-Freedom Structures*
- *Structural/Compatible Reduced Order Aeroelastic Model*

5.1 Three-Dimensional Navier-Stokes and Euler Equations

We start with the top-down approach:

The 3-D Reynolds-Averaged Navier-Stokes Equations read:

$$\frac{\partial U}{\partial t} + \frac{\partial(F - F_v)}{\partial x} + \frac{\partial(G - G_v)}{\partial y} + \frac{\partial(H - H_v)}{\partial z} = 0 \quad (5.1)$$

where:

$$U = \begin{Bmatrix} \rho \\ \rho u \\ \rho v \\ \rho w \\ \rho e \end{Bmatrix}, F = \begin{Bmatrix} \rho u \\ \rho u^2 + p \\ \rho u v \\ \rho u w \\ \rho u h \end{Bmatrix}, G = \begin{Bmatrix} \rho v \\ \rho u v \\ \rho v^2 + p \\ \rho v w \\ \rho v h \end{Bmatrix}, H = \begin{Bmatrix} \rho w \\ \rho u w \\ \rho v w \\ \rho w^2 + p \\ \rho w h \end{Bmatrix},$$

$$F_v = \begin{Bmatrix} 0 \\ \tau_{xx} \\ \tau_{xy} \\ \tau_{xz} \\ \tau_{xx}u + \tau_{xy}v + \tau_{xz}w \end{Bmatrix}, G_v = \begin{Bmatrix} 0 \\ \tau_{yx} \\ \tau_{yy} \\ \tau_{yz} \\ \tau_{yx}u + \tau_{yy}v + \tau_{yz}w \end{Bmatrix}, H_v = \begin{Bmatrix} 0 \\ \tau_{zx} \\ \tau_{zy} \\ \tau_{zz} \\ \tau_{zx}u + \tau_{zy}v + \tau_{zz}w \end{Bmatrix},$$

and ρ , p , (u, v, w) , e , h are the flow density, pressure, velocity, energy and enthalpy, respectively. $\tau_{xx}, \tau_{xy}, \tau_{xz}, \cdot$, etc are the Reynolds stress tensors.

In what follows, we will reduce Eq (5.1) to 3-D and 2-D Euler equations for the convenience of elucidating the frequency-domain POD/ROM approach.

5.2 Harmonic Balance

In Phase I, the importance of aerodynamic nonlinearities on LCO was assessed using a novel two-dimensional harmonic balance (H.B.) technique. With this approach, the unsteady flow variables can be represented by a Fourier Series in time with spatially varying coefficients. This assumption leads to a set of harmonic balance Euler equations, which can be solved efficiently using conventional CFD methods including time marching with local time stepping and multi-grid acceleration. The two-dimensional Euler equations are:

$$\frac{\partial U}{\partial t} + \frac{\partial F}{\partial x} + \frac{\partial G}{\partial y} + \text{partialy} = 0 \quad (5.2)$$

where the flux vectors U , F and G are given by

$$U = \begin{Bmatrix} \rho \\ \rho u \\ \rho v \\ \rho w \\ \rho e \end{Bmatrix}, F = \begin{Bmatrix} \rho u \\ \rho u^2 + p \\ \rho u v \\ \rho u w \\ \rho u h \end{Bmatrix}, G = \begin{Bmatrix} \rho v \\ \rho u v \\ \rho v^2 + p \\ \rho v w \\ \rho v h \end{Bmatrix}, H = \begin{Bmatrix} \rho w \\ \rho u w \\ \rho v w \\ \rho w^2 + p \\ \rho w h \end{Bmatrix} \quad (5.3)$$

Next, representing conservation prime variables by sum of harmonics of fundamental frequency gives:

$$\begin{aligned}\rho(x, y, t) &= \sum_n R_n(x, y) e^{i\omega n t}, \rho u(x, y, t) = \sum_n U_n(x, y) e^{i\omega n t} \\ \rho v(x, y, t) &= \sum_n V_n(x, y) e^{i\omega n t}, \rho e(x, y, t) = \sum_n E_n(x, y) e^{i\omega n t}\end{aligned}\quad (5.4)$$

Requiring each frequency component to vanish independently (harmonic balance) and collecting terms of like harmonics results in

$$\frac{\partial \bar{U}(V)}{\partial t} + \frac{\partial \bar{F}(V)}{\partial x} + \frac{\partial \bar{G}(V)}{\partial y} = 0 \quad (5.5)$$

where

$$\mathbf{V} = \{\dots R_0, U_0, V_0, E_0, R_{+1}, U_{+1}, V_{+1}, E_{+1}, \dots\}^T$$

and

$$\frac{\partial \bar{U}}{\partial t} = i\omega \{ \dots 0 \cdot R_0, 0 \cdot U_0, 0 \cdot V_0, 0 \cdot E_0, +1 \cdot R_{+1}, +1 \cdot U_{+1}, +1 \cdot V_{+1}, +1 \cdot E_{+1} \}^T \quad (5.6)$$

By adding a 'pseudo-time' term, Eq (5.5) can be solved by a conventional CFD solution, i.e.,

$$\frac{\partial V}{\partial \tau} + \frac{\partial \bar{F}(V)}{\partial x} + \frac{\partial \bar{G}(V)}{\partial y} + \frac{\partial \bar{U}(V)}{\partial t} = 0 \quad (5.7)$$

Note that harmonic balance equations are similar in form to original Euler equations. Thus, existing Euler codes can be modified to solve H.B. equations. A two-step Lax-Wendroff scheme will be used. Also, since only "steady-state" solution is desired, one can use local time stepping, multiple-grid acceleration techniques and residual smoothing to speed convergence. The method is computationally very efficient, at least one to two orders-of-magnitude faster than nonlinear time-domain CFD simulations.

In Phase II, we will use the two-dimensional, nonlinear, harmonic balance aerodynamic code and add viscosity terms, i.e., we will develop a Navier-Stokes version of this analysis suitable for the analysis of oscillating airfoils. In addition, we will use this code to perform LCO analysis and prediction for simple structural models, e.g. plunge and pitch of a typical section for conventional and supercritical airfoils. In particular, we will perform correlation studies with the DLR experimental data of the NLR 7301 LCO case.

In Phase I, a three-dimensional time-linearized unsteady aerodynamic analysis was developed. In Phase II, this code will be converted to a harmonic balance analysis of three-dimensional inviscid transonic flows. We will use this three-dimensional analysis to perform LCO analyses of simple linear wing structural models. We will perform LCO correlation studies with a business jet wing or other wing to be determined.

In passing, we note the following when using aeroelastic eigenmodes for LCO prediction. The harmonic balance method has proven to be a very effective method for determining limit cycle oscillations (LCO) and other nonlinear responses of aeroelastic systems. It is often more computationally efficient and gives greater physical insight than, for example, time marching simulations. On the other hand it has some limitations, e.g. it does not allow an investigation of the possible dependence of the response on the initial conditions. Nor does it allow a precise assessment of non-periodic and chaotic motions. At best the harmonic balance method can only approximate a non-periodic motion. In practice these limitations are not often serious drawbacks; however these observations do suggest that future work may well involve a balanced consideration of both time simulations and frequency domain (harmonic balance) studies.

Another consideration is the number of harmonics to be retained in a harmonic balance analysis. If there is a dominant harmonic, a single harmonic may suffice, although it will be important to assess the effects of higher harmonics on the fundamental harmonic *per se*. And finally the algebraic complexity of using the method for multi-modal systems may quickly get out of hand unless special measures are taken to deal with this issue. We will return to this latter issue as, even with reduced order aerodynamic modeling of the structure and fluid, the order of the reduced model will be larger than that often encountered in classical harmonic balance analyses, i.e., on the order of several tens of states.

5.3 Time-Linearized Flow Three-Dimensional Flow Solver

In Phase I, we developed a three-dimensional time-linearized Euler analysis of unsteady flow about a wing. We start with the assumption that the unsteady flow $\hat{\mathbf{u}}(x, y, z, t)$ may be expanded in a perturbation series of the form

$$\hat{\mathbf{u}}(x, y, z, t) = \mathbf{U}(x, y, z) e^{i\omega t} \quad (5.8)$$

where $\mathbf{U}(x, y, z, t)$ represents the steady background flow, and $\mathbf{u}(x, y, z, t)$ is the complex amplitude of the unsteady small-disturbance flow arising from the wing vibration, which vibrates at frequency ω . Substituting Eq (5.8) into the nonlinear three-dimensional Euler equations, and expanding the result in a perturbation series in the small-disturbance quantities, one finds that to zeroth and first order the governing equations reads respectively

$$\frac{\partial \mathbf{F}(\mathbf{U})}{\partial x} + \frac{\partial \mathbf{G}(\mathbf{U})}{\partial y} + \frac{\partial \mathbf{H}(\mathbf{U})}{\partial z} = 0 \quad (5.9)$$

$$i\omega \mathbf{u} + \frac{\partial}{\partial x} \left(\frac{\partial \mathbf{F}}{\partial \mathbf{U}} \mathbf{u} \right) + \frac{\partial}{\partial y} \left(\frac{\partial \mathbf{G}}{\partial \mathbf{U}} \mathbf{u} \right) + \frac{\partial}{\partial z} \left(\frac{\partial \mathbf{H}}{\partial \mathbf{U}} \mathbf{u} \right) = 0 \quad (5.10)$$

In a conventional time-linearized analysis, Eq (5.9) and Eq (5.10) are solved using pseudo time marching and standard CFD techniques. Note that since time does not appear explicitly in either equation, they both may be solved using computational acceleration techniques

such as multiple grid acceleration, local time stepping, and residual smoothing. The result is that these two equations can be solved at a fraction of the cost of solving the full nonlinear Euler equations using conventional time marching.

In Phase I, a simple clean wing model was developed. This CFD analysis used a simple grid structure that limited the approach to clean wings. In Phase II, this model will be extended to allow more complicated grid topologies, which will allow us to analyze multi-body configurations, e.g. wing/store.

5.4 Reduced Order Modeling of Time-Linearized Aerodynamic Models

Having developed a three-dimensional time-linearized flow solver, we next consider the reduction of that model using proper orthogonal decomposition techniques (POD). The idea behind the frequency domain proper orthogonal decomposition is a simple one. We first calculate the small-disturbance response of the aerodynamic system at M different combinations of frequency and excitation. The solutions, also called "snapshots," are denoted by \mathbf{q}^m for $m=1,2,..,M$. These snapshots are then linearly combined to form a smaller number of basis vectors ϕ_k for $k=1,2,..,K$ where $K \ll M$. In other words,

$$\phi_k = \mathbf{Q}\mathbf{v}_k \text{ for } k = 1, 2, \dots, K \quad (5.11)$$

where the m^{th} column of \mathbf{Q} is just \mathbf{q}^m . In the proper orthogonal decomposition technique, the vectors \mathbf{v}_k are found by solving a small eigenvalue problem of the form

$$\mathbf{Q}^H \mathbf{Q} \mathbf{v}_k = \lambda_k \mathbf{v}_k \quad (5.12)$$

Only the eigenvectors \mathbf{v}_k with the largest eigenvalues λ_k are used to form basis vectors defined by Eq (5.11). \mathbf{Q}^H is the Hermitian of \mathbf{Q} .

Having computed the POD basis vectors, we assume that they will provide a useful basis for computing the unsteady solution at some other frequency and/or external excitation than was used to generate the original snapshots. Thus, we let

$$\mathbf{q} = \Phi \xi \quad (5.13)$$

where Φ is an $N \times K$ matrix whose k^{th} column is simply the basis vector ϕ_k , and ξ is a vector of aerodynamics state variables.

We note that when discretized, Eq (5.10) has the form

$$\mathbf{A}\mathbf{q} = \mathbf{A}_0\mathbf{q} + i\omega\mathbf{A}_1\mathbf{q} = \mathbf{b}_0 + i\omega\mathbf{b}_1 \quad (5.14)$$

where \mathbf{A}_0 and \mathbf{A}_1 are independent of the excitation frequency ω , and are purely real, and \mathbf{q} is the vector containing \mathbf{u} at all the nodes of the CFD grid.

Substitution of Eq (5.11) into Eq (5.14), and projection of the error onto the space spanned by the basis vectors gives

$$\Phi^H \mathbf{A} \Phi \xi = \mathbf{A}_R \xi = \Phi^H \mathbf{b} \quad (5.15)$$

Finally, the reduced-order aerodynamic matrix \mathbf{A}_R , which is much smaller than the original aerodynamic matrix \mathbf{A} , is factored using LU decomposition, and Eq (5.15) is solved for the unknown aerodynamic state variables. This step is computationally very efficient because the reduced-order aerodynamic matrix is small, sometimes as small as 10x10, but rarely larger than 100x100. The major expense in constructing the reduced-order aerodynamic model is the computation of the snapshots; the cost of finding the basis vectors and solution to Eq (5.15) is negligible by comparison.

Having described the basic reduced-order modeling technique, we next describe how to incorporate an aerodynamic reduced-order model into an aeroelastic model of flutter. Consider, for example, a two degree-of-freedom structural dynamic model of a typical section. The governing equations of motion are of the form

$$\mathbf{M} \ddot{\mathbf{h}} + \mathbf{K} \mathbf{h} = \mathbf{f} \text{ where } \mathbf{h} = \{h, \alpha\}^T \quad (5.16)$$

and h and α are the plunging and pitching degrees of freedom of the typical section. \mathbf{M} and \mathbf{K} are the mass and stiffness matrices, respectively.

Note that the aerodynamic force vector \mathbf{f} is obtained from integrals involving the pressure at the surface of the airfoil. When discretized, these integrals may be expressed as

$$\mathbf{f} = \mathbf{C} \mathbf{q} \quad (5.17)$$

where \mathbf{C} is a sparse $2 \times N$ matrix. Similarly, for the case of airfoil vibration, the vector \mathbf{b} on the right-hand side of Eq (5.14) can be expressed as

$$\mathbf{b} = \mathbf{b}_0 + i\omega \mathbf{b}_1 = \mathbf{B}_0 \mathbf{h} + i\omega \mathbf{B}_1 \mathbf{h} \quad (5.18)$$

where now we have made the assumption that the airfoil motion is harmonic in time although ω may be complex). For large CFD models, finding the eigenvalues is prohibitively expensive. To reduce the size of the model, we again assume that the number of aerodynamic states can be reduced using Eq (5.13). Again, projecting the error of the aerodynamic equations onto the space spanned by the aeroelastic basis vectors gives the desired reduced-order

aeroelastic model, i.e.,

$$\begin{bmatrix} \mathbf{A}_{R_0} & -\Phi^H \mathbf{B}_0 & -\Phi^H \mathbf{B}_1 \\ 0 & 0 & \mathbf{I} \\ -\mathbf{C}\Phi & \mathbf{K} & 0 \end{bmatrix} \begin{Bmatrix} \xi \\ \mathbf{h} \\ \dot{\mathbf{h}} \end{Bmatrix} + i\omega \begin{bmatrix} \mathbf{A}_{R_1} & 0 & 0 \\ 0 & -\mathbf{I} & 0 \\ 0 & 0 & \mathbf{M} \end{bmatrix} \begin{Bmatrix} \xi \\ \mathbf{h} \\ \dot{\mathbf{h}} \end{Bmatrix} = 0 \quad (5.19)$$

5.5 Reduced-Order Aeroelastic Model for Multi-Degree-Of-Freedom Structures

In Eq (5.19), we have derived a reduced-order aeroelastic model for a two degree of freedom (2 d.o.f.) structure, i.e., $\mathbf{h} = h, \alpha^T$. For multi-degree-of-freedom structures, \mathbf{h} can also be interpreted as the displacements of each degree of freedom in the structural model. In this situation, the size of Eq (5.19) becomes $K + 2n$, where n is the number of structural degrees of freedom. For a realistic wing structural model, n can be on the order of thousands, rendering Eq (5.19) a very large size eigenvalue problem. Solving such a large eigenvalue problem would practically be impossible.

5.5.1 The Modal Approach

To circumvent this problem, we introduce the so-called "*modal approach*" to Eq (5.19). The modal approach approximates \mathbf{h} by the superposition of the low-order structural modes, i.e.,

$$\mathbf{h} = \Psi_a \eta \quad (5.20)$$

where Ψ_a is the modal matrix whose columns contain the modal data of the low-order structural modes and η is the generalized coordinate vector. Since the magnitude of the modes can be arbitrary, they are usually normalized by the square root of their respective generalized masses, giving a unit generalized mass matrix. The justification for using the modal approach is based on the premise that most of the aeroelastic responses are dominated by the lower-order structural modes. Usually, for a single wing structure, the lowest ten (10) structural modes are sufficient to accurately represent \mathbf{h} . Substituting Eq (5.20) into Eq (5.19) and pre-multiplying the second and third rows of Eq (5.19) by Ψ_a^T yields

$$\begin{bmatrix} \mathbf{A}_{R_0} & -\Phi^H \mathbf{B}_0 \Psi_a & -\Phi^H \mathbf{B}_1 \Psi_a \\ 0 & 0 & \begin{bmatrix} \frac{1}{m_i} \\ \vdots \\ \frac{1}{m_i} \end{bmatrix} \\ -\Psi_a^T \mathbf{C}\Phi & [\omega_{n_i}^2] & [2\omega_{n_i} \zeta] \end{bmatrix} \begin{Bmatrix} \xi \\ \eta \\ \dot{\eta} \end{Bmatrix} + i\omega \begin{bmatrix} \mathbf{A}_{R_1} & 0 & 0 \\ 0 & \begin{bmatrix} \frac{1}{m_i} & \vdots & 0 \\ \vdots & \ddots & 0 \\ 0 & 0 & \mathbf{I} \end{bmatrix} & 0 \\ 0 & 0 & \mathbf{I} \end{bmatrix} \begin{Bmatrix} \xi \\ \eta \\ \dot{\eta} \end{Bmatrix} = 0 \quad (5.21)$$

where ω_{n_i} and m_i are the natural frequency and the generalized mass of the i^{th} structural mode, respectively. Now, the size of Eq (5.21) becomes $K + 2m$, where m is the number of structural modes. Because m is much less than the number of structural d.o.f. n , the size of the aeroelastic system is substantially reduced.

5.5.2 The Structural/Modal Damping

Note that a structural/modal damping matrix $\text{diag}[\dots 2\omega_{n_i}\xi \dots]$ has been added to Eq (5.21). With this added matrix, Eq (5.21) will facilitate our subsequent study of LCO. In an earlier LCO study, ZONA has suggested that the structural damping could play a decisive role in LCO for a wing/store system. For LCO study using the proposed method, one could alternatively use Eq (5.21) to delineate the effects with and without structural damping. Also note that the modal approach in fact increases the sparseness of the matrices in Eq (5.21). Thus, the eigenvalue problem of Eq (5.21) can be solved more efficiently by a sparse eigensolver.

5.6 Structural Compatible Reduced-Order Aeroelastic Model

One of the technical issues involved in the CFD aeroelastic computations is the displacement transferal from the structural finite element grid to the CFD surface grid. This technical issue arises from the problem where the CFD surface grid and the structural finite element (FEM) grid are considerably different; in their locations and densities. Solving such a displacement transferal problem of complex configuration such as whole aircraft with external stores is by no means a trivial task.

In March 1999, ZONA received a two-year contract from NASA/Langley to develop a Boundary Element Method (BEM), called the BEM Solver, for the data transferal between the FEM grid and the CFD surface grid (see Section 6.1, ZONA's Related Work). By formulating the data transferal problem as an equivalent solid mechanics problem, the BEM Solver generates a universal spline matrix $[\mathbf{S}]$ which relates the displacements at the FEM grid to the CFD grid such that

$$\Psi_a = \mathbf{S}\Psi_s \quad (5.22)$$

where Ψ_a and Ψ_s are, respectively, the modal matrix at the CFD grid and at the FEM grid. With the universal spline matrix $[\mathbf{S}]$ at hand, converting Eq (5.21) to a structural-compatible reduced-order aeroelastic model is straightforward. Substituting Eq (5.22) into Eq (5.21) gives:

$$\begin{bmatrix} \mathbf{A}_{R_0} & -\Phi^H \mathbf{B}_0 \mathbf{S} \Psi_s & -\Phi^H \mathbf{B}_1 \mathbf{S} \Psi_s \\ 0 & 0 & \begin{bmatrix} \frac{1}{m_i} \\ \vdots \\ \frac{1}{m_i} \end{bmatrix} \\ -\Psi_s^T \mathbf{S}^T \mathbf{C} \Phi & [\omega_{n_i}^2] & [2\omega_{n_i} \zeta] \end{bmatrix} \begin{Bmatrix} \xi \\ \eta \\ \dot{\eta} \end{Bmatrix} + i\omega \begin{bmatrix} \mathbf{A}_{R_1} & 0 & 0 \\ 0 & \begin{bmatrix} \frac{1}{m_i} \\ \vdots \\ \frac{1}{m_i} \end{bmatrix} & 0 \\ 0 & 0 & \mathbf{I} \end{bmatrix} \begin{Bmatrix} \xi \\ \eta \\ \dot{\eta} \end{Bmatrix} = (5.23)$$

Finally, we arrive at the structural-compatible, modal-based, reduced-order aeroelastic model, Eq (5.23). The size of this model is $K + 2m$, where m is the number of low-order structural modes and is usually on the order of ten for a single wing structure. Eq (5.23) contains two very sparse matrices that can be solved efficiently by a sparse eigenvalue solver.

5.7 Modeling LCO of High Degree-of-Freedom Nonlinear Systems

The nonlinear system that we wish to model can for the most part be modeled as quasi-linear nonlinear vector equations of the form

$$i\omega \mathbf{M}\mathbf{q} + \mathbf{N}\mathbf{q} = 0 \quad (5.24)$$

where \mathbf{q} is a very large matrix arising containing the Fourier coefficients of the unknowns in a harmonic balance analysis, \mathbf{M} is the a constant matrix, and \mathbf{N} is a nonlinear vector operator arising from the harmonic balance analysis. Here \mathbf{q} would contain the unknown flow solution in the three-dimensional harmonic balance of the three-dimensional flow field, and also the structural dynamic modes. Thus, the system may contain hundreds of thousands of degrees of freedom. This system of equations is solved using pseudo-time time marching. Thus, Eq (5.24) is solved by marching the equation

$$\frac{\partial \mathbf{q}}{\partial t} + i\omega \mathbf{M}\mathbf{q} + \mathbf{N}\mathbf{q} = 0 \quad (5.25)$$

in time until a steady state is reached. However, if ω is not known accurately, then Eq (5.25) will not converge, but will itself go into a mathematical limit cycle. One can show, however, that the solution \mathbf{q} will be nearly correct. The solution can be improved by first computed a better estimate for ω using a nonlinear Rayleigh quotient, i.e.

$$\omega \approx \frac{\mathbf{q}^H \mathbf{N}(\mathbf{q})}{\mathbf{q}^H \mathbf{M}^H \mathbf{M}(\mathbf{q})} \quad (5.26)$$

Eq (5.25) can then be marched again to improve the estimate of \mathbf{q} . This process can be repeated until convergence. The result is a description of the LCO behavior of a very high dimensional system, i.e. a nonlinear CFD model coupled to a linear or nonlinear structural model. If Phase II, this technique will be applied to the harmonic balance flow solver coupled to a linear and/or nonlinear structure.

Chapter 6

Development of the Structural/FEM Models and CSD/CFD Grid Interfacing for Candidate Wings for LCO Investigation

Summary

- *In support of the CFD activities for 3D LCO investigation, several wing planforms were selected as candidates for LCO case studies. The selected wing and wing/store candidates were:*
 1. *the MAVRIC-I Business Jet Wing (Fig. 6.1)*
 2. *the ARW-2 Wing (Fig. 6.2)*
 3. *the AGARD Standard 445.6 Wing (Fig. 6.3), and*
 4. *the F-16 Wing and Wing/Store System. (Fig. 6.4)*

All wings under consideration are known to have occurrence of LCO in the lower transonic regime by Wind-Tunnel testing (at TDT of NASA-Langley).

- *The Configurations of these wing planforms are shown below.*
- *One supporting efforts to the follow-on 3D LCO investigations through out the Phase II period is to supply structural/FEM models and to develop CSD/CFD interfacing models. For the selected wing-planform candidates. In what follows, we will show mode shapes due to structural/FEM versus deformed CFD meshes for various wing candidates as a result of these efforts.*
- *The finally selected wing-planform for 3D LCO case studies turned out to the AGARD Standard 445.6 wing and the F-16 wing and wing/store system. Due to the accessibility and availability of their test data, the MAVRIC-I wing and ARW-2 wing were not selected for the preliminary test cases for Phase II. The LCO results of the AGARD 445.6 and the F-16 wing/store system will be presented in the next two chapters.*

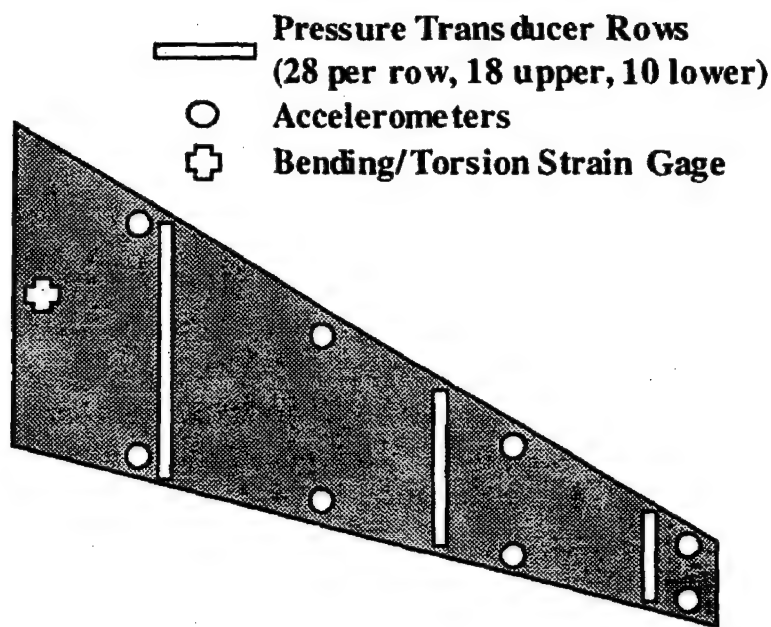


Figure 6.1: Instrumentation Layout for Refurbished MAVRIC-I Business Jet Wing Model

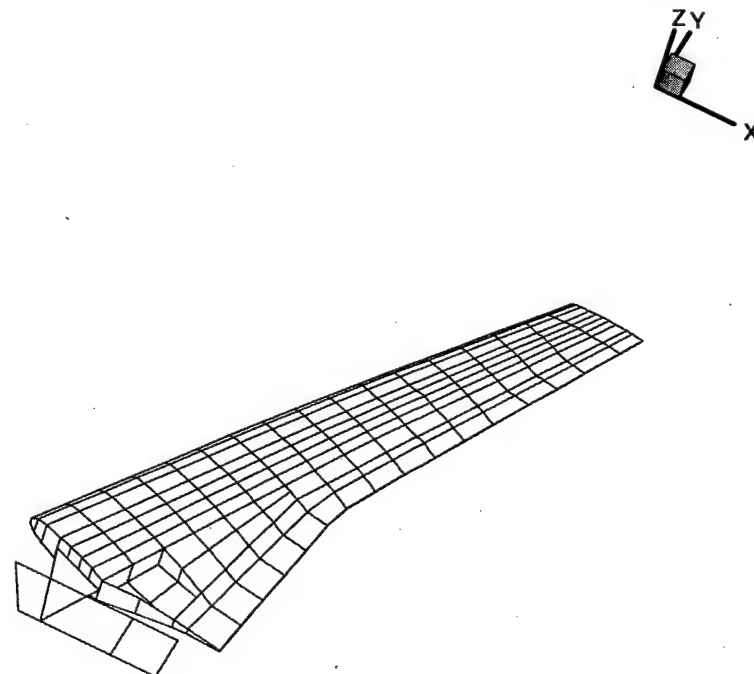


Figure 6.2: MSC NASTRAN FEM of the ARW-2 Wind-Tunnel Model

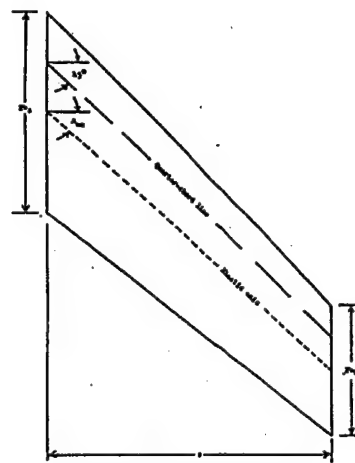


Figure 6.3: AGARD Standard 445.6 wing, Showing Dimensions: $AR = 4.0$, $\lambda = 45$ deg, $\Lambda = 0.6$, NACA 65A004 airfoil section (taken from AGARD Report 765 by Dr. Carson Yates.)

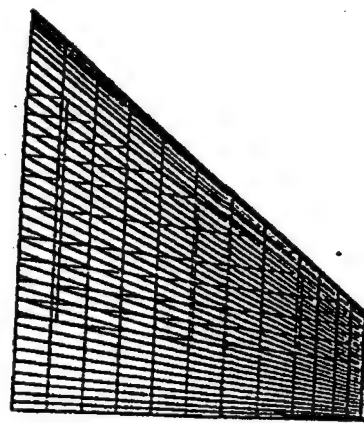


Figure 6.4: Wing Aerodynamic and Structural Model

Mode	Natural Frequencies (Hz)	Generalized Mass (lbf-in/s ²)	Generalized Stiffness (lbf-in)
1	4.083394E+00	1.000000E+00	6.582675E+02
2	1.397037E+01	1.000000E+00	7.705050E+03
3	3.154093E+01	1.000000E+00	3.927433E+04
4	3.199304E+01	1.000000E+00	4.040833E+04
5	5.811350E+01	1.000000E+00	1.333257E+05
6	5.879132E+01	1.000000E+00	1.364540E+05
7	8.823108E+01	1.000000E+00	3.073286E+05
8	9.221439E+01	1.000000E+00	3.357045E+05

Table 6.1: Natural Frequencies, Generalized Masses, and Generalized Stiffness of the MAVRIC-I Business Jet Wing.

6.1 Deforming CFD Meshes of the MAVRIC-I Business Jet Wing

The MAVRIC-I business jet wing is an ongoing wind tunnel test program of the NASA/Langley aeroelasticity branch. The model is constructed with a simple stepped aluminum plate providing the wing stiffness and fitted with end-grain balsa wood to provide the wing contour. Previous experiment has shown that in the 0.8 to 0.9 Mach number range, the model motions were predominantly in the first wing-bending mode and exhibited Limit Cycle Oscillation (LCO).

The model has been retested in the Transonic Dynamic Tunnel (TDT) as the MAVRIC-I. Figure 6.1 indicates the location of instrumentation that has been added to the model. Three chords of unsteady pressure transducers are installed at span stations 0.22, 0.63 and 0.87. Each chord has 28 upper surface and 18 lower surface close-mounted transducers. Eight accelerometers are mounted along the leading and trailing edge of the wing and bending/torsion strain gages are installed at the root. The intent of the retest is to obtain unsteady pressure and wing response data under conditions of LCO in order to validate CFD codes for such conditions.

Figure 6.5 shows a structural finite element model of the MAVRIC-I Business Jet Wing that was provided by the NASA/Langley aeroelasticity branch. This structural finite element model consists of 613 grid points and 551 plate elements whose first 8 natural frequencies, generalized masses, and generalized stiffness are presented in Table 1.

Figure 6.6 presents a surface CFD mesh of the MAVRIC-I business wing that consists of 33x121 grid points. To generate the deformed CFD surface meshes of the 8 structural modes, we employed the "BEM Solver" which was developed by ZONA under a two-year contractual support of NASA/Langley. The BEM solver utilizes the structural boundary element method to generate a universal spline matrix that can transfer the displacement computed

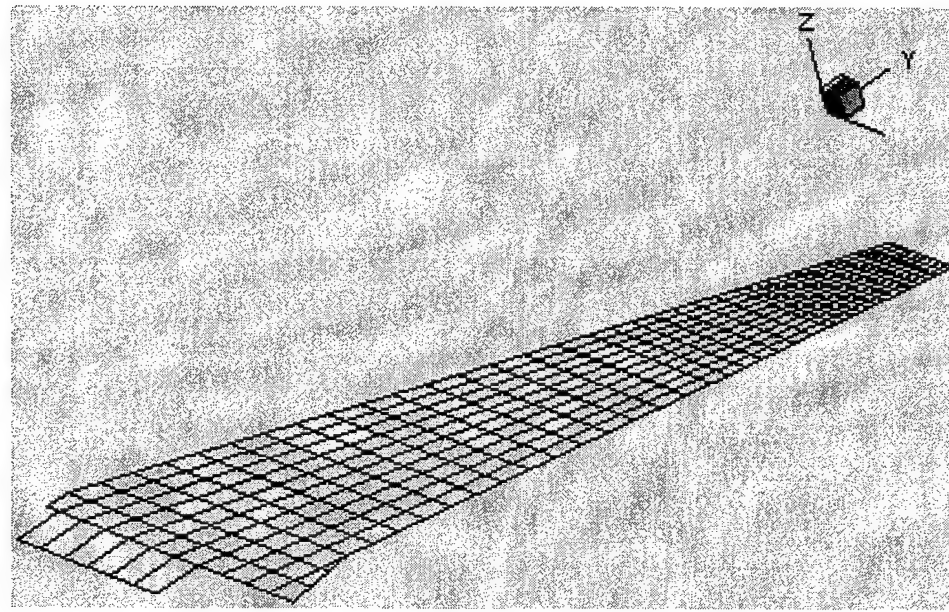


Figure 6.5: Structural Finite Element Model of the MAVRIC-I Business Jet Wing.

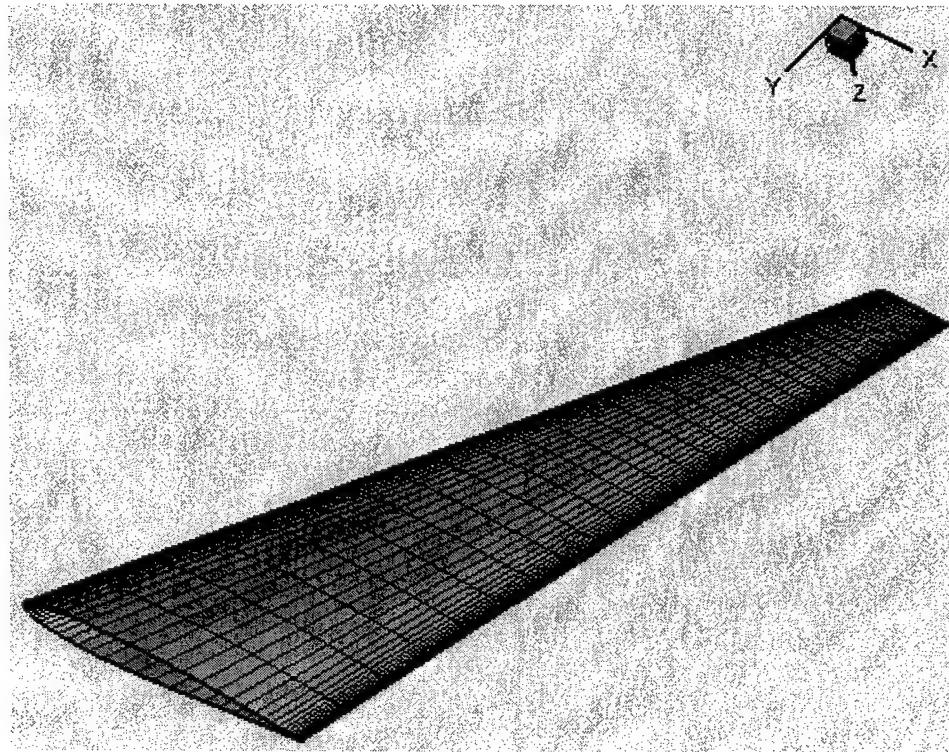


Figure 6.6: CFD Surface Mesh of the MAVRIC-I Business Jet Wing.

Mode	Natural Frequencies (Hz)	Generalized Mass (lbf-in/s ²)	Generalized Stiffness (lbf-in)
1	9.943	1.0	2.49E+03
2	29.85	1.0	3.159E+04
3	32.06	1.0	4.059E+04
4	61.13	1.0	1.475E+05
5	63.82	1.0	1.6079E+05
6	99.16	1.0	3.88E+05
7	105.718	1.0	4.412E+05
8	115.32	1.0	5.251E+05

Table 6.2: Natural Frequencies, Generalized Masses, and Generalized Stiffness of the ARW-2 Wing.

at the structural grid to the CFD grid. These deformed structural FEM models computed by MSC/NASTRAN and 8 deformed CFD meshes computed by the BEM solver are shown in figure 6.7.

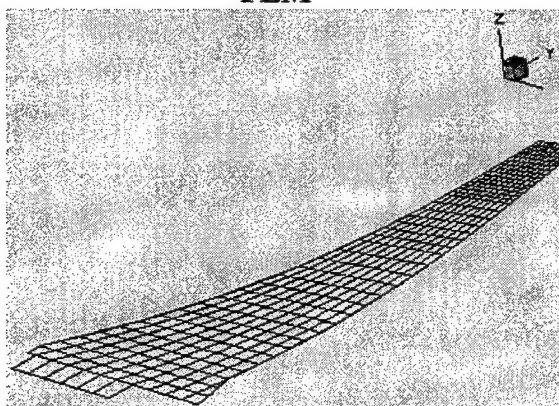
6.2 Deforming CFD Mesh of the ARW-2 Wing

The ARW-2 wing (the second of Aeroelastic research wing) was developed by NASA Langley and tested in the transonic dynamic tunnel (TDT) in the 1980's. The Nastran structural model of the ARW-2 wing is converted from an original spar-based FEM model reported in Ref [96].

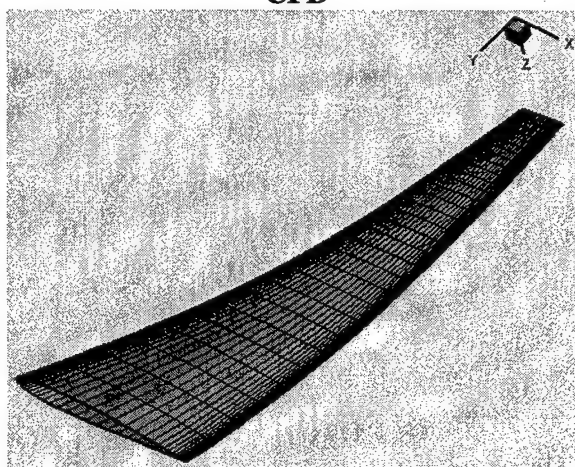
Figure 6.2 presents the Nastran FEM of the ARW-2 wind tunnel model whose natural frequencies, generalized masses, and generalized stiffness are shown in table 6.2.

Shown in Figure 6.8 is the surface CFD mesh of the ARW-2 wing which consists of 153x53 grip points. Similar to the generation of defomed sufrace CFD mesh of the MAVRIC-I wing, the BEM solver is adopted to compute the deformed surface CFD mesh of the ARW-2 wing for the first eight modes. Figure 6.9 depicts the deformed FEM modes computed by MSC.Nastran and the deformed CFD mesh computed by the BEM solver. It can be seen that these two sets of deformed models are very similar. Also, the deformed CFD meshes appear to smooth; showing the robustness of the BEM solver.

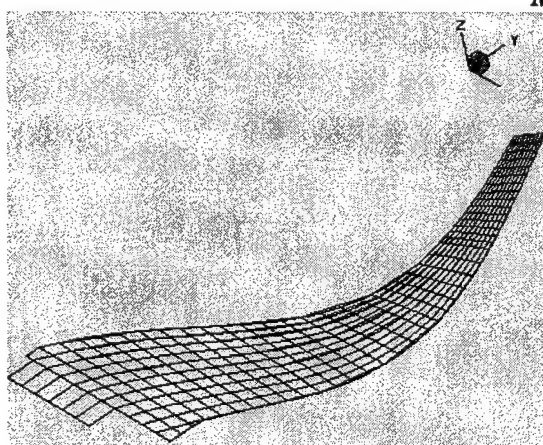
FEM



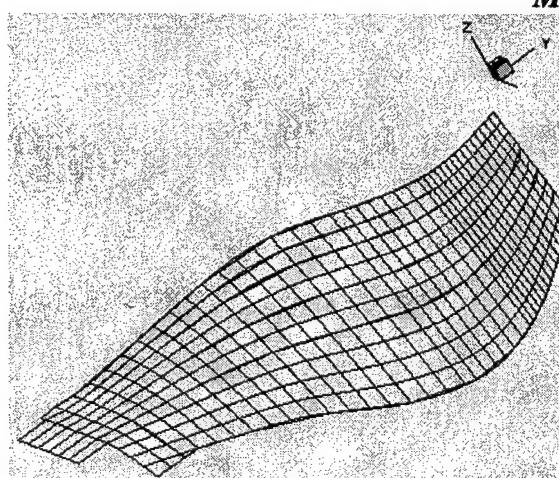
CFD



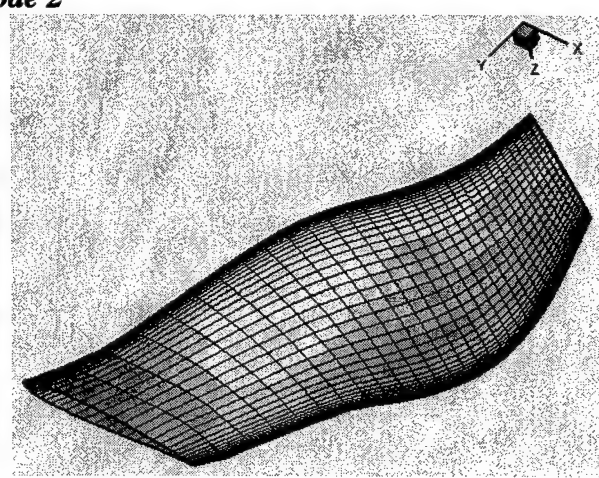
Mode 1

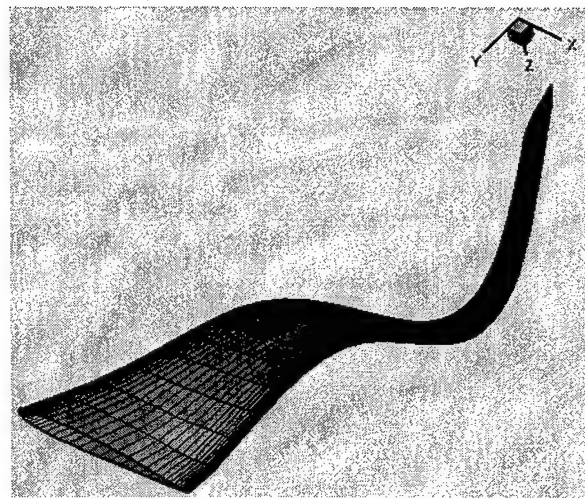
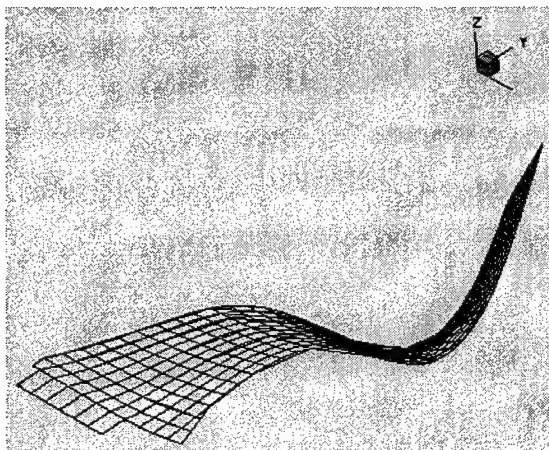


Mode 2

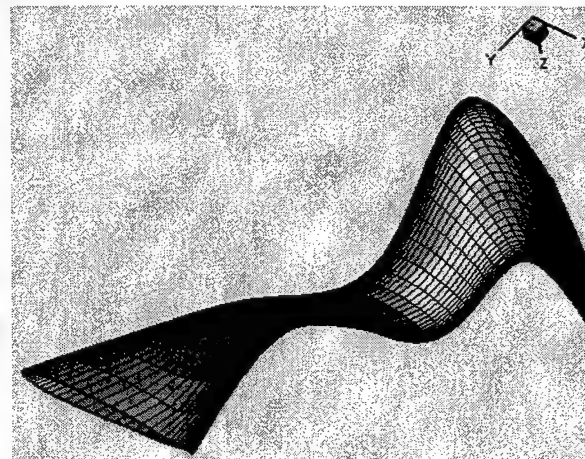
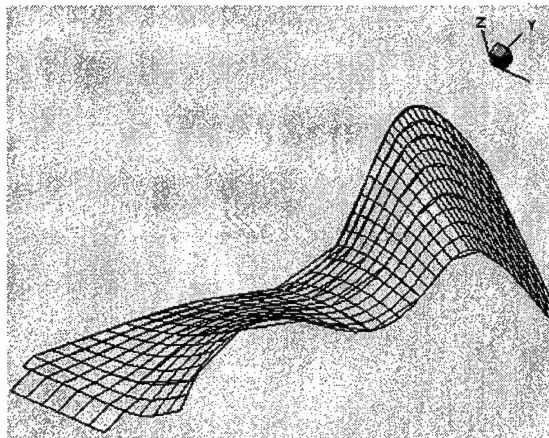


Mode 3

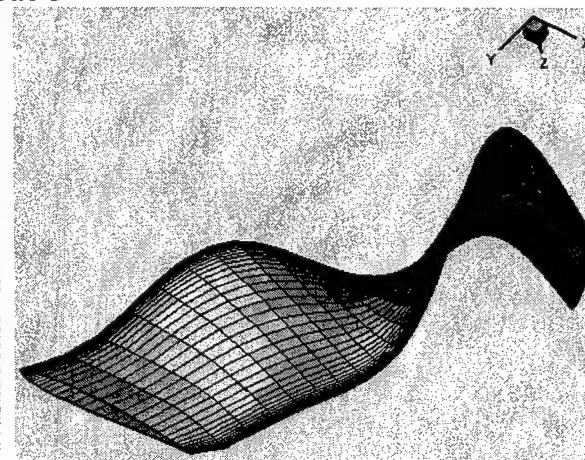
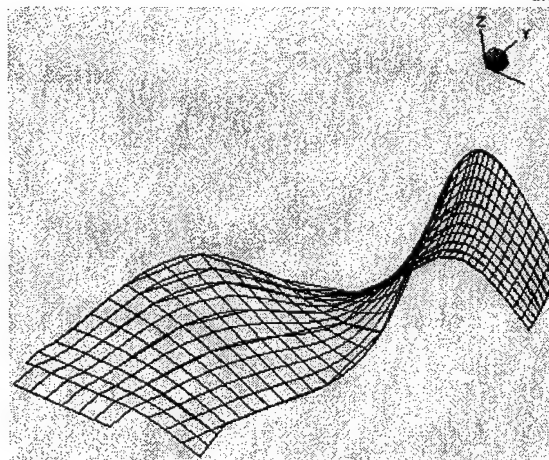




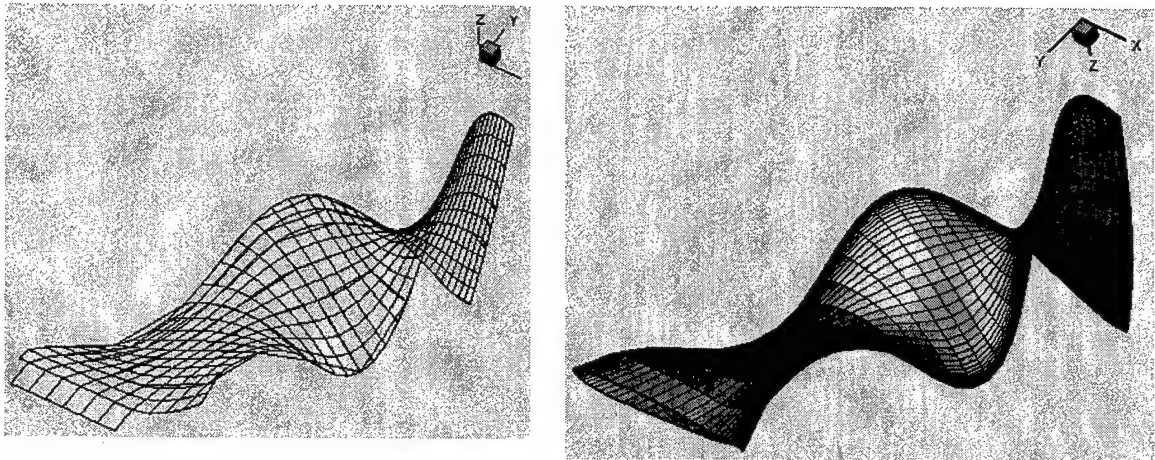
Mode 4



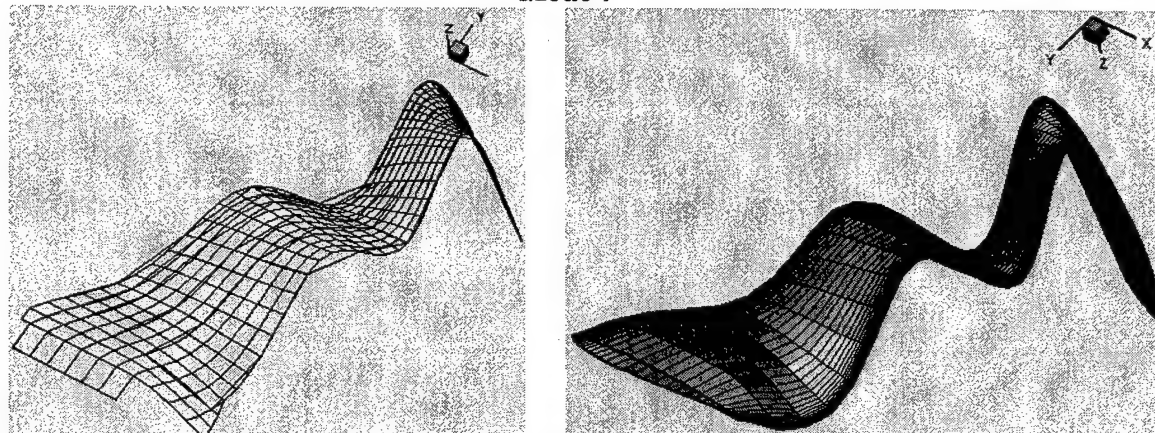
Mode 5



Mode 6



Mode 7



Mode 8

Figure 6.7: Deforming FEM Models and CFD Meshes of the 8 MAVRIC-I Wing Structural Modes.

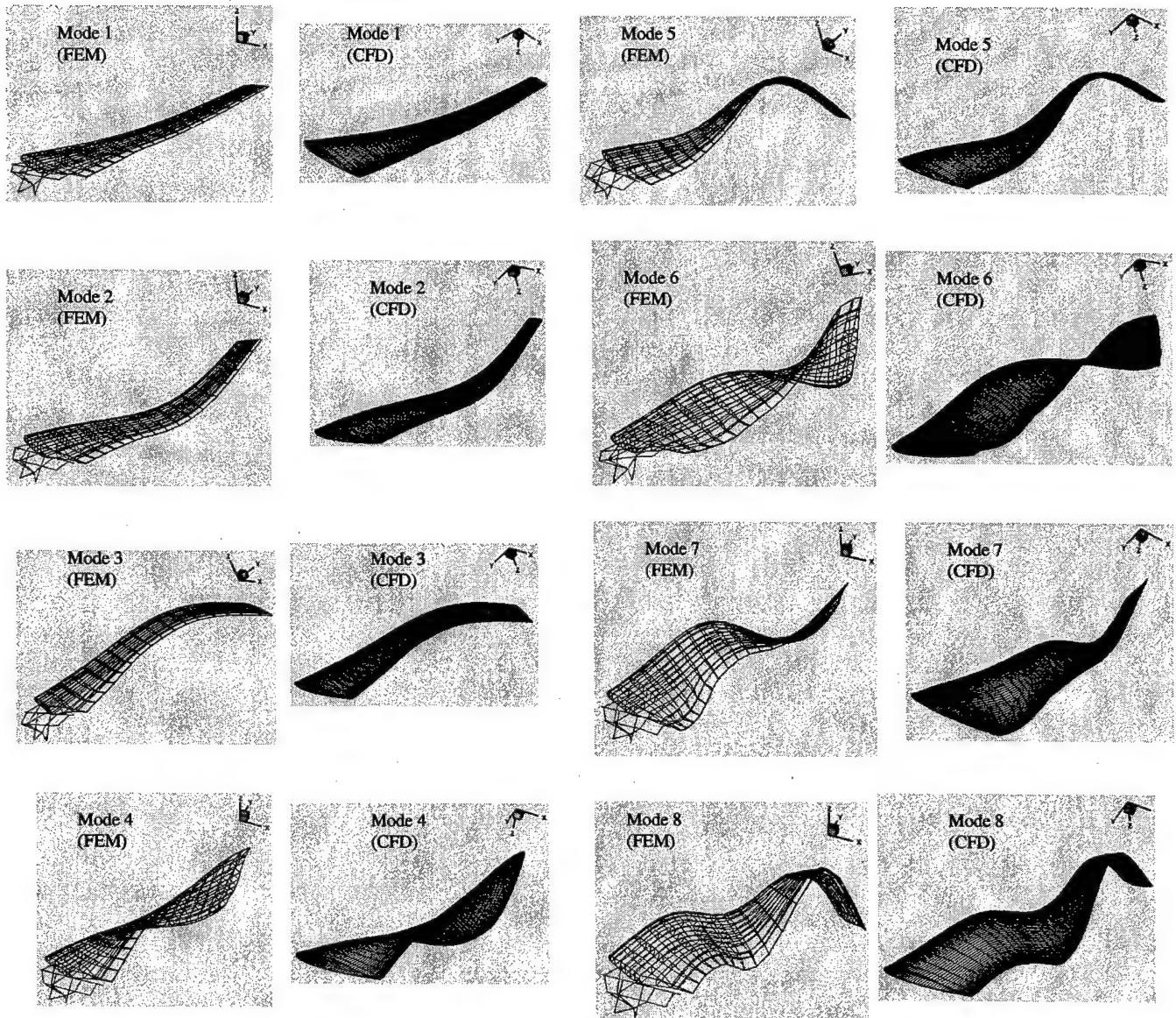


Figure 6.8: Deforming FEM Models and CFD Meshes of the 8 MAVRIC-I Wing Structural Modes.

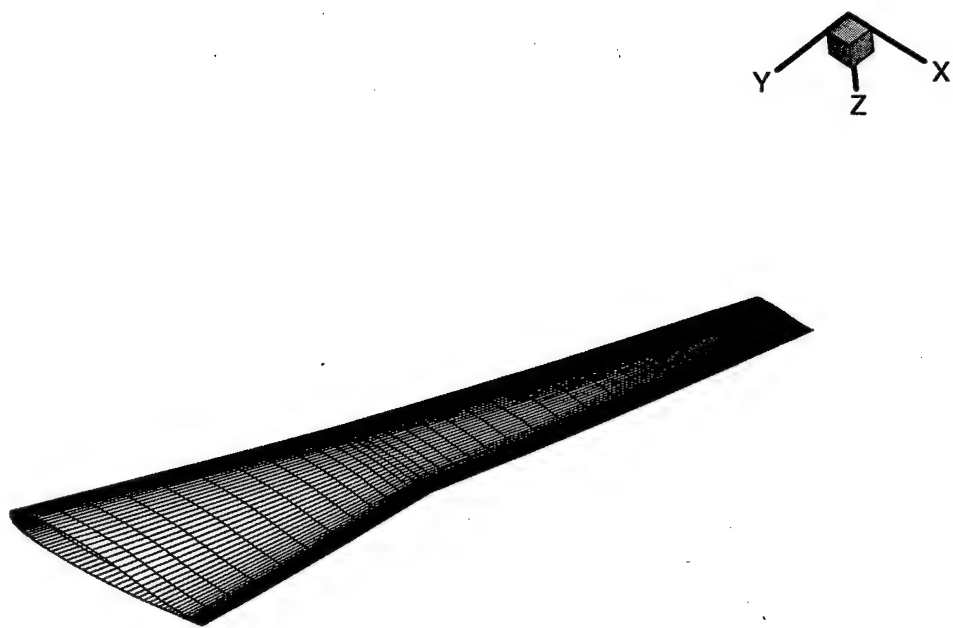


Figure 6.9: CFD Surface Mesh of the ARW-2 Wing

Chapter 7

Duke 3D Wings LCO: AGARD 445.6

Summary

- The inviscid Euler CFD/HB solution method has been extended to three-dimensional flow over a wing. The AGARD 445.6 has been used as an example to demonstrate the capability of the method. To our knowledge these are the first LCO results obtained for this wing by any investigators. Among the principal findings is that over a wide Mach number range there is no stable LCO that would be detectable. Moreover in the low supersonic range an unstable LCO is predicted which suggests that LCO of a large amplitude would be encountered below the predicted flutter boundary. This is an interesting result because previous correlations of experiment and theory have suggested that flutter was observed experimentally at dynamic pressures below the predicted flutter boundary at low supersonic Mach numbers. The unstable LCO predicted at these Mach number may be at least part of the explanation of this difference between experiment and linear flutter theory which has been so perplexing to the aerospace community.
- The complete work in detail can be found in the paper entitled, "A Harmonic Balance Approach to Modeling Three-Dimensional Nonlinear Unsteady Aerodynamics and Aeroelasticity," by J.P. Thomas, E.H. Dowell, and K.C. Hall presented at the ASME International Mechanical Engineering Conference and Exposition, ASME Paper IMECE-2002-32532, November 2002 in New Orleans, LA. Its abstract reads as follows:
Presented is a frequency domain harmonic balance (HB) technique for modeling nonlinear unsteady aerodynamics of three-dimensional transonic inviscid flows about wing configurations. The method can be used to model efficiently nonlinear unsteady aerodynamic forces due to finite amplitude motions of a prescribed unsteady oscillation frequency. When combined with a suitable structural model, aeroelastic (fluid-structure), analyses may be performed at a greatly reduced cost relative to time marching methods to determine the limit cycle oscillations (LCO) that may arise. As a demonstration of the method, nonlinear unsteady aerodynamic response and limit cycle oscillation trends are presented for the AGARD 445.6 wing configuration. Computational results based on the inviscid flow model indicate that the AGARD 445.6 wing configuration exhibits only mildly nonlinear unsteady aerodynamic effects for relatively large amplitude motions. Furthermore, and most likely a consequence of the observed mild nonlinear aerodynamic behavior, the aeroelastic limit cycle oscillation amplitude is predicted to increase rapidly for reduced velocities beyond the flutter boundary. This is consistent

with results from other time-domain calculations. Although not a configuration that exhibits strong LCO characteristics, the AGARD 445.6 wing nonetheless serves as an excellent example for demonstrating the HB/LCO solution procedure.

- *Presented below are two essential conclusive figures showing the HB flutter/LCO solutions due to our inviscid (Euler) model of a 3D AGARD 445.6 wing. The left figure shows that the HB result in flutter boundary throughout the transonic Mach numbers in which it correlates well with test data in the lower transonic Mach number range. The right figure shows that the HB method predicts an unstable LCO in the low supersonic Mach number range, suggesting the LCO of a large amplitude would be encountered below the predicted flutter boundary.*

7.1 Introduction

Recently, Hall et. al. [78] presented a new and computationally efficient harmonic balance (HB) approach for modeling nonlinear periodic unsteady aerodynamics of two-dimensional turbo-machinery configurations. The HB method can be used to model nonlinear unsteady aerodynamic response due to finite amplitude motions, and it is easily implemented within the framework of a conventional iterative CFD method. Subsequently, the present authors [?, 80] devised a computational strategy based on the harmonic balance technique for modeling aeroelastic limit cycle oscillation (LCO) behavior of two-dimensional airfoil configurations.

In the following article, we now extend both the harmonic balance technique for modeling nonlinear unsteady aerodynamics, and the harmonic balance based LCO solution procedure, to three-dimensional inviscid flows about wing configurations. The main challenge in going from two to three-dimensions is that structural models in three-dimensions normally consist of many more degrees-of-freedom (DOF) other than the two “typical” pitch and plunge DOF for two-dimensional airfoil sections.

For two-dimensional flows, it has been observed that a Newton-Raphson root finding technique in conjunction with the harmonic balance method proves to be a very efficient procedure for computing LCO solutions [?, 80]. However for the Newton-Raphson LCO solution procedure, one must compute gradients (or sensitivities) of the nonlinear unsteady aerodynamic loading with respect to each of the structural degrees-of-freedom. For a two-dimensional airfoil section, this requires only two gradient calculations.

For three-dimensional configurations however, this step may have to be carried out for many more structural degrees-of-freedom. One focus of the research presented in this paper has been to determine to what extent one may reduce the computational effort by using a limited number of the possible structural DOF. As will be shown subsequently, using only the structural modes that dominate the flutter onset condition appears to be sufficient to model LCO behavior accurately when using the HB/LCO solution procedure.

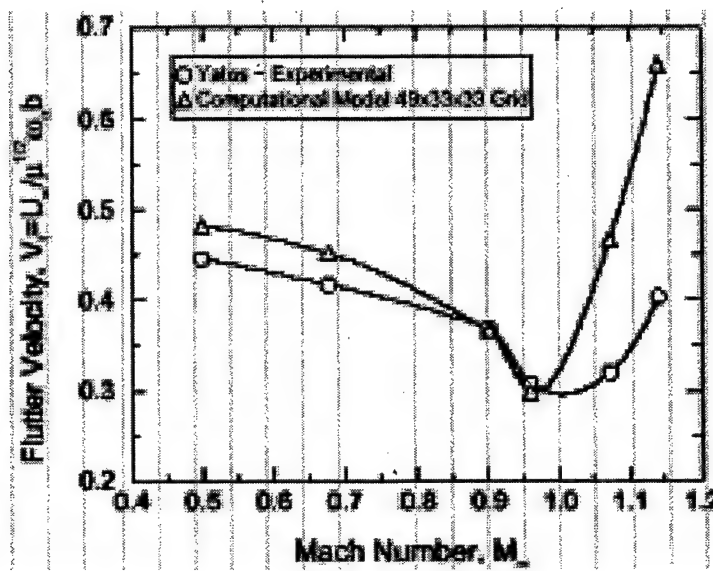


Figure 7.1: Mach Number Flutter Speed Dip Trend for the AGARD 445.6 Wing Configuration

In the following, we demonstrate the harmonic balance technique for modeling nonlinear unsteady aerodynamics, along with the harmonic balance based LCO solution procedure, for the well known AGARD 445.6 transonic wing configuration [?, 82]. We begin by presenting the aeroelastic system of equations applicable to the AGARD 445.6 wing configuration.

7.2 Aeroelastic Model Governing Equations

The governing aeroelastic system of equations for the AGARD 445.6 wing configuration (Fig. 7.3) may be written in the frequency domain as:

$$k_w \mathcal{M} \left(-\bar{\omega}^2 \mu \mathbf{I} + \frac{1}{V^2} \boldsymbol{\Omega} \right) \boldsymbol{\xi} - \mathbf{C}_{\mathcal{Q}}(\boldsymbol{\xi}, \bar{\omega}) = \mathbf{0}. \quad (7.1)$$

For the present analysis, we consider a linear structural model expressed in terms of structural natural modes together with a nonlinear aerodynamic model. Structural damping is neglected. k_w is a constant dependent on the wing shape and overall mass given by

$$k_w = \frac{\pi A_R (1 + \lambda_t) (1 + \lambda_t + \lambda_t^2)}{6 \bar{m}}, \quad (7.2)$$

and $\mathbf{C}_{\mathcal{Q}}$ is the vector of generalized aerodynamic forces, the m^{th} element of which is given by

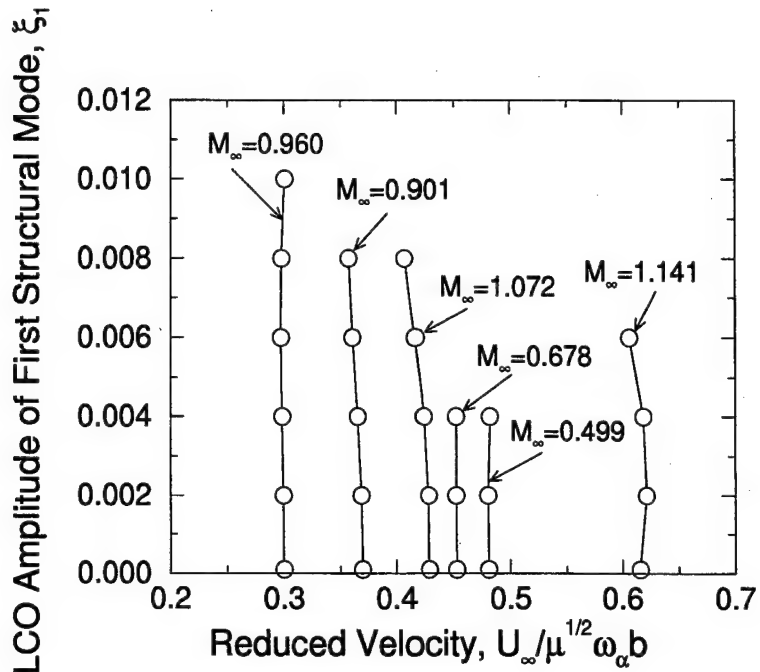


Figure 7.2: Computed AGARD 445.6 Wing Configuration LCO Behavior Trends

$$C_{Q_m} = \frac{1}{q_{\infty} c_r^2} \iint_A \bar{p}_1 \psi_m \cdot \hat{\mathbf{n}} \, dA \quad (7.3)$$

where the integral is evaluated over the surface of the wing.

In addition to the generalized mass matrix \mathbf{M} , wing structural frequency ratio matrix Ω , and mass ratio μ , the governing aeroelastic equations also include the reduced velocity V , reduced frequency $\bar{\omega}$, and structural modal coordinates ξ .

As was done for the aeroelastic LCO model of Ref. [80], one can also include the static aeroelastic equations in the mathematical model. However for the case of the AGARD 445.6 wing configuration, this is not necessary since the configuration consists of a wing based on a constant symmetric airfoil section at zero degree angle-of-attack. As such, no net steady, or static, aerodynamic load acts on the wing.

As will be discussed in the following section, in order to solve the aeroelastic system (Eq. 8.1), one must be able to compute the generalized aerodynamic forces \mathbf{C}_Q for finite values of the structural modal coordinates ξ . This is where the harmonic balance procedure becomes an invaluable tool.

7.3 Harmonic Balance Method

7.3.1 Governing Equations

We consider the inviscid Euler equations (the Reynolds averaged Navier-Stokes equations can be treated in a similar manner), which may be written in integral form as

$$\frac{\partial}{\partial t} \iiint_{V(t)} \mathbf{U} dV + \iint_{A(t)} (\vec{\mathcal{F}} - \mathbf{U} \vec{\mathbf{x}}) \cdot \hat{\mathbf{n}} dA = \mathbf{0} \quad (7.4)$$

where \mathbf{U} is the vector of conservative fluid variables

$$\mathbf{U} = \{\rho \ \rho u \ \rho v \ \rho w \ E_t\}^T \quad (7.5)$$

and

$$\vec{\mathcal{F}} = \mathbf{F} \hat{\mathbf{i}} + \mathbf{G} \hat{\mathbf{j}} + \mathbf{H} \hat{\mathbf{k}} \quad (7.6)$$

where \mathbf{F} , \mathbf{G} , and \mathbf{H} are the x , y , and z direction component flux vectors. i.e.

$$\mathbf{F} = \begin{Bmatrix} \rho u \\ \rho u^2 + p \\ \rho u v \\ \rho u w \\ (E_t + p)u \end{Bmatrix}, \quad \mathbf{G} = \begin{Bmatrix} \rho v \\ \rho u v \\ \rho v^2 + p \\ \rho v w \\ (E_t + p)v \end{Bmatrix}, \quad \mathbf{H} = \begin{Bmatrix} \rho w \\ \rho u w \\ \rho u v \\ \rho v^2 + p \\ (E_t + p)w \end{Bmatrix}.$$

The unsteady motion of the control volume $\vec{\mathbf{x}}$ is given by

$$\vec{\mathbf{x}} = \vec{f} \hat{\mathbf{i}} + \vec{g} \hat{\mathbf{j}} + \vec{h} \hat{\mathbf{k}}, \quad (7.7)$$

and this accounts for the effect of wing surface and grid motion.

7.3.2 Fourier Series Expansion

We consider the unsteadiness of the flow to be strictly periodic in time with period $T = 2\pi/\omega$ where ω is the fundamental unsteady frequency. Thus we can expand Eq. 7.4 in a Fourier series. For example,

$$\iiint_{V(t)} \mathbf{U} dV = \mathbf{Q}(t) \approx \sum_{n=-N_H}^{N_H} \hat{\mathbf{Q}}_n e^{jn\omega t} \quad (7.8)$$

so that

$$\frac{\partial}{\partial t} \iiint_{V(t)} \mathbf{U} dV \approx j\omega \sum_{n=-N_H}^{N_H} n \hat{\mathbf{Q}}_n e^{jn\omega t}, \quad (7.9)$$

and similarly

$$\iint_{A(t)} (\vec{\mathcal{F}} - \mathbf{U} \vec{\mathbf{x}}) \cdot \hat{\mathbf{n}} dA = \mathbf{R}(t) \approx \sum_{n=-N_H}^{N_H} \hat{\mathbf{R}}_n e^{jn\omega t}. \quad (7.10)$$

N_H is the number of harmonics used in the Fourier expansion.

7.3.3 Fourier Coefficients

Substituting the Fourier expansions (Eqs. 7.9 and 7.10) into Eq. 7.4, multiplying by $e^{-jm\omega t}$, and integrating over one period, for each m , i.e.

$$\int_0^T \frac{1}{T} \sum_{n=-N_H}^{N_H} (jn\hat{\mathbf{Q}}_n + \hat{\mathbf{R}}_n) e^{jn\omega t} e^{-jm\omega t} dt \quad (7.11)$$

yields a system of equations for the Fourier coefficients. Namely

$$\mathbf{A} \hat{\mathbf{Q}} + \hat{\mathbf{R}} = \mathbf{0} \quad (7.12)$$

where

$$\mathbf{A} = \begin{bmatrix} -jN_H & & \\ & \ddots & \\ & & jN_H \end{bmatrix}, \hat{\mathbf{Q}} = \begin{Bmatrix} \hat{\mathbf{Q}}_{-N_H} \\ \hat{\mathbf{Q}}_{-N_H+1} \\ \vdots \\ \hat{\mathbf{Q}}_{N_H} \end{Bmatrix}, \hat{\mathbf{R}} = \begin{Bmatrix} \hat{\mathbf{R}}_{-N_H} \\ \hat{\mathbf{R}}_{-N_H+1} \\ \vdots \\ \hat{\mathbf{R}}_{N_H} \end{Bmatrix}.$$

7.3.4 Time Domain Variables

Next, via a Fourier transform matrix \mathbf{E} , one can relate the Fourier coefficient variables $\hat{\mathbf{Q}}$ to time domain solution variables stored at uniformly space sub-time levels within a given period of motion. i.e.,

$$\tilde{\mathbf{Q}} = \mathbf{E} \hat{\mathbf{Q}}, \quad \tilde{\mathbf{R}} = \mathbf{E} \hat{\mathbf{R}} \quad (7.13)$$

where

$$\tilde{\mathbf{Q}} = \begin{Bmatrix} \mathbf{Q}(t_0) \\ \mathbf{Q}(t_1) \\ \vdots \\ \mathbf{Q}(t_{2N_H}) \end{Bmatrix}, \quad \tilde{\mathbf{R}} = \begin{Bmatrix} \mathbf{R}(t_0) \\ \mathbf{R}(t_1) \\ \vdots \\ \mathbf{R}(t_{2N_H}) \end{Bmatrix}, \quad (7.14)$$

and

$$t_n = \frac{2\pi n}{(2N_H + 1)\omega} \quad n = 0, 1, \dots, 2N_H. \quad (7.15)$$

More specifically,

$$\tilde{\mathbf{Q}} = \begin{Bmatrix} \iiint_{V(t_0)} \mathbf{U}(t_0) dV \\ \iiint_{V(t_1)} \mathbf{U}(t_1) dV \\ \vdots \\ \iiint_{V(t_{2N_H})} \mathbf{U}(t_{2N_H}) dV \end{Bmatrix}, \quad (7.16)$$

and

$$\tilde{\mathbf{R}} = \begin{Bmatrix} \iint_{A(t_0)} (\tilde{\mathcal{F}}(t_0) - \mathbf{U}(t_0) \tilde{\mathbf{x}}(\mathbf{t}_0)) \cdot \hat{\mathbf{n}}(t_0) dA \\ \iint_{A(t_1)} (\tilde{\mathcal{F}}(t_1) - \mathbf{U}(t_1) \tilde{\mathbf{x}}(\mathbf{t}_1)) \cdot \hat{\mathbf{n}}(t_1) dA \\ \vdots \\ \iint_{A(t_{2N_H})} (\tilde{\mathcal{F}}(t_{2N_H}) - \mathbf{U}(t_{2N_H}) \tilde{\mathbf{x}}(\mathbf{t}_{2N_H})) \cdot \hat{\mathbf{n}}(t_{2N_H}) dA \end{Bmatrix}. \quad (7.17)$$

Thus

$$\mathbf{A}\mathbf{E}\tilde{\mathbf{Q}} + \mathbf{E}\tilde{\mathbf{R}} = \mathbf{0}, \quad (7.18)$$

and

$$\mathbf{E}^{-1}\mathbf{A}\mathbf{E}\tilde{\mathbf{Q}} + \mathbf{E}^{-1}\mathbf{E}\tilde{\mathbf{R}} = \mathbf{0}. \quad (7.19)$$

So now one can work in terms of the time domain variables, which is in general much easier to do. Note however that we take full advantage of the assumed periodic motion and thus a transient time simulation and its associated computational cost is avoided. The resulting system of equations can then be written as

$$\mathbf{D}\tilde{\mathbf{Q}} + \tilde{\mathbf{R}} = \mathbf{0} \quad (7.20)$$

where

$$\mathbf{D} = \mathbf{E}^{-1}\mathbf{A}\mathbf{E}. \quad (7.21)$$

7.3.5 Pseudo Time Marching

By adding a pseudo time derivative term $\delta\tilde{\mathbf{Q}}/\delta t$ to Eq. 7.20, one can then develop an iterative technique for determining the harmonic balance solution $\tilde{\mathbf{Q}}$. That is,

$$\frac{\delta\tilde{\mathbf{Q}}}{\delta t} + \mathbf{D}\tilde{\mathbf{Q}} + \tilde{\mathbf{R}} = \mathbf{0}, \quad (7.22)$$

whereby one then simply “marches” Eq. 7.22 in a fictitious time-like manner until a steady state (Eq. 7.20) is achieved. Solution acceleration techniques such as local time-stepping, pre-conditioning, residual smoothing, and multi-grid can all be used to accelerate the convergence of the harmonic balance solution.

So for example, in the case of a finite-volume based CFD method, Eq. 7.22 is solved for every computational “finite-volume” comprising the computational mesh. The overall thus consists of pseudo time marching $N \times (2N_H + 1)$ dependent variables where N is the number of mesh points times the number of dependent variables.

Modifying an existing steady CFD flow solver to implement the harmonic balance technique is thus a relatively straight forward task as the main requirement is just a re-dimensioning of the primary arrays from N elements to $N \times (2N_H + 1)$ elements. Again since solution acceleration techniques such as local time-stepping, pre-conditioning, residual smoothing, and multi-grid can be used, the computational cost of the method in determining unsteady solutions thus scales by a factor of $(2N_H + 1)$ times the cost of a nominal steady flow solution.

Once a harmonic balance solution has been determined for a pre-specified wing motion and frequency, one can then obtain the resulting generalized aerodynamic forces from Eq. 8.3.

7.4 Limit Cycle Oscillation Solution Procedure

Based on previous research efforts conducted for two-dimensional airfoil configurations, we have found that a Newton-Raphson technique in conjunction with the harmonic balance nonlinear unsteady flow solver technique provides an efficient method to determine limit cycle oscillation response.

As demonstrated in Refs. [79] and [80], the harmonic balance LCO solution method proceeds by choosing one of the structural modal coordinates to be the independent variable. For the two-dimensional airfoil case, this was chosen to be the pitch coordinate $\bar{\alpha}$. For three-dimensional flow about wings, we now consider ξ_1 , the modal coordinate of the first (typically bending) structural mode shape, as the independent variable. We also chose ξ_1 to be real valued.

In formulating the HB/LCO solution technique, one then proceeds by dividing Eq. 8.1

through by ξ_1 , and re-expressing the system of equations as:

$$\mathbf{R}(\mathbf{L}, \xi_1) = k_w \mathbf{M} \left(-\bar{\omega}^2 \mu \mathbf{I} + \frac{1}{V^2} \boldsymbol{\Omega} \right) \frac{\boldsymbol{\xi}}{\xi_1} - \mathbf{C} \mathbf{Q} \left(\frac{\boldsymbol{\xi}}{\xi_1}, \xi_1, \bar{\omega} \right) = \mathbf{0}. \quad (7.23)$$

Considering both the real and imaginary parts of Eq. 7.23, the vector \mathbf{L} then represents the unknown LCO solution variables

$$\mathbf{L} = \begin{Bmatrix} V \\ \bar{\omega} \\ \text{Re}(\xi_2)/\xi_1 \\ \text{Im}(\xi_2)/\xi_1 \\ \vdots \\ \text{Re}(\xi_M)/\xi_1 \\ \text{Im}(\xi_M)/\xi_1 \end{Bmatrix}, \quad (7.24)$$

which consists of the LCO reduced velocity V (this variable is customarily the independent variable in time-domain LCO solution techniques), LCO reduced frequency $\bar{\omega}$, and the real and imaginary parts of the ratio of each of the LCO structural modal coordinates, for modes two and higher, to the first structural modal coordinate amplitude ξ_1 . The real and imaginary parts of Eq. 7.23 as such represent a system of $2M$ equations for the $2M$ unknown LCO solution variables of \mathbf{L} .

As observed in Refs. [79] and [80], an efficient method for solving Eq. 7.23 is to use a simple Newton-Raphson root finding technique. This is an iterative method for solving for the unknown LCO variables \mathbf{L} whereby one “marches” the vector equation

$$\mathbf{L}^{n+1} = \mathbf{L}^n - \left[\frac{\partial \mathbf{R}(\mathbf{L}^n)}{\partial \mathbf{L}} \right]^{-1} \mathbf{R}(\mathbf{L}^n), \quad (7.25)$$

until a suitable level of convergence is achieved.

We have also observed that one can use simple forward finite-differencing to compute the column vectors of $\partial \mathbf{R}(\mathbf{L})/\partial \mathbf{L}$. That is,

$$\left[\frac{\partial \mathbf{R}(\mathbf{L})}{\partial \mathbf{L}} \right] = \left[\begin{array}{cccc} \frac{\partial \mathbf{R}}{\partial V} & \frac{\partial \mathbf{R}}{\partial \bar{\omega}} & \frac{\partial \mathbf{R}}{\partial \text{Re}(\xi_2)/\xi_1} & \frac{\partial \mathbf{R}}{\partial \text{Im}(\xi_2)/\xi_1} \\ | & | & | & | \\ \text{etc.} & & & & \end{array} \right] \quad (7.26)$$

where for example

$$\frac{\partial \mathbf{R}(\mathbf{L})}{\partial V} \approx \frac{\mathbf{R}(\mathbf{L}, V + \epsilon) - \mathbf{R}(\mathbf{L}, V)}{\epsilon},$$

$$\frac{\partial \mathbf{R}(\mathbf{L})}{\partial \bar{\omega}} \approx \frac{\mathbf{R}(\mathbf{L}, \bar{\omega} + \epsilon) - \mathbf{R}(\mathbf{L}, \bar{\omega})}{\epsilon},$$

etc. for a small ϵ . Determining the column vectors of $\partial \mathbf{R} / \partial \mathbf{L}$ in this manner thus requires numerous computations of $\mathbf{R}(\mathbf{L})$ for various perturbations to \mathbf{L} . This in turn means several computations of the unsteady aerodynamic loading \mathbf{C}_Q for the different perturbations of \mathbf{L} , and this is where the harmonic balance solver comes into play. This is also the most computationally expensive aspect of the LCO solution methodology. However, the overall method does lend itself to a simple computational parallelization strategy as each of the gradient approximations can be calculated on an individual computer processor.

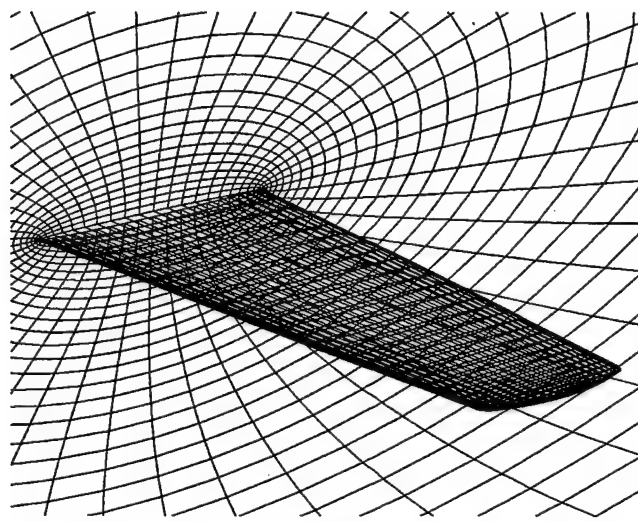
7.4.1 The AGARD 445.6 Transonic Wing Configuration

As noted in the introduction, in order to demonstrate the harmonic balance nonlinear aerodynamic and LCO solution procedures, the the AGARD model 445.6 transonic wing configuration [?, 82] is chosen as an example. This is a 45 degree quarter chord swept wing based on the NACA 64A004 airfoil section, which has an aspect ratio of 3.3 (for the full span), and a taper ratio of 2/3. Figure 7.3 illustrates the computational mesh employed for this configuration with Fig. 7.3a showing a close-up of the wing surface and symmetry boundary grids, and Fig. 7.3b showing the outer boundary grid. The grid, which in this instance is the “medium” resolution mesh, is based on an “O-O” topology that employs 49 (mesh i coordinate) computational nodes about the wing in the stream-wise direction, 33 (mesh j coordinate) nodes normal to the wing, and 33 (mesh k coordinate) nodes along the semi-span. The total number of fluid dynamic DOF for this CFD mesh is thus 266,805 (i.e. $5 \text{dependent flow variables} \times i_{max}(49) \times j_{max}(33) \times k_{max}(33)$). The outer boundary of the grid extends five semi-spans from the mid-chord of the wing at the symmetry plane. The particular structural configuration of the wing under consideration is referred to as the “2.5 ft. weakened model 3” [?, 82].

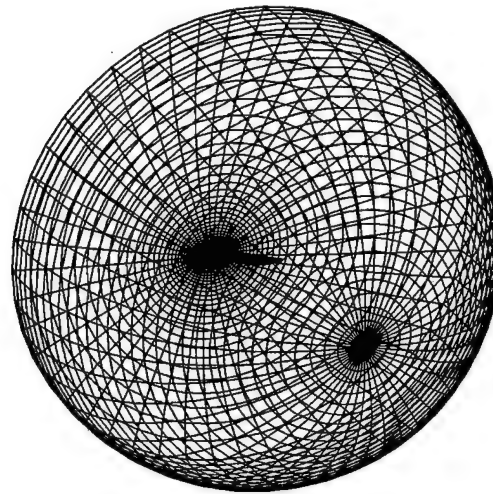
Finally, Fig 7.4 shows the first three computed (via a finite element analysis) structural mode shapes and natural frequencies for the AGARD 445.6 “weakened” wing configuration as presented in [81]. The first mode shape is seen to consist of a first bending type of motion, the second mode shape then being a first twisting type of motion, and finally the third mode being a second bending motion. Two additional mode shapes, second twisting and third bending, are also provided in [81]. These mode shapes have all been mapped to the computational meshes used in this study using a sixth-order multi-dimensional least squares curve fitting technique.

7.4.2 Unsteady Grid Motion Treatment

As noted in section 3.4, for the harmonic balance method, the flow solution variables are stored at $2N_H + 1$ sub-time levels over a period of one cycle of motion. This means that the unsteady deformed shape of the wing is thus required at $2N_H + 1$ sub-time levels over

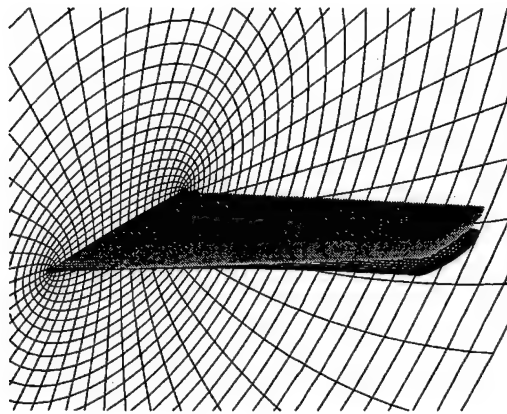


(a) *Wing Surface and Symmetry Plane Grids*

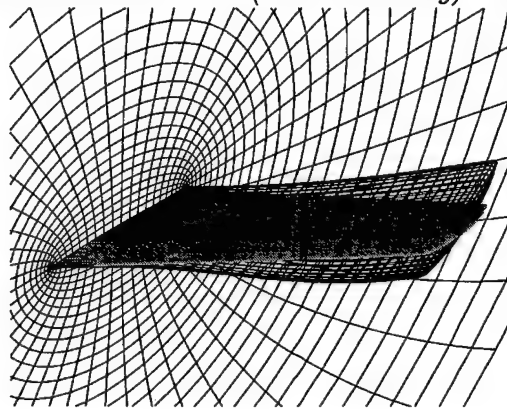


(b) *Far-field Boundary Grids*

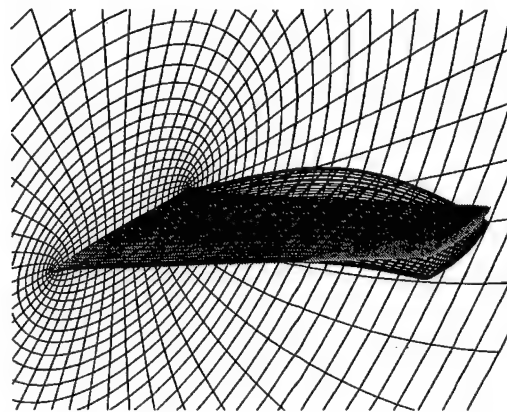
Figure 7.3: Computational Grid Layout for AGARD 445.6 Wing Configuration. 49(i) x 33(j) x 33(k) Grid Shown.



Structural Mode One (First Bending) - 60 hz



Structural Mode Two (First Twisting) - 240 hz



Structural Mode Three (Second Bending) - 304 Hz

Figure 7.4: AGARD 445.6 Wing “Weakened” Structural Configuration Mode Shapes.

the same period of motion. In the following analysis, we consider a linear structural model whereby we approximate the finite-amplitude motions as a superposition of a limited number of the natural mode shapes of the structure. That is,

$$\mathbf{x}_{i,j,k}(t_n) = \mathbf{x}_{0_{i,j,k}} + \phi_{i,k}(j) \operatorname{Re} \left(\sum_{m=1}^M \xi_m \psi_m e^{j\omega t_n} \right) \quad (7.27)$$

where $\mathbf{x}_{0_{i,j,k}}$ is the nominal stationary grid and $\phi_{i,k}(j)$ is a blending function, which is equal to one at the wing surface boundary, and which decays to zero at the outer far-field grid boundary. In this instance, we use the following blending function

$$\phi_{i,k}(j) = 1 - s_{i,k}(j)/s_{i,k}(j_{\max}) \quad (7.28)$$

where $s_{i,k}(j)$ is the distance, in the j^{th} mesh coordinate, along a grid line curve emanating from the $(i, k)^{\text{th}}$ mesh point on the surface of the wing.

This procedure for modeling the finite amplitude wing surface and grid motion is very simple and efficient. However, it can eventually lead to negative volumes when the amplitude of the motion is too great. This is in part due to the “O-O” grid topology, which has the tendency to have a rather highly skewed mesh near the wing tip.

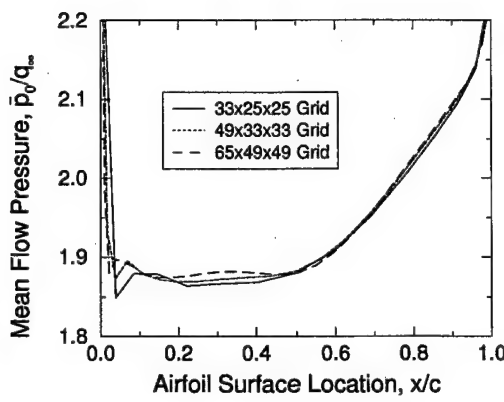
7.5 Nonlinear Unsteady Aerodynamics

We next compute the nonlinear aerodynamic response for a $M_\infty = 0.960$ background steady flow about the AGARD 445.6 wing configuration due to various finite amplitudes of unsteady wing motion. We choose a reduced frequency of $\bar{\omega} = 0.1$ since this is near the reduced frequency at which the wing flutters.

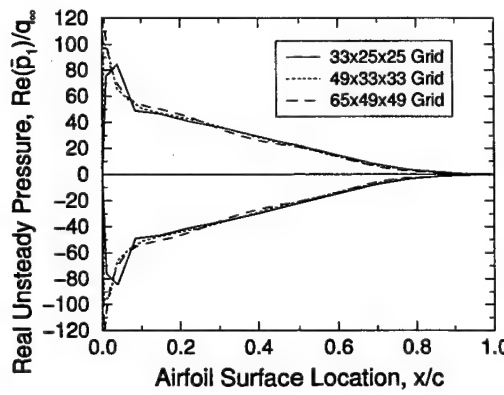
7.5.1 Mesh Convergence

First, we consider the quality of the mesh. To get a sense of required mesh resolution, we consider a small, in effect linear, amplitude motion of the first modal coordinate. i.e. $\xi_1 = 0.0001$ for a reduced frequency $\bar{\omega} = 0.1$. Of course grid resolution is also an important issue for larger amplitude motions. However for larger motion amplitudes, the number of harmonics one uses in the HB method, in addition to the grid resolution, plays a role in overall solution accuracy. As such, a comprehensive study of model resolution becomes quite a bit more involved. For this reason, we have chosen to examine a small amplitude motion. Future grid convergence studies will consider larger amplitude motions and higher harmonics.

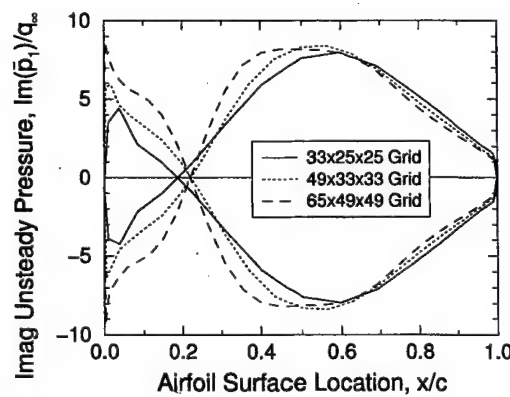
Figure 7.5 shows the computed steady and unsteady flow surface pressure distributions at 70% span for three different grid resolutions. As can be seen, there is not much difference in the solutions amongst the three different grid resolutions. As such, we have chosen to employ



Mean (Zeroth Harmonic) Surface Pressure



Real Unsteady (First Harmonic) Surface Pressure



Imaginary Unsteady (First Harmonic) Surface Pressure

Figure 7.5: Mesh Convergence Characteristics for the AGARD 445.6 Wing Surface Pressure at 70% of Wing Semi-span: $\alpha_0 = 0.0$ (deg), $M_\infty = 0.960$, $\bar{\omega} = 0.1$, and $\xi_1 = 0.0001$.

Structural Mode Shape	ξ_{\max}	$\bar{z}_{1\max}/(b/2)$	$\bar{z}_{1\max}/c_r$
1 - First Bending	0.0120	0.2416	0.3309
2 - First Twisting	0.0025	0.0500	0.0685
2 - Second Bending	0.0030	0.0547	0.0749

Table 7.1: AGARD 445.6 Wing Configuration Maximum Modal Coordinate Amplitudes - 49(i) x 33(j) x 33(k) Grid.

49x33x33 grid for all subsequent calculations. As can be seen, since the AGARD 445.6 wing uses only a 4% thick symmetric airfoil section, the pressure distribution is also symmetric about the upper and lower surfaces, and because the section is so thin, no definitive shock is readily apparent at even this high transonic Mach number.

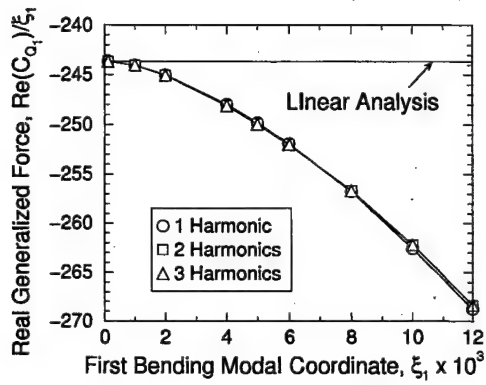
7.5.2 Finite Amplitude Motion Limits

As mentioned in section 4.2, negative computational cell volumes can occur once the amplitude of the wing motion becomes too large. Table 7.1 shows the maximum value for each of the first three structural modal coordinates, when taken separately, at which point negative volume problems start to occur for the 49x33x33 mesh. Also listed is the corresponding maximum unsteady vertical displacement of the wing surface $\bar{z}_{1\max}$ during an interval of motion.

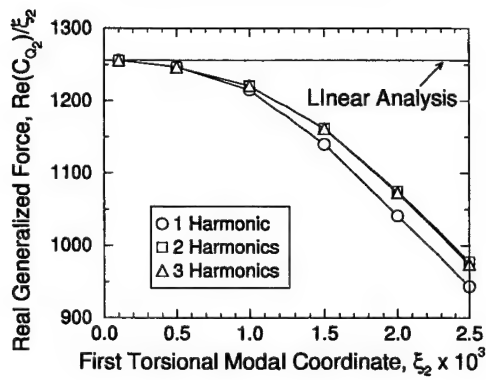
7.5.3 Harmonic Convergence

Next, Figs. 7.6 and 7.7 show computed real and imaginary parts, respectively, of the first three generalized force coefficients (C_{Q_1} , C_{Q_2} , and C_{Q_3}) normalized by the each modal coordinate (ξ_1 , ξ_2 , and ξ_3) as a function of the magnitude of each modal coordinate (ξ_1 , ξ_2 , and ξ_3). Shown are results when using one, two, and three harmonics in the harmonic balance solution procedure. As can be seen, the amplitude of the modal coordinate has an effect on the generalized force, and particularly so for the real part. Also evident is how one should use more harmonics when considering ever increasing modal coordinate amplitudes. However, in this example, the use of only two harmonics can be seen to produce a very high level of harmonic convergence for even the largest modal amplitudes. It has been our experience that two harmonics in many cases are all that are necessary for achieving a good level of accuracy as long as the amplitudes are not too large, say for example, a maximum of five degrees in pitch amplitude for the case of an airfoil section.

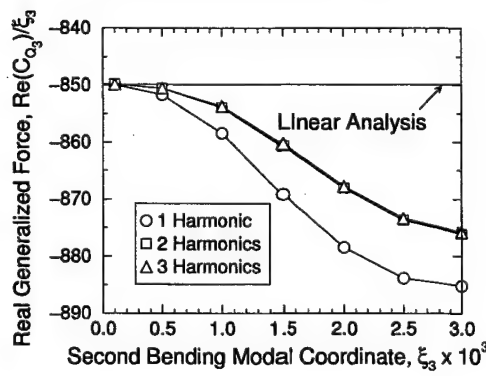
Next, Fig. 7.8 shows surface pressure distributions for the zeroth harmonic (Fig. 7.8a) (i.e. mean flow), along with the real (Fig. 7.8b) and imaginary (Fig. 7.8c) parts of the first harmonic (unsteady flow), again normalized by the modal coordinate amplitude ξ_1 at a location approximately 70% of wing semi-span. In this instance, we consider four different modal coordinate amplitudes ($\xi_1=0.0001, 0.0020, 0.0050, 0.0100$) for the case of three harmonics



Structural Mode One

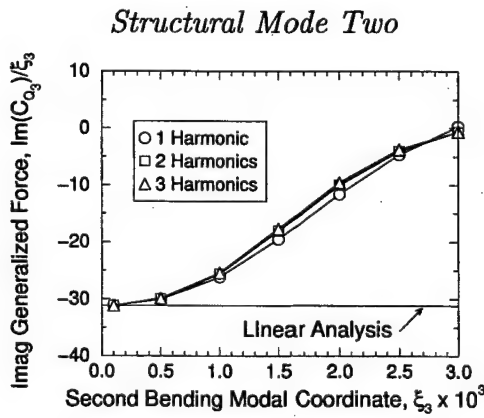
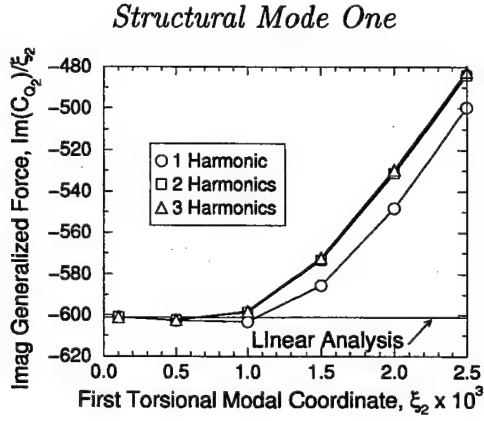
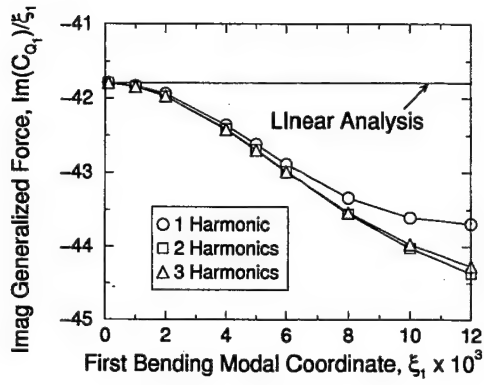


Structural Mode Two



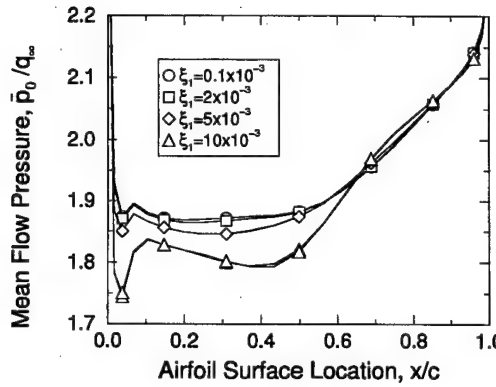
Structural Mode Three

Figure 7.6: Real part of Unsteady Generalized Force as a Function of Mode Shape Amplitude: $\alpha_0 = 0.0$ (deg), $M_\infty = 0.960$, and $\bar{\omega} = 0.1$.

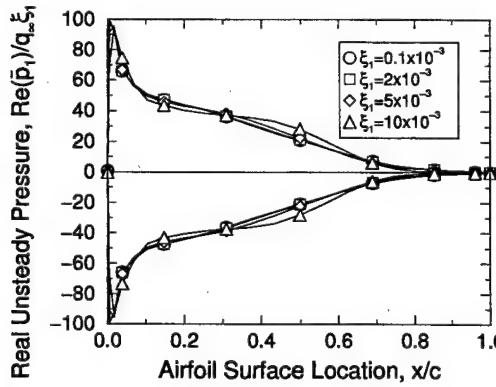


Structural Mode Three

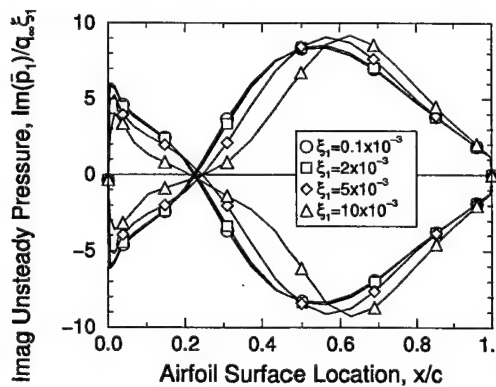
Figure 7.7: Imaginary part of Unsteady Generalized Force as a Function of Mode Shape Amplitude: $\alpha_0 = 0.0$ (deg), $M_\infty = 0.960$, and $\bar{\omega} = 0.1$.



Mean (Zeroth Harmonic) Surface Pressure



Real Unsteady (First Harmonic) Surface Pressure



Imaginary Unsteady (First Harmonic) Surface Pressure

Figure 7.8: Mean and Unsteady Flow Surface Pressure Distribution Dependence on Mode Shape Amplitude: $\alpha_0 = 0.0$ (deg), $M_\infty = 0.960$, $\bar{\omega} = 0.1$, and $N_H = 3$.

used in the harmonic balance technique. Readily apparent are nonlinear effects due to the ever increasing modal coordinate amplitudes. In fact, this is surprisingly so for the zeroth harmonic of the solution (Fig. 7.8a).

Finally, Fig. 7.9 shows normalized zeroth and first harmonic surface pressure distributions for the largest modal coordinate amplitude ($\xi_1=0.0120$) while varying the number of harmonics used in the harmonic balance technique. Two harmonics can be seen to produce good harmonic convergence.

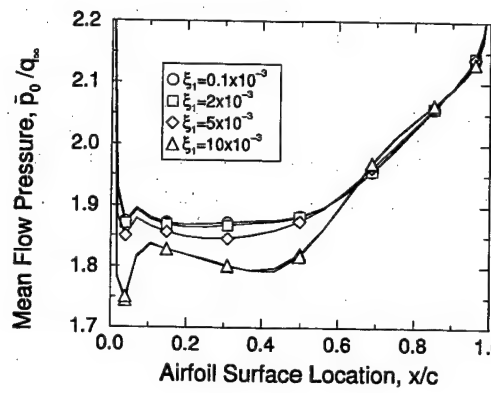
7.6 Nonlinear Unsteady Aeroelasticity

7.6.1 Flutter Onset Trend for the AGARD 445.6 Wing Configuration

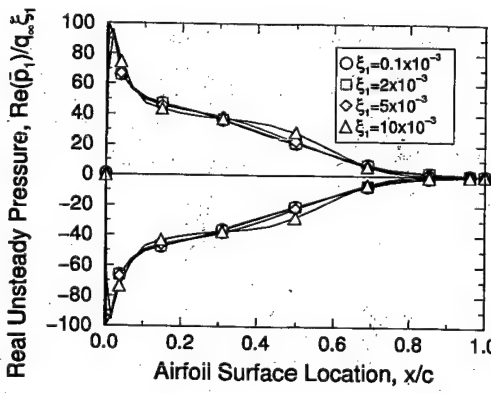
Figure 7.10 shows the computed Mach number flutter onset reduced velocity trend for the AGARD 445.6 wing configuration. Computational model results are shown together with experimental results. The six Mach numbers are the same as those of the experimental investigation of Ref. [82]. The reduction of the flutter onset velocity in the transonic region is readily apparent. The flutter onset conditions are determined using the proper orthogonal decomposition (POD) reduced order model (ROM) time-linearized unsteady aerodynamic approach of Ref. [84]. The POD/ROM approach has been demonstrated to provide a good approximation of the flutter onset conditions, which can then be used as initial conditions for the iterative HB/LCO solution procedure. The agreement between theory and experiment is generally good except at the supersonic free-stream Mach numbers. Other inviscid computational studies by investigators such as Lee-Rausch and Batina [85] and Gordnier and Melville [86] have demonstrated similar differences between theory and experiment for the supersonic Mach numbers.

Table 7.2 shows computed values for the reduced velocity V , reduced frequency $\bar{\omega}$, and the shape of the unsteady motion of the wing at the flutter onset condition, which is presented in terms of the ratio of the amplitude of each of structural modal coordinates normalized to the amplitude of first structural modal coordinate. As can be seen, the first bending structural motion dominates the flutter onset unsteady motion for the six Mach numbers considered, particularly in the transonic region. In fact, beyond the first three structural modes, higher modes only contribute a fraction of a percent to the overall unsteady motion at the flutter onset condition. As will be shown, one can typically neglect these higher numbered modes in the HB/LCO solution procedure.

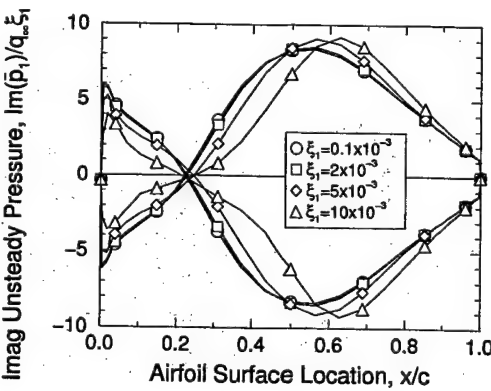
7.6.2 LCO Behavior Trends for the AGARD 445.6 Wing Configuration



Mean (Zeroth Harmonic) Surface Pressure



Real Unsteady (First Harmonic) Surface Pressure



Imaginary Unsteady (First Harmonic) Surface Pressure

Figure 7.8: Mean and Unsteady Flow Surface Pressure Distribution Dependence on Mode Shape Amplitude: $\alpha_0 = 0.0$ (deg), $M_\infty = 0.960$, $\bar{\omega} = 0.1$, and $N_H = 3$.

used in the harmonic balance technique. Readily apparent are nonlinear effects due to the ever increasing modal coordinate amplitudes. In fact, this is surprisingly so for the zeroth harmonic of the solution (Fig. 7.8a).

Finally, Fig. 7.9 shows normalized zeroth and first harmonic surface pressure distributions for the largest modal coordinate amplitude ($\xi_1=0.0120$) while varying the number of harmonics used in the harmonic balance technique. Two harmonics can be seen to produce good harmonic convergence.

7.6 Nonlinear Unsteady Aeroelasticity

7.6.1 Flutter Onset Trend for the AGARD 445.6 Wing Configuration

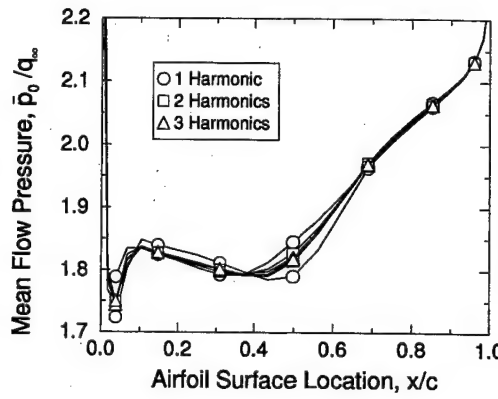
Figure 7.10 shows the computed Mach number flutter onset reduced velocity trend for the AGARD 445.6 wing configuration. Computational model results are shown together with experimental results. The six Mach numbers are the same as those of the experimental investigation of Ref. [82]. The reduction of the flutter onset velocity in the transonic region is readily apparent. The flutter onset conditions are determined using the proper orthogonal decomposition (POD) reduced order model (ROM) time-linearized unsteady aerodynamic approach of Ref. [84]. The POD/ROM approach has been demonstrated to provide a good approximation of the flutter onset conditions, which can then be used as initial conditions for the iterative HB/LCO solution procedure. The agreement between theory and experiment is generally good except at the supersonic free-stream Mach numbers. Other inviscid computational studies by investigators such as Lee-Rausch and Batina [85] and Gordnier and Melville [86] have demonstrated similar differences between theory and experiment for the supersonic Mach numbers.

Table 7.2 shows computed values for the reduced velocity V , reduced frequency $\bar{\omega}$, and the shape of the unsteady motion of the wing at the flutter onset condition, which is presented in terms of the ratio of the amplitude of each of structural modal coordinates normalized to the amplitude of first structural modal coordinate. As can be seen, the first bending structural motion dominates the flutter onset unsteady motion for the six Mach numbers considered, particularly in the transonic region. In fact, beyond the first three structural modes, higher modes only contribute a fraction of a percent to the overall unsteady motion at the flutter onset condition. As will be shown, one can typically neglect these higher numbered modes in the HB/LCO solution procedure.

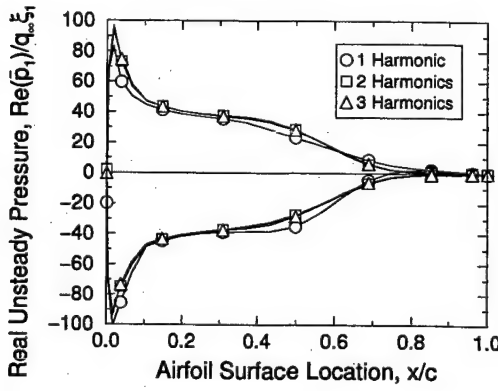
7.6.2 LCO Behavior Trends for the AGARD 445.6 Wing Configuration

	Mach Number, M_∞					
	0.499	0.678	0.901	0.960	1.072	1.141
V	0.479	0.450	0.368	0.300	0.452	0.664
$\bar{\omega}$	0.211	0.141	0.0929	0.0771	0.0664	0.0790
$\text{Re}(\xi_2)/\xi_1$	-0.312	-0.243	-0.115	-0.0635	-0.102	-0.171
$\text{Im}(\xi_2)/\xi_1$	0.115	0.0624	0.0253	0.0137	0.00854	0.0142
$\text{Re}(\xi_3)/\xi_1$	0.0492	0.0360	0.0179	0.0106	0.0348	0.0905
$\text{Im}(\xi_3)/\xi_1$	0.00379	0.00202	0.000389	-0.000558	-0.00246	-0.00591
$\text{Re}(\xi_4)/\xi_1$	-0.00557	-0.00477	-0.00161	-0.000110	0.00707	0.0117
$\text{Im}(\xi_4)/\xi_1$	0.00495	0.00346	0.00203	0.00104	-0.00103	-0.00166
$\text{Re}(\xi_5)/\xi_1$	0.00102	0.00101	0.00117	0.00116	0.000437	-0.00361
$\text{Im}(\xi_5)/\xi_1$	-0.00127	-0.00067	-0.000368	-0.000486	-0.000498	-0.000574

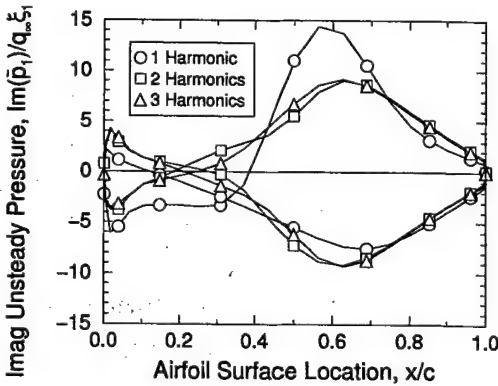
Table 7.2: AGARD 445.6 Wing Configuration Mach Number Flutter Onset Conditions.



Mean (Zeroth Harmonic) Surface Pressure



Real Unsteady (First Harmonic) Surface Pressure



Imaginary Unsteady (First Harmonic) Surface Pressure

Figure 7.9: Mean and Unsteady Flow Surface Pressure Distribution Dependence on Number of Harmonic Used in HB Solver: $\alpha_0 = 0.0$ (deg), $M_\infty = 0.960$, $\bar{\omega} = 0.1$, and $\xi_1 = 0.0120$.

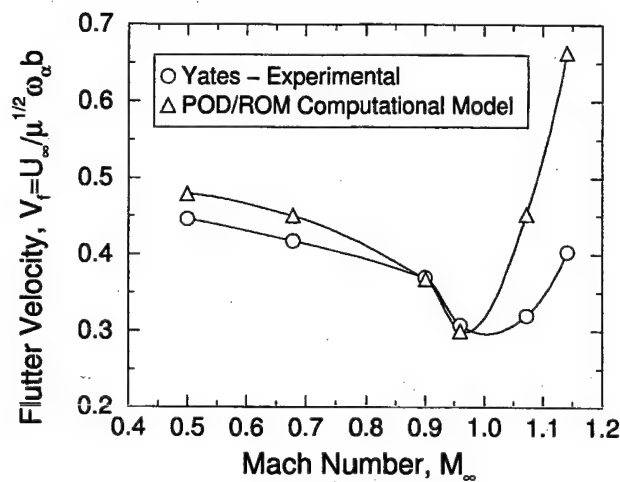


Figure 7.10: Mach Number Flutter Speed Dip Trend for the AGARD 445.6 Wing Configuration

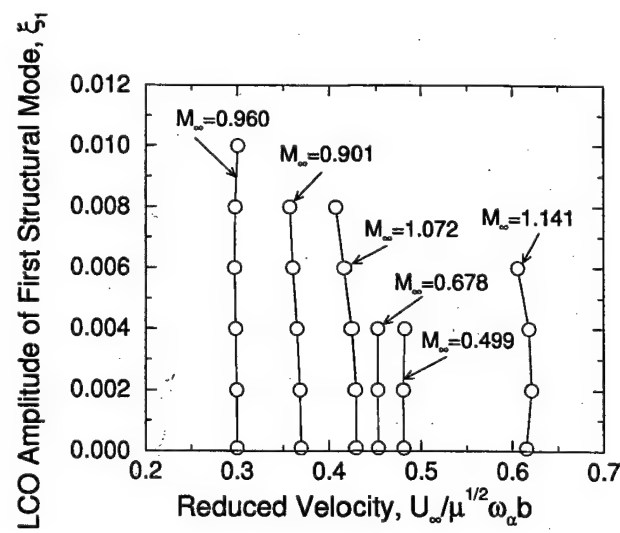


Figure 7.11: Computed AGARD 445.6 Wing Configuration LCO Behavior Trends.

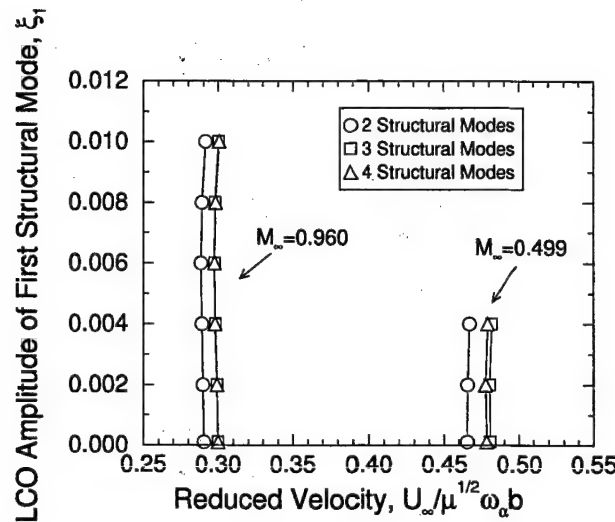


Figure 7.12: Computed AGARD 445.6 Wing Configuration LCO Behavior Trends When Using Different Numbers of Structural Modes in HB/LCO Solutions Procedure.

Based on the LCO solution procedure presented in the Section 4, Fig. 7.11 shows computed LCO behavior trends for the AGARD 445.6 wing configuration for the six different Mach numbers. Unfortunately, Ref. [82] does not provide any specific experimental LCO data. Plotted in Fig. 7.11 is the LCO amplitude of the first structural modal coordinate, ξ_1 , versus the reduced velocity V for each of the six different Mach numbers. The data points for what appear to be zero LCO amplitude actually correspond to a very small LCO amplitude of $\xi_1 = 0.0001$.

In this instance, only the first three structural modes are used for the HB/LCO solution process. The convergence of the HB/LCO solution procedure is also very rapid. Only one or two iterations of Eq. 7.25 are required. The LCO amplitudes in the transonic region go to larger values than those in the subsonic and high supersonic region since the first bending mode shape very much dominates in the transonic region. As such, negative volume problems with the unsteady grid are less of an issue in the transonic region.

Note how the LCO behavior trend curves are nearly vertical. This is indicative of very linear aeroelastic LCO response behavior, which is not all that surprising for this particularly thin wing that has a maximum thickness ratio of 4%. A recent time-domain, and viscous flow, computational study of this same configuration for $M_\infty = 0.960$ and $M_\infty = 1.141$ conducted by Gordnier and Melville [86] also determined that no LCO conditions appear to exist. Note that $\xi_1 = 0.012$ corresponds to an unsteady wing amplitude of approximately one third of the wing root chord (Section 5.2).

Finally, Fig. 7.12 shows computed LCO behavior trends for $M_\infty = 0.499$ and $M_\infty = 0.960$ when using two, three, and four structural mode shapes in the HB/LCO solution procedure.

As can be seen, only the first few structural mode shapes are necessary to produce converged LCO solutions. Again, this is most likely due to the fact that the first bending mode tends to dominate the aeroelastic flutter motion for the AGARD 445.6 wing.

It is interesting to note that the strongest nonlinear LCO behavior occurs for $M_{\infty}=1.072$ and $M_{\infty}=1.141$ as shown in Fig. 7.11. For these Mach numbers, the nonlinear effect is to decrease the reduced velocity at which LCO may occur below the flutter onset condition. This may be at least a partial explanation for the observed differences between theory and experiment in Fig. 7.10. There the calculated (linear) reduced velocity at the onset of flutter is compared to the reduced velocity at which flutter was observed experimentally. As shown in Fig. 7.10, the flutter/LCO observed experimentally does indeed occur at a reduced velocity below that predicted theoretically for the onset of flutter.

7.7 Conclusions

A harmonic balance method for modeling nonlinear periodic unsteady three-dimensional inviscid transonic flows about wing configurations is presented. Demonstrated is the ability of the method to model nonlinear aerodynamic effects due to large amplitude motions for a well known aeroelastic configuration. The use of only two harmonics in the procedure is shown to be quite sufficient for producing harmonic convergence. A limit cycle oscillation solution methodology is also presented and demonstrated for the same benchmark transonic configuration. A weak LCO is observed, which is consistent with results from time-domain calculations by Gordnier and Melville [86]. Nevertheless, it is suggested that nonlinear aerodynamic effects may at least partially explain some of the previously observed differences between experiment and linear aeroelastic theory.

Nomenclature

A_R	= aspect ratio = wing span squared/wing area
b, c	= semi-chord and chord respectively
\mathbf{C}_Q	= vector of non-dimensional generalized forces
E_t	= total energy
f, g, h	= scalar functions defining unsteady grid motion in x , y , and z coordinates, respectively
\mathbf{I}	= identity matrix
j	= $\sqrt{-1}$
\bar{m}	= mass of wing
M_{∞}	= free-stream Mach number
M	= number of structural modes
\mathbf{M}	= generalized mass matrix
N_H	= number of harmonics used in harmonic balance method

\bar{p}_1	= first harmonic unsteady pressure
q_∞	= free-stream dynamic pressure
ρ, ρ_∞	= local and free-stream density, respectively
\mathbf{Q}	= vector of generalized aerodynamic forces
u, v, w	= flow velocity components in x , y , and z coordinate directions, respectively
U_∞	= free-stream velocity
\bar{v}	= volume of a truncated cone having stream-wise root chord as lower base diameter, stream-wise tip chord as upper base diameter, and wing half span as height
V	= reduced velocity or speed index $V = U_\infty / \sqrt{\mu \omega_\alpha b}$
α_0	= airfoil or wing root steady flow angle-of-attack
λ_t	= wing taper ratio $\lambda_t = c_t / c_r$
μ	= mass ratio, $\mu = \bar{m} / \rho_\infty \bar{v}$
ψ_m	= m^{th} structural mode shape
$\omega, \bar{\omega}$	= frequency and reduced frequency $\bar{\omega} = \omega b / U_\infty$
ω_α	= wing first torsional mode natural frequency
Ω	= matrix with structural frequency ratios squared along main diagonal (e.g. $(\omega_1 / \omega_\alpha)^2, \dots, (\omega_M / \omega_\alpha)^2$)
ξ_m, ξ	= m^{th} modal structural coordinate and vector of modal structural coordinates

Subscripts

$0, 1$	= zeroth and first harmonic, respectively
f	= flutter onset (i.e. neutral stability) condition

Chapter 8

3D Wing With Store: F-16 Wing/Store

Summary

- Significant progress has been made in extending out reduced order method (ROM) and harmonic balance (HB) method for computing transonic flutter and limit cycle oscillations (LCO). These novel solution methods provide state of the art accuracy using either an Euler or Navier-Stokes computational fluid dynamics (CFD) model while dramatically decreasing the required computational time and effort. This new capacity has been used to predict the effects of aerodynamics nonlinearities on transonic flutter and LCO of a F-16 wing/store system using the inviscid (Euler) and viscous (RANS) versions of the HB method.
- With reference to the attached results in the following figures: Figure 8.1 shows the geometry of the wing and a portion of the CFD computational grid. Mach number contours for the steady flow about the wing are shown in Figure 8.2. The reduced velocity at which flutter occurs and the eigenmodal participation factors at the flutter condition are shown in Figure 8.3. Finally, in Figure 8.4, the LCO response for the wing tip acceleration measured in g is shown for both the inviscid and viscous flow models. Note that although the reduced velocity at which flutter begins is similar for either flow model, the LCO response is quite different depending on which flow model is used, inviscid or viscous. The results from the viscous model are in better agreement with the LCO response observed in flight tests. These calculations are preliminary quantitative comparisons between the theoretical results and flight test results show good agreement for both the reduced velocity at flutter and the flutter frequency as well as the general level of LCO response.
- More detail is presented in the following section (an extended abstract for AIAA/SDM 2004). For additional details on the Navier-Stokes (RANS) calculations and results for the F-16 wing/store LCO, one is referred to the paper under the same title at the upcoming AIAA/SDM 2004 meeting in Palm Springs.
- Presented is an investigation of modeling of limit cycle oscillation behavior of the F-16 fighter configuration using a frequency-domain harmonic-balance based computational fluid dynamic approach. Strong nonlinear limit cycle behavior is observed in the case

of a viscous flow model as compared to an inviscid flow model. Details of the computational model and plans for the final paper are presented.

8.1 Introduction

The following article reports the latest research efforts in developing and demonstrating the modeling of limit cycle oscillation (LCO) behavior using a frequency domain harmonic balance technique, in this case as applied to a F-16 fighter aircraft configuration.

Denegri [87] has presented experimental data for three different weapon and store configurations of the F-16 aircraft. The LCO behavior was found to be unique for each of these configurations.

A primary purpose of this investigation is to study the possibility of the using the harmonic balance LCO solution method to model some of the various LCO trends that Denegri [87] observed for the limit cycle oscillations of the F-16 wing.

The aerodynamics of the F-16 wing (but not the stores) are modeled by either an Euler or Navier-Stokes based CFD code and the solutions are obtained using the novel Harmonic Balance Method developed at Duke University. The structural model contains the mass and stiffness characteristics of both the wing and the stores.

8.2 Theoretical Details

As demonstrated in Thomas et. al. [88, 89], the governing aeroelastic system of equations for the F-16 wing can be written in the frequency domain as:

$$k_w \mathbf{M} \left(-\bar{\omega}^2 \mu \mathbf{I} + \frac{1}{V^2} \boldsymbol{\Omega} \right) \boldsymbol{\xi} - \mathbf{C}_{\mathbf{Q}}(\boldsymbol{\xi}, \bar{\omega}) = \mathbf{0}. \quad (8.1)$$

In this instance, we consider a linear structural model expressed in terms of structural natural modes together with a nonlinear aerodynamic model. Structural damping is neglected.

k_w is a constant dependent on the wing shape and overall airplane mass given by

$$k_w = \frac{\pi A_R (1 + \lambda_t) (1 + \lambda_t + \lambda_t^2)}{6 \bar{m}}, \quad (8.2)$$

and $\mathbf{C}_{\mathbf{Q}}$ is the vector of generalized aerodynamic forces, the m^{th} element of which is given by

$$C_{Qm} = \frac{1}{q_{\infty} c_r^2} \iint_A \bar{p}_1 \psi_m \cdot \hat{\mathbf{n}} \, dA \quad (8.3)$$

where the integral is evaluated over the surface of the wing.

In order to solve the aeroelastic system (Eq. 8.1), one must be able to compute the generalized aerodynamic forces \mathbf{C}_Q for finite values of the structural modal coordinates ξ . This is done using the harmonic balance solver. Details of the harmonic balance procedure can be found in Hall et. al. [90] and Thomas et. al. [91, 88]

8.3 New Theoretical Details

$$\mathbf{M}(-\omega^2 \mathbf{I} + \Omega^2) \xi - \mathbf{Q} = 0 \quad (8.4)$$

$$\mathbf{M}(-\omega^2 \mathbf{I} + \Omega^2) \xi - \mathbf{Q}(M_\infty, h, \bar{\omega}, \xi) = 0. \quad (8.5)$$

where

$$\mathbf{Q} = \mathbf{Q}(M_\infty, \text{altitude}, \alpha_0, \bar{\omega}, \xi) = \begin{Bmatrix} Q_1 \\ Q_2 \\ \vdots \\ Q_M \end{Bmatrix} \quad (8.6)$$

and

$$Q_m = \iint_A \bar{p}_1 \phi_m \cdot \hat{\mathbf{n}} dA \quad (8.7)$$

or

$$Q_m = \iint_A \bar{p}_1 \phi_m \cdot \vec{\mathbf{n}} dA \quad (8.8)$$

$$Q_m = \iint_A \left[\bar{p}_1 (\vec{\phi}_m \cdot d \vec{A}_0) + \bar{p}_0 (\vec{\phi}_m \cdot d \vec{A}_1) \right] \quad (8.9)$$

8.4 LCO Solution Procedure

As far as the LCO solution procedure, we begin by defining the residual of the aeroelastic system of equations (8.5) as

$$\mathbf{R}(\mathbf{L}) = \mathbf{M}(-\omega^2 \mathbf{I} + \Omega^2) \xi / \xi_1 - \mathbf{Q} / \xi_1 = 0 \quad (8.10)$$

where

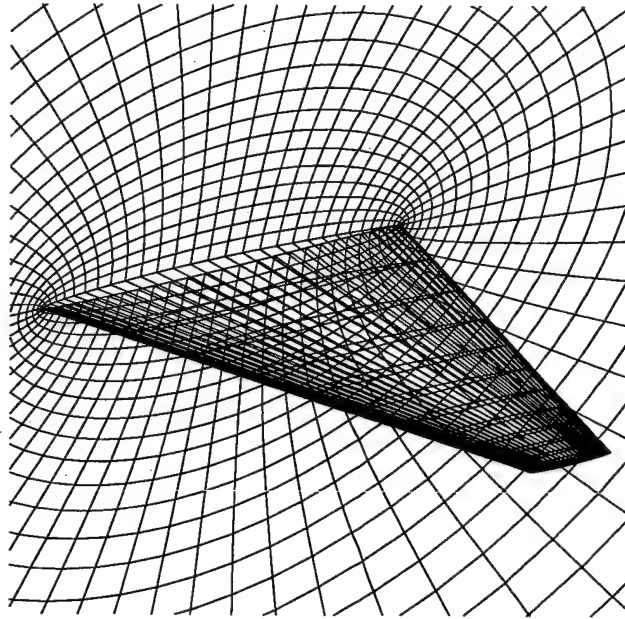


Figure 8.1: F-16 Inviscid Flow Case Computational Grid.

$$\mathbf{L} = \begin{Bmatrix} M_\infty \\ \bar{\alpha}_0 \\ \omega \\ \text{Re}(\xi_2)/\xi_1 \\ \text{Im}(\xi_2)/\xi_1 \\ \vdots \\ \text{Re}(\xi_M)/\xi_1 \\ \text{Im}(\xi_M)/\xi_1 \end{Bmatrix}, \quad (8.11)$$

8.5 Computational Details

For the results presented in this study, the CFD method is a variant of standard Lax-Wendroff scheme [92, 93, 94] in conjunction with the one-equation turbulence model of Spalart and Allmaras [95].

Shown in Fig. 8.1 is the inviscid computational grid near the F-16 wing surface and wing symmetry plane. The mesh uses 65 (mesh i coordinate) computational nodes about the wing in the stream-wise direction, 33 (mesh j coordinate) nodes normal to the wing, 13 (mesh k coordinate) nodes along the semi-span, and 12 more nodes wrapping around the wing tip. The outer boundary of the grid extends five wing semi-spans from the mid-chord of the wing at the symmetry plane. A similar grid is used for the viscous flow model with the difference being that the viscous mesh has mesh points highly clustered near the wing boundary.

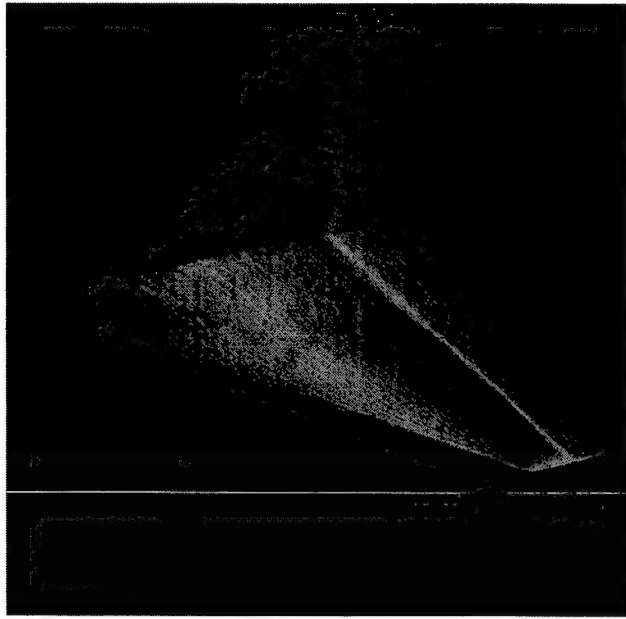


Figure 8.2: F-16 Inviscid Flow Case Computed Mach Contours, $M_{\infty} = 0.9$, $\alpha_0 = 1.5$ deg..

Figure 8.2 shows computed inviscid Mach number contours for a freestream Mach number of $M_{\infty} = 0.9$ and a steady angle-of-attack of $\alpha_0 = 1.5$ degrees.

In the following, we are using the anti-symmetric structural mode shapes. For the aerodynamics, we are modeling only one-half of the wing. As such, we are using symmetric unsteady aerodynamic boundary conditions. So as an initial approximation, we are assuming that the unsteady aerodynamic effects from one side of the overall wing, are small on the other side of the wing. For the final paper, our plans are to model the entire wing in order to properly assess the magnitude of this effect.

8.5.1 F-16 Wing Structural Model

Figure 8.3 shows the computational nodes of the structural model used in the following analysis.

The structural mode shapes correspond to the “Typical LCO” configuration of the F-16 wing. The “Typical LCO” modes shapes are for the case of the F-16 with the following wing stores: Station 1: Empty, Station 2: AIM-9L, Station 3: Air-Surface Missile, Station 4: Wing Tank (Empty). See Denegri [87] for further details.

As mentioned previously, only the anti-symmetric mode shapes have been used in the HB/LCO method. For this initial analysis, the following results are based on using the first two anti-symmetric structural modes.

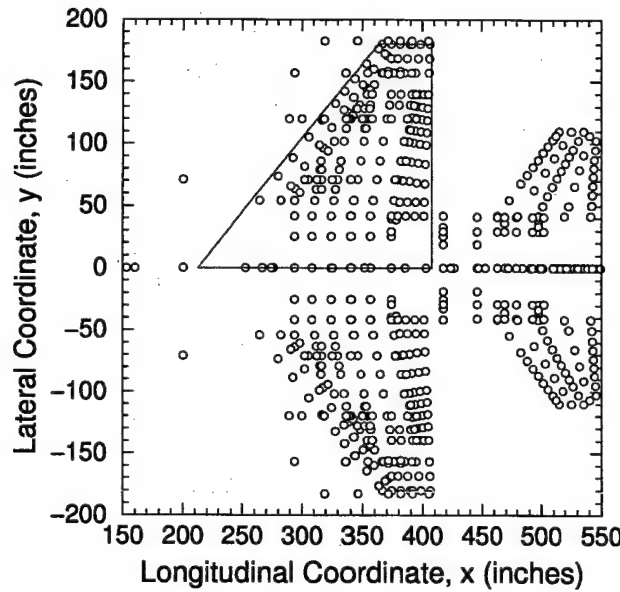


Figure 8.3: F-16 Structural Model Computational Nodes

8.5.2 Limit Cycle Oscillations

Figure 8.4 shows the computed viscous flow model LCO wing tip leading edge acceleration response measured in g's for three difference flight altitudes. The current model does not predict any significant stable or unstable LCO behavior. The nearly vertical line LCO response indicates that as soon as flutter onset Mach number is reached, any further increase in reduced velocity will result immediately in large amplitude unsteady motions. The authors believe there are three possible reasons for the lack of strong LCO behavior being predicted by the HB/LCO model.

First, there could be issues related sufficient mesh resolution. The authors wish to stress that the results shown are preliminary. Mesh refinement studies are currently underway. Previous work by the authors has shown that sufficient mesh resolution is an important aspect of accurate LCO prediction. Second, wing external stores are not being modeled with the current CFD method. Other researchers have suggested that unsteady nonlinear aerodynamic effects brought about by external store may be significant. Third, the structural model used is the present analysis is linear. For the actual F-16 configuration, nonlinear structural effects could play a significant role in overall LCO behavior. All these possibilities for the lack of strong LCO response are currently being investigated.

8.6 Conclusions

The computation of limit cycle oscillation behavior of a F-16 fighter aircraft wing configuration is demonstrated. The limit cycles are computed using a frequency domain harmonic balance technique. Calculations are ongoing. Continuing refinements of the computational

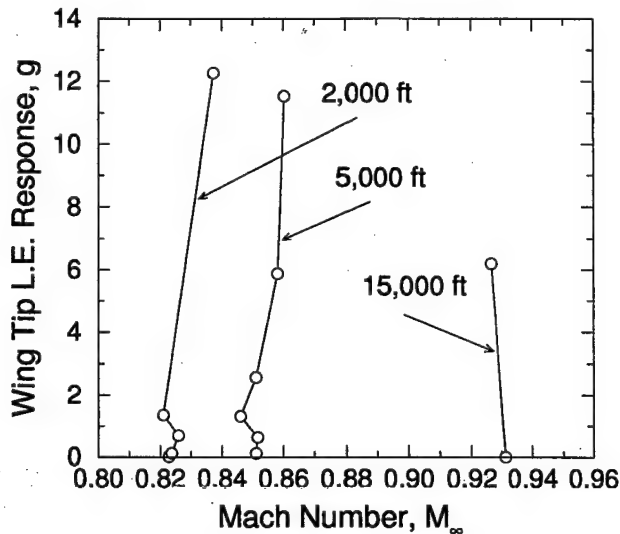


Figure 8.4: Computed F-16 LCO Trends for Three Difference Altitudes Based on Viscous Flow Model. $\alpha_0 = 1.541$ (deg)

model will be reported, in addition to further details of the overall computational methodology.

Nomenclature

- A_R = aspect ratio = wing span squared/wing area
- b, c = wing root semi-chord and chord, respectively
- \mathbf{C}_Q = vector of non-dimensional generalized forces
- \mathbf{I} = identity matrix
- \bar{m} = mass of wing
- M_∞ = free-stream Mach number
- M = number of structural modes
- \mathbf{M} = generalized mass matrix
- \bar{p}_1 = first harmonic unsteady pressure
- \mathbf{Q} = vector of generalized aerodynamic forces
- q_∞ = free-stream dynamic pressure
- Re_∞ = free-stream Reynolds number
- ρ_∞ = free-stream density
- U_∞ = free-stream velocity
- \bar{v} = volume of a truncated cone having stream-wise root chord as lower base diameter, stream-wise tip chord as upper base diameter, and wing half span as height
- V = reduced velocity $V = U_\infty / \sqrt{\mu \omega_\alpha b}$
- α_0 = wing steady (or mean) flow angle-of-attack

λ_t = wing taper ratio $\lambda_t = c_t/c_r$
 μ = mass ratio, $\mu = \bar{m}/\rho_\infty \bar{v}$
 ψ_m = m^{th} structural mode shape
 $\omega, \bar{\omega}$ = frequency and reduced frequency $\bar{\omega} = \omega b/U_\infty$
 Ω = matrix with structural natural frequencies
 along main diagonal (e.g. $\omega_1, \omega_2, \dots, \omega_M$)
 ξ_m, ξ = m^{th} modal structural coordinate and vector
 of modal structural coordinates

Subscripts

r = root
 $0, 1$ = zeroth and first harmonic, respectively

Chapter 9

Commercialization Strategy: Phase II

With a strong technical background, ZONA also has extensive experience in commercialization of its product. In fact, ZONA has been serving the aerospace community through consulting/contractual work and software licensing support since 1986.

ZONA's unsteady/steady aerodynamic software in the aerospace market most notably includes ZONA51 (currently the Aero Option II in MSC/NASTRAN - an industry standard) and the ZAERO software system (covering the entire Mach range). ZONA codes have, thus far, accumulated over 120 users worldwide.

Under an AF/STTR Phase II contract, ZONA and MSC Software are reaching a business agreement to commercialize and jointly market ASTROS* (the seamlessly integrated ZAERO module into ASTROS). ASTROS is a popular Automated Structural Optimization System software among aerospace industry and universities.

9.1 Next Generation Aeroelastic Software

After some 20 years of continuing R&D effort in unsteady transonic aerodynamics, high-level (3-D Euler and Navier-Stokes) unsteady CFD methods remain inadequate to handle the fixed-wing transonic aeroelastic problems encountered in industry. ZONA's recent marketing survey reveals the possible causes of such an inadequacy. These include that: (1) the current CFD methods are computationally very expensive for flutter calculations, (2) the procedures are not easily user-adaptive, (3) Structure engineers prefer to work with solutions in frequency-domain not time-domain. Industry standard methods such as the classical AIC method is lacking in the transonic regime where a reliable high-level CFD method such as CFL3D is badly needed. The proposed frequency-domain POD/ROM method originated by Hall/Dowell has a great potential to be such transonic AIC-like method which has the essence of efficiency, accuracy, modularity and could assess the key physics for nonlinear flutter/LCO. Its future applicability is far reaching which extends to areas in aeroelasticity, aeroacoustics, turbomachinery, ASE, MDO, etc. On the other hand, the ZAERO aeroelastic system exclusively adopts the AIC methodology as basis for the unified unsteady aerodynamics. Although efficient, ZAERO is incapable to provide nonlinear, viscous unsteady aerodynamics with large amplitude oscillations. Once developed, the transonic frequency-domain POD/ROM/HB (Harmonic Balance) methodology along with its Navier-Stokes option, would be an integral part of ZONA's ZAERO aeroelastic system. ZONA envisions that

the production code of the frequency-domain POD/ROM/HB method should become the future industry standard for routine transonic flutter/LCO analysis.

9.2 Commercialization of the Software with ZAERO

As the frequency-domain POD/ROM/HB code is successfully developed, ZONA intends to package the POD/ROM/HB/Navier-Stokes methodology (with either software option) into a well-defined commercial software product. To facilitate its sales, ZONA plans to couple the code with the unified aerodynamic module within ZAERO and jointly market for both codes.

ZONA has currently teamed up with a major FEM software house (MSC Software) for ZONA51 (in MSC/NASTRAN) and ZAERO licensing. ZONA currently supports over 120 users worldwide for the MSC/NASTRAN Aero Option II. Released in April 1999, ZAERO has already had a dozen users including Lockheed Martin/Vought Systems, Boeing/Commercial, DLR/Göttingen, SDRC, NASA/MSFC, NASA/Dryden, Scaled Composites Coleman Aerospace, etc. With ZONA's extensive aerospace contractual/software licensing experience, this software product is expected to break into the aerospace market quite readily. Prospective customers include ZONA's current clientele, other aerospace companies and DoD organization.

As a first license precursor β -sites will be set up with Boeing/St. Louis and Lockheed Martin/Forth Worth to upgrade the code as a viable industry production software.

Other commercialization steps include advertising through magazines, the internet, and attending AIAA conventions. All these are currently being pursued by ZONA for the licensing sales of ZONA codes.

Chapter 10

Conclusion

ZONA Technology, Inc. and Duke University, the ZONA/Duke team, has completed a successful Phase II program entitled "Nonlinear Reduced-Order Modeling of Limit Cycle Oscillations of Aircraft Wings and Wing/Stores". The overarching goal for the Phase II work is to build on the very substantial progress made in Phase I and to develop a capability for a highly computationally efficient and physically accurate mathematical modeling of limit cycle oscillations (LCO) and other nonlinear aeroelastic phenomena. The approach uses the concepts of aerodynamic modes as well as structural modes. Such models provide substantially improved physical understanding and also more accurate prediction of LCO in particular and nonlinear aeroelastic responses in general. This capability may also lead to a rational prediction of buffet onset due to aerodynamically nonlinear oscillations.

The specific objective of the proposed program is to develop the frequency-domain POD/ROM/HB EigenMode method (HB method) and to generalize this method to three-dimensional viscous transonic flow, in order to further the understanding, provide accurate and efficient prediction, and exercise control of LCO/flutter for aircraft wings and wing/stores. In so doing, the high-level Reynolds-average Navier-Stokes (RANS) Equation is solved by the developed HB method framework for computational expediency, while maintaining solution accuracy for LCO/flutter prediction.

The HB method developed is aimed at the capability of handling the following physical effects:

- Three dimensional (3D) as well as 2D flows.
- Nonlinear as well as time linearized aerodynamic pressures and forces.
- Multi-body, e.g., wings plus stores, as well as single body (e.g., wing only) configurations.
- Many as well as few structural modes.
- LCO (nonlinear) as well as flutter (linear) aeroelastic prediction.

Accordingly, the ZONA/Duke team has successfully accomplished the following technical objectives:

- Develop the 2-D N-S version of the above proposed approach.

- Investigate further the initial condition impact on LCO via a 2-D time-domain method (CFL3D/N-S code).
- Extend the geometry capability to 3-D including wing/store configurations.
- Generalize the 2-D/3-D methods to include Harmonic Balance technique for nonlinear LCO analysis.
- Include multiple structural mode analysis capability.
- Perform LCO case studies including wing-alone and F-16 wing/store systems.

Throughout the course of the HB method development, the following conclusions from the tasks (presented in Chapter 2 through Chapter 8) are worth noting:

1. Transonic LCO/flutter solutions using the 2D HB method for inviscid and viscous flows: Frequency-Domain.
 - An extensive parameter analyses of an airfoil aeroelastic configuration (NACA64A010A airfoil) has been achieved using a highly efficient time linearized CFD computational technique. Correlation with experiment remains an open challenge, however a comparison of results from our CFD model with results from an unsteady aerodynamic experiment by Davis and Malcom[37] for lift and moment shows encouraging agreement.
 - An efficient procedure for computing the LCO behavior of aeroelastic airfoil configurations (NLR7301 airfoil) in viscous transonic flows is presented. Viscous effects are demonstrated to be an important factor in determining the behavior of LCO response with respect to reduced velocity. Viscous effects for the NLR 7301 aeroelastic configuration under investigation lead to a much more gradual rate of increase in LCO amplitude with respect to reduced velocity when compared to an inviscid model. The rapid increase in the computed LCO response beyond the flutter point emphasizes the importance of making careful and comprehensive experimental measurements of LCO response over a range of reduced velocities or other parameters as the flutter boundary is exceeded.
2. Transonic LCO/flutter solutions using CFL3D.AE code: Time-Domain
 - A CFD time-marching method, CFL3D v6, is employed to investigate the influences of viscosity, initial airfoil position, and initial perturbation on the amplitudes of the transonic limit cycle oscillations (LCO) of a supercritical airfoil. As expected, stronger aerodynamic nonlinearity leads to smaller LCO amplitudes, even a damped solution while weaker aerodynamic nonlinearity incurs larger LCO amplitudes, even a divergent solution.
 - The computed results due to different methods on the transonic LCO solution for NLR7301 supercritical airfoil at $M = 0.75$ can be summarized by the following figure prepared by Duke University. It is seen that the DLR measured LCO

amplitude (Schewe) is only a fraction of the computed results including that of ZONA (Tang et al), Naval Postgraduate School (Weber et al) and Duke University (Hall and Dowell, Hollow Symbols).

- It is clear that the HB method is superior to the time-domain methods such as CFL3D in terms of computational efficiency and the ease of LCO/flutter solution identification.

3. Transonic LCO/flutter solutions for 3D wings and wing/store systems using the HB method: Frequency-Domain

- A harmonic balance method for modeling nonlinear periodic unsteady three-dimensional inviscid transonic flows about wing configurations (AGARD 445.6 wing) is presented. Demonstrated is the ability of the method to model nonlinear aerodynamic effects due to large amplitude motions for a well known aeroelastic configuration. The use of only two harmonics in the procedure is shown to be quite sufficient for producing harmonic convergence. A limit cycle oscillation solution methodology is also presented and demonstrated for the same benchmark transonic configuration. A weak LCO is observed, which is consistent with results from time-domain calculations by Gordnier and Melville [86]. Nevertheless, it is suggested that nonlinear aerodynamic effects may at least partially explain some of the previously observed differences between experiment and linear aeroelastic theory.
- Significant progress has been made in extending out reduced order method (ROM) and harmonic balance (HB) method for computing transonic flutter and limit cycle oscillations(LCO). These novel solution methods provide state of the art accuracy using either an Euler or Navier-Stokes computational fluid dynamics (CFD) model while dramatically decreasing the required computational time and effort. This new capacity has been used to predict the effects of aerodynamics nonlinearities on transonic flutter and LCO of a F-16 wing/store system using the inviscid (Euler) and viscous (RANS) versions of the HB method.

Finally, this Phase II final report intends to provide a comprehensive description of our approach and results obtained in achieving the Phase II technical objectives. These achievements provide a sound foundation upon which the Phase III effort for technology transfer for a production-ready LCO prediction software can be carried out thus rendering viable commercialization.

References

- [1] Denegri, C.M., "Limit Cycle Oscillation Flight Test Results of a Fighter with External Stores," AIAA-2000-1394.
- [2] Norton, W.J., "Limit Cycle Oscillation and Flight Flutter Testing," Proceedings of the Society of Flight Test Engineers 21st Annual Symposium, Aug. 1990.
- [3] Redd, L.T., "Flutter and Aerodynamic Flight Testing at the Air Force Flight Test Center," Aerospace Flutter and Dynamics Council, Edwards Air Force Base, CA, May 12-14, 1993.
- [4] Brignac, W.J., "Limit Cycle Oscillation F-16 Experience," presented at Flutter and Dynamics Council, Dallas, TX, May 10-11, 1989.
- [5] Schuster, D.M., Edwards, J.W. and Bennett, R.M., "An Overview of Unsteady Pressure Measurements in the Transonic Dynamics Tunnel," AIAA 2000-1770, AIAA Dynamics Specialists Conference, Atlanta, GA, Apr. 5-6, 2000.
- [6] Gibbons, M.D., "Aeroelastic Calculations Using CFD for a Typical Business Jet Model," NASA Contractor Report 4753, Sep. 1996.
- [7] Chen, P.C., Sarhaddi, D. and Liu, D.D., "Limit Cycle Oscillation Studies of a Fighter with External Stores," 39th Structures, Structural Dynamics and Materials Conference, AIAA-98-1727, Apr. 1998.
- [8] Cunningham Jr., A.M. and Meijer, J.J., "Semi-Empirical Unsteady Aerodynamics for Modeling Aircraft Limit Cycle Oscillations and Other Nonlinear Aeroelastic Problems," International Forum on Aeroelasticity and Structural Dynamics, Manchester, U.K., Jun. 26-28, 1995.
- [9] Edwards, J.W., "Transonic Shock Oscillations and Wing Flutter Calculated with an Interactive Boundary Layer Coupling Method," Euromech-Colloquium 349 Simulation of Fluid-Structure Interaction in Aeronautics, Göttingen, Germany, Sep. 16-18, 1996.
- [10] Krist, S.L., Biedron, R.T. and Rumsey, C.L., "CFL3D User's Manual Version 5.0," NASA Langley Research Center, Hampton, VA, Sep. 1997.
- [11] Hall, K.E., Thomas, J.P. and Dowell, E.H., "Reduced-Order Modeling of Unsteady Small Disturbance Flows Using a Frequency-Domain Proper Orthogonal Decomposition Technique," 37th Aerospace Sciences Meeting and Exhibit, AIAA 99-0655, Jan. 1999.

- [12] Bendiksen, O.O., "Role of Shock Dynamics in Transonic Flutter," AIAA-92-2121-CP, 1992.
- [13] Sheta, E.F. and Harrand, V.J., "Computational and Experimental Investigation of Limit Cycle Oscillations in Nonlinear Aeroelastic Systems," AIAA 2000-1399, 41st AIAA/ASME/ASCE/AHS/ASC Structures, Structural Dynamics & Materials Conference, Atlanta, GA, Apr. 3-6, 2000.
- [14] Dowell, E.H., Thomas, J.P. and Hall, K.C., "Transonic Limit Cycle Oscillation Analysis Using Reduced Order Modal Aerodynamic Models," extended abstract for 42nd AIAA/ASME/ASCE/AHS/ASC Structures and SDM Conference, Seattle, WA, Apr. 16-19, 2001.
- [15] Thomas, J.P., Dowell, E.H. and Hall, K.C., "Nonlinear Inviscid Aerodynamic Effects on Transonic Divergence, Flutter and Limit Cycle Oscillations," extended abstract for 42nd AIAA/ASME/ASCE/AHS/ASC Structures and SDM Conference, Seattle, WA, Apr. 16-19, 2001.
- [16] Thomas, J.P., Dowell, E.H. and Hall, K.C., "Three-Dimensional Transonic Aeroelasticity Using Proper Orthogonal Decomposition Based Reduced Order Models," extended abstract for 42nd AIAA/ASME/ASCE/AHS/ASC Structures and SDM Conference, Seattle, WA, Apr. 16-19, 2001.
- [17] Batina, J.T., "Unsteady Transonic Small-Disturbance Theory Including Entropy and Vorticity Effects," Journal of Aircraft, Vol. 26, No. 6, June 1989, p. 531.
- [18] Silva, W.A., "Application of Nonlinear Systems Theory to Transonic Unsteady Aerodynamic Responses," Journal of Aircraft, Vol. 30, No. 5, Sept.-Oct. 1993, pp. 660-668.
- [19] Mignolet, M.P., Liu, D.D. and Chen, P.C., "On the Nonlinear Structural Damping Mechanism of the Wing/Store Limit Cycle Oscillation," AIAA-99-1459, 1999.
- [20] Nam, C., Chen, P.C., Liu, D.D., Yurkovich, R.M. and Urnes, J., "Adaptive Reconfigurable Control Based on a Reduced-Order System Identification for Flutter and Aeroelastic Instability Suppression," SBIR Phase I Final Report for Naval Air Warfare Center Aircraft Division, NAWC-TR-99, Jun. 2000.
- [21] Chen, P.C. and Jadic, I., "Interfacing of Fluid and Structural Models via an Innovative Structural Boundary Element Method," AIAA Journal, Vol. 36, No. 2, Feb. 1998, pp. 282-287.
- [22] Chen, P.C. and Hill, L.R., "A Three-Dimensional Boundary Element Method for CFD/CSD Grid Interfacing," AIAA 99-1213, 1999.
- [23] Dowell, E. H. and Hall, K. C. "Modeling of Fluid-Structure Interaction," *Annual Reviews of Fluid Mechanics*, No. 33, 2000, pp. 445-490

- [24] Vepa, R., "On the Use of Padé Approximates to Represent Unsteady Aerodynamic Loads for Arbitrarily Small Motions of Wings," *AIAA Paper 76-17*, Jan. 1976.
- [25] Karpel, M., "Design for Active Flutter Suppression and Gust Alleviation Using State-Space Aeroelastic Modeling," *Journal of Aircraft*, Vol. 19, No. 3, 1982, pp. 221-227.
- [26] Raveh, D. E., Levy, Y., and Karpel, M. "Aircraft Aeroelastic Analysis and Design Using CFD-Based Unsteady Loads," In *41st Structures, Structural Dynamics, and Materials Conference and Exhibit*, Atlanta, GA, April 2000. AIAA-00-1325.
- [27] Hall, K. C., Thomas, J. P., Clark, W. S., "Computation of Unsteady Nonlinear Flows in Cascades Using a Harmonic Balance Technique", *AIAA Journal*, Vol. 40, No. 5, 2002, pp. 879-886.
- [28] Thomas, J. P., Dowell, E. H., Hall, K. C., "Nonlinear Inviscid Aerodynamic Effects on Transonic Divergence, Flutter and Limit Cycle Oscillations", *AIAA Journal*, Vol. 40, No. 4, 2002, pp. 638-646.
- [29] Kholodar, D. B., Thomas, J. P., Dowell, E. H. and Hall, K. C. "A Parameter Study of Transonic Airfoil Flutter and Limit Cycle Oscillation Behavior," In *43rd Structures, Structural Dynamics, and Materials Conference and Exhibit*, Denver, CO, April 2002, AIAA-02-1211.
- [30] Hall, K. C., Thomas, J. P., and Dowell, E. H., "Proper Orthogonal Decomposition Technique for Transonic Unsteady Aerodynamic Flows", *AIAA Journal*, Vol. 38, No. 10, 2000, pp. 1853-1862.
- [31] Ni, R., "A Multiple Grid Scheme for Solving the Euler Equations", *AIAA Journal*, Vol. 20., pp. 1565-1571, November, 1982.
- [32] Saxor, A. P., "A Numerical Analysis of 3-D Inviscid Stator/Rotor Interactions Using Non-Reflecting Boundary Conditions", Gas Turbine Laboratory Report 209, MIT March 1992.
- [33] Kholodar, D. B. "Aeroelastic Response of an Airfoil with Structural and Aerodynamic Nonlinearities," Doctoral Dissertation, Dept. of Mechanical Engeneering and Material Science, Duke Univ., Durham, NC, 2002.
- [34] Dowell, E. H. (ed.), Crawley, E. F., Curtiss Jr., H. C., Scanlan, R. H., and Sisto, F., "A Modern Course in Aeroelasticity," Kluwer Academic Publishers, 1995.
- [35] Seidel, D. A., Bennett, R. M., Whitlow, W., Jr., "An Exploratory Study of Finite Difference Grids for Transonic Unsteady Aerodynamics," NASA-TM-84583, 1982.
- [36] Landahl, M., "Unsteady Transonic Flow," Oxford: Pergamon, 1961.
- [37] Davis, S. N. and Malcom, G. N., "Transonic Shock-Wave/Boundary-Layer Interactions on an Oscillating Airfoil," *AIAA Journal*, Vol. 18, No. 11, Nov. 1980, pp. 1306-1312.

- [38] Magnus, R. J., "Computational Research on Inviscid, Unsteady, Transonic Flow Over Airfoils," ONR CASCD/LVP 77-010, 1977.
- [39] Bendiksen, O. O. and Kousen, K. A., "Transonic Flutter Analysis Using the Euler Equations," AIAA Paper 87-0911-CP, Apr. 1987.
- [40] Ueda, T. and Dowell, E. H., "Flutter Analysis Using Nonlinear Aerodynamic Forces" *Journal of Aircraft*, Vol. 21, No. 2, Feb. 1984, pp. 101-109.
- [41] Isogai, K., "Numerical Study of Transonic Flutter of a Two-Dimensional Airfoil," NAL TR-617T, National Aerospace Institute, Tokyo, Japan, 1980.
- [42] Thomas, J. P., Dowell, E. H. and Hall, K. C. "Transonic Limit Cycle Oscillation Analysis Using Reduced Order Aerodynamic Models," In *42nd Structures, Structural Dynamics, and Materials Conference and Exhibit*, Seattle, WA, April 2001. AIAA-01-1212.
- [43] Florea, R., Hall, K. C., and Dowell, E. H. "Eigenmode Analysis and Reduced-Order Modeling of Unsteady Transonic Potential Flow Around Airfoils," *Journal of Aircraft*, Vol. 37, No. 3, 2000, pp. 454-462.
- [44] Hall, K. C., Thomas, J. P., and Clark, W. S., "Computation of Unsteady Nonlinear Flows in Cascades Using a Harmonic Balance Technique," *AIAA Journal*, Vol. 40, No. 5, May 2002, pp. 879-886.
- [45] Thomas, J. P., Dowell, E. H., and Hall, K. C., "Nonlinear Inviscid Aerodynamic Effects on Transonic Divergence, Flutter and Limit Cycle Oscillations," *AIAA Journal*, Vol. 40, No. 4, April 2002, pp. 638-646.
- [46] Schewe, G., and Deyhle, H., "Experiments on Transonic Flutter of a Two-Dimensional Supercritical Wing with Emphasis on Non-Linear Effects," Proceeding of the Royal Aeronautical Society Conference on Unsteady Aerodynamics, London, UK, July 17-18, 1996.
- [47] Schewe, G., Knipfer, A., Mai, H., and Dietz, G., "Experimental and Numerical Investigation of Nonlinear Effects in Transonic Flutter," English Version (Translated by Dr. W. F. King III), German Aerospace Center DLR Final Report Number DLR IB 232-2002 J 01, Corresponds to Final Report for BMBF: Nichtlineare Effekte beim transsonischen Flattern (FKZ 13 N 7172), and Internal Report DLR IB 2001 J03, January 25, 2002.
- [48] Knipfer, A., and Schewe, G., "Investigations of an Oscillating Supercritical 2D Wing Section in Transonic Flow," AIAA Paper 99-0653, 36th Aerospace Sciences Meeting and Exhibit, Reno, NV, January 1999.
- [49] McMullen, M., Jameson, A., and Alonso, J. J., "Acceleration of Convergence to Period Steady State in Turbomachinery Flows," AIAA Paper 2001-0152, 39th AIAA Aerospace Sciences Meeting and Exhibit, January, 2001, Reno, NV.

- [50] McMullen, M., Jameson, A., and Alonso, J. J., "Application of a Non-Linear Frequency Domain Solver to the Euler and Navier-Stokes Equations," AIAA Paper 2002-0120, 40th AIAA Aerospace Sciences Meeting and Exhibit, January, 2002, Reno, NV.
- [51] Ni, R., "A Multiple Grid Scheme for Solving the Euler Equations," *AIAA Journal*, Vol. 20., pp. 1565–1571, November, 1982.
- [52] Saxor, A. P., "A Numerical Analysis of 3-D Inviscid Stator/Rotor Interactions Using Non-Reflecting Boundary Conditions," Gas Turbine Laboratory Report 209, MIT March 1992.
- [53] Spalart, P. R. and Allmaras, S. R., "A One Equation Turbulence Model for Aerodynamic Flows," AIAA Paper 92-0439, January, 1992.
- [54] Weber, S., Jones, K. D., Ekaterinaris, J. A., and Platzer, M. F., "Transonic Flutter Computations for a 2D Supercritical Wing," AIAA Paper 99-0798, 36th Aerospace Sciences Meeting and Exhibit, Reno, NV, January 1999.
- [55] Tang, L., Bartels, R. E., Chen, P. C., and Liu, D. D., "Numerical Investigation of Transonic Limit Cycle Oscillations of a Two-Dimensional Supercritical Wing," *Journal of Fluids and Structures*, Vol. 17., No. 1, pp. 29–41, January, 2003.
- [56] Castro, B. M., Jones, K. D., Ekaterinaris, J. A., and Platzer, M. F., "Analysis of the Effect of Porous Wall Interference on Transonic Airfoil Flutter," AIAA 2001-2725, June, 2001.
- [57] Castro, B. M., Ekaterinaris, J. A., and Platzer, M. F., "Navier-Stokes Analysis of Wind-Tunnel Interference on Transonic Airfoil Flutter," *AIAA Journal*, Vol. 40, No. 7, July 2002, pp. 1269–1276.
- [58] Baldwin, B. and Lomax, H., "Thin layer approximation and algebraic model for separated turbulent flow," AIAA-78-257, 1978.
- [59] Bartels, R. E., "Mesh strategies for accurate computation of unsteady spoiler and aeroelastic problems," *Journal of Aircraft*, Vol. No 37, pp.521-525, 2000.
- [60] Castro, B. M., Ekaterinaris, J. A. and Platzer, M. F., "Transonic Flutter Computations for the NLR 7301 Airfoil Inside a Wind Tunnel," AIAA-2000-0984, 2000.
- [61] Chen, P. C., Sarhaddi, D. and Liu, D.D., "Limit Cycle Oscillation Studies of a Fighter with External Stores," AIAA-98-1727, 1998.
- [62] Cunningham, H. J., Batina, J. T. and Bennett, R. M., "Modern Wing Flutter Analysis by Computational Fluid Dynamics Methods," *Journal of Aircraft*, Vol. No. 25, pp.962-968, 1988.
- [63] Cunningham Jr., A. M. and Meijer, J. J., "Semi-Empirical Unsteady Aerodynamics for Modeling Aircraft Limit Cycle Oscillations and Other Nonlinear Aeroelastic Problems," *International Forum on Aeroelasticity and Structural Dynamics (Manchester)*, 1995.

- [64] Denegri, C. M., "Limit Cycle Oscillation Flight Test Results of a Fighter with External Stores," AIAA-2000-1394, 2000.
- [65] Edwards, J. W., "Transonic Shock Oscillations and Wing Flutter Calculated with an Interactive Boundary Layer Coupling Method," *Euromech-Colloquium 349 Simulation of Fluid-Structure Interaction in Aeronautics (Göttingen)*, 1996.
- [66] Edwards, J. W., Bennett, R. M., Whitlow, Jr. and Seidel, D. A., "Time-Marching Transonic Flutter Solutions Including Angle-of-Attack Effects," *Journal of Aircraft*, Vol. No. 20, pp.899-906, 1983.
- [67] Hall, K. E., Thomas, J. P. and Dowell, E. H., "Reduced-Order Modeling of Unsteady Small Disturbance Flows using a Frequency-Domain Proper Orthogonal Decomposition Technique," AIAA-99-0655, 1999.
- [68] Hartwich, P. M. and Agrawal, S., "Method for Perturbing Multiblock Patched Grids in Aeroelastic and Design Optimization Applications," AIAA-97-2038, 1997.
- [69] <http://fmad-www.larc.nasa.gov/biedron/Cfl3dv6/cfl3dv6.html>
- [70] Knipfer, A. and Schewe, G., "Investigations of an Oscillation Supercritical 2-D Wing Section in a Transonic Flow," AIAA-99-0653, 1999.
- [71] Knipfer, A., Schewe, G. and Wendt, V., "Numerische und experimentelle Untersuchungen an einem schwingenden NLR 7301-Profil in transsonischer Stroemung, Teil 1: Flattern und erzwungene Schwingungen," *DLR Bericht IB 232-98 J 05*, 1998.
- [72] Krist, S. L., Biedron, R. T. and Rumsey, C. L., "CFL3D User's Manual Version 5.0," *NASA Langley Research Center*, Hampton, VA, 1997.
- [73] Norton, W. J., "Limit Cycle Oscillation and Flight Flutter Testing," *Proceedings of the Society of Flight Test Engineers 21st Annual Symposium*, 1990.
- [74] Roe, P. L., "Approximate Riemann Solvers, Parameter Vectors, and Difference Schemes," *Journal of Computational Physics*, Vol. No. 43, pp.357-372, 1981.
- [75] Schewe, G. and Deyhle, H., "Experiments on Transonic Flutter of a Two-Dimensional Supercritical Wing with Emphasis on the Nonlinear Effects," *Proceedings of the Royal Aeronautical Society Conference on Unsteady Aerodynamics (London)*, 1996.
- [76] Spalart, P. and Allmaras, S., "A One-Equation Turbulence Model for Aerodynamic Flows," AIAA-92-0439, 1992.
- [77] Weber, S., Jones, K. D., Ekaterinaris, J. A. and Platzer, M. F., "Transonic Flutter Computations for a 2-D Supercritical Wing," AIAA-99-0798, 1999.
- [78] Hall, K. C., Thomas, J. P., Clark, W. S., "Computation of Unsteady Nonlinear Flows in Cascades Using a Harmonic Balance Technique", *AIAA Journal*, Vol. 40, No. 5, 2002, pp. 879–886.

[79] Thomas, J. P., Dowell, E. H., Hall, K. C., "Nonlinear Inviscid Aerodynamic Effects on Transonic Divergence, Flutter and Limit Cycle Oscillations", *AIAA Journal*, Vol. 40, No. 4, 2002, pp. 638–646.

[80] Thomas, J. P., Dowell, E. H., Hall, K. C., "Modeling Viscous Transonic Limit Cycle Oscillation Behavior Using a Harmonic Balance Approach", AIAA Paper 2001-1414, 43rd AIAA/ASME/ASCE/AHS/ASC Structures, Structural Dynamics and Materials (SDM) Conference, Denver, CO, April 2002.

[81] Yates, E. C., Jr., "AGARD Standard Aeroelastic Configurations for Dynamic Response I - Wing 445.6", NASA TM 100492, August 1987; also *Proceedings of the 61st Meeting of the Structures and Materials Panel*, Germany, AGARD-R-765, 1985, pp. 1–73.

[82] Yates, E. C., Jr., Land, N. S., and Foughner, J. T. , Jr., "Measured and Calculated Subsonic and Transonic Flutter Characteristics of a 45 Deg Sweptback Wing Planform in Air and in Freon-12 in the Langley Transonic Dynamics Tunnel", NASA TN D-1616, March 1963.

[83] Edwards, J. W., Schuster, D. M., Spain, C. V., Keller, D. F., Moses, R. W., "MAVRIC Flutter Model Transonic Limit Cycle Oscillation Test", AIAA Paper 2001-1209, 42th AIAA/ASME/ASCE/AHS/ASC Structures, Structural Dynamics and Materials (SDM) Conference, Seattle, WA, April 2001.

[84] Thomas, J. P., Dowell, E. H., Hall, K. C., "Three-Dimensional Aeroelasticity Using Proper Orthogonal Decomposition Based Reduced Order Models", AIAA Paper 2001-1526, 42nd AIAA/ASME/ASCE/AHS/ASC Structures, Structural Dynamics and Materials (SDM) Conference, Seattle, WA, April 2001.

[85] Lee-Rausch, E. M. and Batina, J. T., "Wing Flutter Boundary Prediction Using Unsteady Euler Aerodynamic Method", *Journal of Aircraft*, Vol. 32, No. 2, 1995, pp. 416–422.

[86] Gordnier, R. E., Melville, R. B., "Transonic Flutter Simulations Using an Implicit Aeroelastic Solver", *Journal of Aircraft*, Vol. 37, No. 5, 2000, pp. 872–879.

[87] Charles M. Denegri, Jr., "Limit Cycle Oscillation Flight Test Results of a Fighter with External Stores," *Journal of Aircraft*, Vol. 37, No. 5, pp. 761–769, 2000.

[88] Jeffrey P. Thomas and Earl H. Dowell and Kenneth C. Hall, "A Harmonic Balance Approach for Modeling Three-Dimensional Nonlinear Unsteady Aerodynamics and Aeroelasticity", ASME Paper IMECE-2002-32532, November 2002.

[89] Jeffrey P. Thomas and Kenneth C. Hall and Earl H. Dowell, "A Harmonic Balance Approach for Modeling Nonlinear Aeroelastic Behavior of Wings in Transonic Viscous Flow", AIAA Paper 2003-1924, April 2003.

- [90] Kenneth C. Hall and Jeffrey P. Thomas and William S. Clark, "Computation of Unsteady Nonlinear Flows in Cascades Using a Harmonic Balance Technique," *AIAA Journal*, Vol. 40, No. 5, pp. 879–886, May 2002.
- [91] Jeffrey P. Thomas and Earl H. Dowell and Kenneth C. Hall, "Nonlinear Inviscid Aerodynamic Effects on Transonic Divergence, Flutter and Limit Cycle Oscillations," *AIAA Journal*, Vol 40, No. 4, pp 638-646, April 2002.
- [92] Ron-Ho Ni, "A Multiple Grid Scheme for Solving the Euler Equations", *AIAA Journal*, Vol. 20, No. 11, pp. 1565–1571, November 1982.
- [93] Roger L. Davis and Ron Ho Ni and Wallace W. Bowley, "Prediction of Compressible, Laminar Viscous Flows Using a Time-Marching Control Volume and Multiple-Grid Technique," *AIAA Journal*, Vol. 22, No. 1, pp. 1573–1581, November 1984.
- [94] A. P. Saxor, "A Numerical Analysis of 3-D Inviscid Stator/Rotor Interactions Using Non-Reflecting Boundary Conditions", MIT, No. 209, March 1992, Gas Turbine Laboratory Report 209.
- [95] P. R. Spalart and S. R. Allmaras, "A One Equation Turbulence Model for Aerodynamic Flows", AIAA Paper 92-0439, January 1992.

- [90] Kenneth C. Hall and Jeffrey P. Thomas and William S. Clark, "Computation of Unsteady Nonlinear Flows in Cascades Using a Harmonic Balance Technique," *AIAA Journal*, Vol. 40, No. 5, pp. 879–886, May 2002.
- [91] Jeffrey P. Thomas and Earl H. Dowell and Kenneth C. Hall, "Nonlinear Inviscid Aerodynamic Effects on Transonic Divergence, Flutter and Limit Cycle Oscillations," *AIAA Journal*, Vol 40, No. 4, pp 638-646, April 2002.
- [92] Ron-Ho Ni, "A Multiple Grid Scheme for Solving the Euler Equations", *AIAA Journal*, Vol. 20, No. 11, pp. 1565–1571, November 1982.
- [93] Roger L. Davis and Ron Ho Ni and Wallace W. Bowley, "Prediction of Compressible, Laminar Viscous Flows Using a Time-Marching Control Volume and Multiple-Grid Technique," *AIAA Journal*, Vol. 22, No. 1, pp. 1573–1581, November 1984.
- [94] A. P. Saxor, "A Numerical Analysis of 3-D Inviscid Stator/Rotor Interactions Using Non-Reflecting Boundary Conditions", MIT, No. 209, March 1992, Gas Turbine Laboratory Report 209.
- [95] P. R. Spalart and S. R. Allmaras, "A One Equation Turbulence Model for Aerodynamic Flows", AIAA Paper 92-0439, January 1992.
- [96] Sandford, Maynard C., Seidel, David A., Eckstrom, Clinton V., and Spain, Charles V., "Geometrical and Structural Properties of an Aeroelastic Research Wing," NASA-TM-4110, April 1989.